

CONFIDENTIAL UP TO AND INCLUDING 27/08/2023 - DO NOT COPY, DISTRIBUTE OR MAKE PUBLIC IN ANY WAY

Diffuse reflectance spectroscopy characterization of molecular absorption via graphene based photodetectors

Michael Evans

Supervisors: Prof. Nicholas Le Thomas , Prof. Frank Koppens (ICFO)

Counsellors: Dr. Stijn Goossens (ICFO), Ir. Gabriel Mercier (ICFO), Ir. Carles Monasterio (ICFO)

Master's dissertation submitted in order to obtain the academic degree of
European Master of Science in Photonics

ICFO - Institut de Ciències Fotòniques, Castelldefels

and

Ghent University

Department of Information Technology

Chair: Prof. dr. ir. Bart Dhoedt

Faculty of Engineering and Architecture

Academic year 2017-2018



Statement of Confidentiality

Confidential up to and including 27/08/2023
Important

This master dissertation contains confidential information and/or confidential research results proprietary to ICFO. It is strictly forbidden to publish, cite or make public in any way this master's dissertation or any part thereof without the express written permission of ICFO.

Under no circumstances may this masters dissertation be communicated to or put at the disposal of third parties. Photocopying or duplicating it in any other way is strictly prohibited.

Disregarding the confidential nature of this master dissertation may cause irremediable damage to ICFO.

The stipulations mentioned above are in force until the embargo date.

Michael Evans, August 2018

CONFIDENTIAL UP TO AND INCLUDING 27/08/2023 - DO NOT COPY, DISTRIBUTE OR MAKE PUBLIC IN ANY WAY

Diffuse reflectance spectroscopy characterization of molecular absorption via graphene based photodetectors

Michael Evans

Supervisors: Prof. Nicholas Le Thomas , Prof. Frank Koppens (ICFO)

Counsellors: Dr. Stijn Goossens (ICFO), Ir. Gabriel Mercier (ICFO), Ir. Carles Monasterio (ICFO)

Master's dissertation submitted in order to obtain the academic degree of
European Master of Science in Photonics

ICFO - Institut de Ciències Fotòniques, Castelldefels

and

Ghent University

Department of Information Technology

Chair: Prof. dr. ir. Bart Dhoedt

Faculty of Engineering and Architecture

Academic year 2017-2018



Acknowledgements

First and foremost I would like to thank my promotors Prof. Frank Koppens, Prof. Nicholas Le Thomas and my supervisors Dr. Stijn Goosens, Gabriel Mercier and Carles Monasterio for giving me the opportunity to contribute and work in QMantis. I would like to thank Gabriel and Carles especially for countless hours of assistance and advice in the lab. I also want to thank everyone else in the Quantum Nano-Optoelectronics group for providing a fantastic atmosphere and answering all my questions. The experience and knowledge gained has been invaluable.

I would also like to thank my family, friends and fellow classmates for their support throughout the year.

Michael Evans, August 2018

Permission of Use on Loan

The author gives permission to make this master dissertation available for consultation and to copy parts of this master dissertation for personal use, after embargo date. In all cases of other use, the copyright terms have to be respected, in particular with regard to the obligation to state explicitly the source when quoting results from this master dissertation.

Michael Evans, August 2018

Diffuse reflectance spectroscopy characterization of molecular absorption via graphene based photodetectors

by

Michael Evans

Master's dissertation submitted in order to obtain the academic
degree of Master of Science in Photonics Engineering

Academic year 2017-2018

Promotors: Prof. Dr. F. KOPPENS &

Prof. Dr. N. LE THOMAS

Counsellor: Dr. Ir. S. GOOSENS &

Ir. G. MERCIER &

Ir. C. MONASTERIO

Faculty of Engineering and Architecture

Ghent University

Department of Electronics and Information Systems

Chair: Prof. Dr. Ir. B. Dhoedt

Abstract

This Master dissertation explores diffuse reflection spectroscopy as a viable tool for analytical chemistry, both quantitatively and qualitatively. *In-vitro* optical phantoms are created to mimic the turbid diffuse environments of human tissue. The method is first explored in the visible spectrum with ink as an absorbing chromophore. To test the efficiency of the method, glucose was chosen due to its basic chemical composition, non-toxicity and its medical relevance. Glucose absorption peaks ($1.59\mu m$ and $2.1\mu m$) altered the focus of the thesis from exploring diffuse reflection spectroscopy in the visible range to measuring in the short-wavelength infrared range ($1000 - 2200nm$).

Contents

Statement of Confidentiality	i
Acknowledgements	iii
Permission of Use on Loan	iv
Abstract	v
Extended Abstract	vi
Table of Contents	viii
List of Figures	xii
List of Tables	xiii
1 Introduction	1
1.1 Motivation For Coupling Analytical Chemistry and Optics	1
1.2 Glucose	2
1.2.1 Continuous Glucose monitoring	2
1.2.2 Wearable Glucose sensor	2
1.2.3 Thesis objective and challenges	3
1.3 Thesis outline	4
2 Spectroscopic Detection of Glucose	5
2.1 Molecular Absorption Spectroscopy	5
2.1.1 Fourier Transform Spectrometer	7

2.1.2	Beer-Lambert Law	10
2.2	Absorption Spectroscopy of Glucose solutions	11
2.2.1	Glucose Spectrum	11
2.2.2	Water Spectrum	13
2.2.3	Theoretical Signal-to-Noise Ratio	14
2.3	In-Vitro Tissue Like Optical Phantoms	16
2.4	Diffuse Reflectance Spectroscopy	18
2.4.1	Optical Propagation Path	19
2.4.2	Distance Decay	24
2.5	Simulations of target glucose peaks	24
2.5.1	Lipofundin scattering	24
2.5.2	Lipofundin anisotropic g factor	26
2.5.3	Lipofundin reduced scattering coefficient	28
2.5.4	Fiber separation approximation	28
2.5.5	Human tissue anisotropic g factor	30
2.6	Glucose Sensor Based on a Broadband Flexible Detector	32
2.6.1	Integrating an electrically active colloidal quantum dot photodiode with a graphene phototransistor	32
2.6.2	Sensor Configuration	32
2.7	Conclusion	34
3	Mapping the exponential decay in the visible spectrum	36
3.1	Introduction	36
3.2	Experimental set-up design	36
3.2.1	The fibers	40
3.3	Map the intensity tomography of the solution	42
3.3.1	3-D plot: Exponential radial distance decay results	44
3.3.2	2-D plot: Top down view	45
3.3.3	3-D plot: Log scale of intensity	46
3.4	Exploring axial symmetry	47
3.4.1	Reproducibility of results	49

3.5	Extract μ_a concentration from intensity and radial distance	52
4	Integrating a broadband NIR source and complimentary NIR detector	55
4.1	Introduction	55
4.2	Experimental set-up design	55
4.3	Characterization of set-up components	62
4.4	Measurement results	72
4.5	Conclusion	74
5	Introducing Glucose as a Chromophore	76
5.1	Introduction	76
5.2	Calculating glucose concentrations	76
5.3	Measurement results	77
5.3.1	Troubleshooting the fluctuations	81
5.3.2	Improved results	85
5.4	Conclusion	87
6	Conclusion & Future Work	88
	Bibliography	92

List of Figures

2.1	Vibrational energy level distribution	6
2.2	The electromagnetic spectrum	7
2.3	Schematic of a Michelson fourier transform spectrometer.	8
2.4	Schematic of TWINS [10].	9
2.5	Glucose Spectrum found from onsite spectrometer, Cary 5000 UV-Vis-NIR. . . .	12
2.6	Deionized water transmission spectrum obtained from on-site commercial Carry UV-Vis-NIR spectrometer.	13
2.7	Molar absorptivity $\epsilon(\lambda)$ for interfering biomolecules in (a) the first octave band and (b) the combination band plotted with data from <i>Amerov et al.</i> [11]	14
2.8	Schematic of interlipid scattering particles in Lipofundin MCT/LCT 20% as described in <i>Van Staveren et al.</i> [20].	17
2.9	Particle size distribution of Lipofundin MCT. Graph based on data from [24] . .	18
2.10	Reflection vs transmission [16].	19
2.11	Light scattering regimes with respect to wavelength and particle size [16]. . . .	20
2.12	Schematic of scattering regimes (a) Forward ($g > 0$), (b) Isotropic ($g \approx 0$) & (c) Back scattering ($g < 0$).	21
2.13	Henyeey-Greenstein phase function simulation for contrasting anisotropic g factors.	23
2.14	Polar plot simulations for (a) isotropic scattering of $g = 0$ & (b) forward scattering of $g = 0.98$	23
2.15	OMLC, <i>Flock et al.</i> & <i>Van Staveren et al.</i> characterization of Lipofundin MCT/LCT 10% (a) Scattering coefficient μ_s & (b) the anisotropic factor g . [21] . . .	25
2.16	(a) Simulation via MATLAB of the phase function for different anisotropic $g(\lambda)$ factors for Lipofundin & (b) Schematic of corresponding physical representation .	27
2.17	(a) Polar simulations via MATLAB of the anisotropic g factors scattering for Lipofundin & (b) Mie approximations for $g(1.5\mu m) = 0.18$ and $g(2.1\mu m)$	28
2.18	Schematic of fiber separation approximation model	29

2.19	(a) Wavelength dependent anisotropic g values for human tissue for contrast-ing studies [8] & (b) the wavelength dependent reduced scattering coefficient for human tissue [9].	31
2.20	(a) Schematic of Pbs-QD & graphene hybrid photodetector [3] (b) Spectral de-pendence of the photoresponse of CQDs with an excitation peak of $920nm$ & (c) Spectral dependence of the photoresponse of CQDs with an excitation peak of $1,670nm$ [4]	33
3.1	Spectrum of Thorlabs visible laser diode.	38
3.2	Transmission spectrum of black china ink for contrasting concentrations in bulk water solution.	39
3.3	Response curve of the PDA36A Si photodetector [36].	40
3.4	(a) Attachment of a stripped and cleaved fiber through a needle & (b) microscope image of the exposed fiber end.	41
3.5	(a) Fiber microscope image of the minimum separation distance between two stripped fibers & (b) The final set-up of source and collection fiber in an optical phantom.	41
3.6	Schematic of the experimental set-up.	42
3.7	Schematic of x & y sweep of the phantoms tomography.	43
3.8	3-D intensity tomography profile of the exponential distance decay in the Lipo-fundin solution for (a) $0ml$ of ink (b) $1ml$ of ink (c) $2ml$ of ink (d) $2.5ml$ of ink & (e) $3ml$ of ink.	44
3.9	2-D top down view of the tomography profile of the exponential distance decay in the Lipofundin solution for (a) $0ml$ of ink (b) $1ml$ of ink (c) $2ml$ of ink (d) $2.5ml$ of ink & (e) $3ml$ of ink.	45
3.10	3-D view of the logarithm of the intensity profile of the exponential distance decay in the Lipofundin solution for (a) $0ml$ of ink (b) $1ml$ of ink (c) $2ml$ of ink (d) $2.5ml$ of ink & (e) $3ml$ of ink.	46
3.11	Tomography direction of x -sweeps & y -sweep.	47
3.12	2-D cross section in the x & y direction of the distance decay data for (a) $0ml$ of ink (b) $1ml$ of ink (c) $2ml$ of ink (d) $2.5ml$ of ink & (e) $3ml$ of ink.	48
3.13	Tomography map of data points taken at $5mm$ of every x -sweep.	49
3.14	Reproducibility of results for same data recorded in both x & y -sweeps for (a) $0ml$ of ink (b) $1ml$ of ink (c) $2ml$ of ink (d) $2.5ml$ of ink & (e) $3ml$ of ink.	50
3.15	Schematic of possible discrepancy issue between x and y sweeps.	51
3.16	Intensity vs for ink concentrations for six set distances.	53
3.17	Distance decay model $\log(I * \rho^2)$ vs ρ	54

4.1	NKT EXR-20 output power spectrum [26]	56
4.2	Schematic of a PCF fiber used in NKT products. Light is guided by a high index embedded solid core surround by a low index cladding housing a hexagon lattice of air holes. A polymer outer coat offers protection. [31]	57
4.3	NKT SuperK EXR-20 collimator fiber end and corresponding SuperK CONNECT alignment case [31].	58
4.4	Transmission profiles of the each filter, data plotted from Thorlabs specification sheets [33], [34].	59
4.5	Filter and collimation component of experimental set-up.	60
4.6	Responsivity curve for the New England ext. InGaAs photodiode [35].	61
4.7	Image of full experimental set-up with new components added.	62
4.8	Schematic of set-up design to test the SuperK EXR-20. output.	63
4.9	Transmission spectrum of the neutral density filters, data plotted from Thorlabs specification sheets [37]	63
4.10	NKT SuperK EXR-20 spectrum bandwidth for power increments.	64
4.11	Schematic of the mode-field diameter measurement with a fiber core for different modes.	65
4.12	Schematic of the mode-field diameter measurement with a fiber core for different modes	65
4.13	Transmission profile of ECO-550 glass [28].	66
4.14	The source fiber (a) normal commercial end & (b) the stripped and cleaved end.	68
4.15	The collection fiber (a) normal commercial end & (b) the stripped and cleaved end.	68
4.16	Shematic of power conversion efficiency locations measured in the set-up.	69
4.17	Power loss conversion efficiencies.	71
4.18	Spectrums recorded from the phantom under illumination of the full bandwidth of the SuperK source for (a) no ink, (b) 0.2ml of ink and (c) 0.4ml of ink	72
4.19	Distance decay of first overtone band with 1.4 μ m longpass filter	73
4.20	Intensity of the 1.59 μ m peak in log scale with separation distance increments.	74
5.1	Beer-Lambert function simulated of the molar absorptivities of the two glucose peaks via MATLAB.	77
5.2	First overtone band recorded for concentrations of (a) no glucose (b) 5% glucose (c) 15% glucose & (d) 25% glucose in the phantom	78
5.3	Glucose concentration decay for the 1.59 μ m peak at 0.05mm separation.	79

5.4	Four interferogram measurements repeated by TWINS for 25% glucose concentration at $0.05mm$ distance.	80
5.5	An example of an accurate interferogram measurement with acceptable noise. . .	81
5.6	Time trace of intensity fluctuations with the step motor timing-belt detached. . .	82
5.7	Time trace for 15 minute periods of the phantom with contrasting input powers of (a) 25%, (b) 50%, (c) 75% & (d) 100%.	83
5.8	Time trace for a 15 minute period of water at 100% input power.	84
5.9	Improved results with no fluctuations present.	85
5.10	Time trace for a 15 minute period at 100% input power with improved attachment. .	85
5.11	Improved results with no fluctuations present.	86
5.12	Exponential distance decay for the $1.59\mu m$ peak in the phantom.	86
6.1	Broadband spectrum measurement for QMantis hybrid graphene- <i>CQD</i> detector. .	91

List of Tables

2.1	Composition of 1000ml of both Lipofundin MCT/LCT 10% 20% emulsions in bulk water [14].	16
2.2	μ_s & l_{MFP} values for 685nm, 1590nm & 2100nm for both approximations	26
2.3	Anisotropic g values & angle θ for 90% scattering of the light after the event for 685nm, 1590nm & 2100nm for both approximations	26
2.4	μ'_s & l_{TMFP} values for 685nm, 1590nm & 2100nm for both approximations . . .	28
2.5	Fiber separation distance approximations for both models for 685nm, 1590nm & 2100nm	30
3.1	Gradient values of intensity vs ink concentration.	52
4.1	SuperK EXR-20 optical specifications from NKT datasheet. [26]	57
4.2	Collimator wavelength dependent diameter vs source wavelength dependent . . .	66
4.3	The SuperK power just after the 1.5 μ m longpass filter	69
4.4	The SuperK power just after the collimator for both the 1.5 μ m and 2.25 μ m filters	70
4.5	The SuperK power measure in the lock-in amplifier after passing through the TWINS.	70

Chapter 1

Introduction

1.1 Motivation For Coupling Analytical Chemistry and Optics

Analytical chemistry is the field dedicated to separating, identifying and quantifying matter. It can be separated into two analysis categories, quantitative and qualitative. Qualitative analysis is the measurement of identifying chemical species. Quantitative analysis delves further by determining numerical counts or concentrations. Methods and techniques in analytical chemistry have evolved vastly with the technology revolution of the 20th century. Classically, *wet chemical* methods were used to analyze the chemical composition of a sample. Qualitatively, techniques such as precipitation, extraction and distillation were employed and identification via color, odor, melting points, radioactivity, reactivity, etc. Quantitative measurements of concentrations were realized from mass or volume changes.

With the advancement of modern instrumentation came new innovative techniques such as mass spectrometry, electrochemical analysis, thermal analysis and microscopy to name a few. Exploiting optics and the electromagnetic spectrum as a tool to investigate matter was the fundamental step towards the field of spectroscopy. Illuminating matter with different portions of the electromagnetic spectrum can cause many different atomic or molecular events that can be detected.

One common optical spectroscopic technique is absorption spectroscopy. It is a damage free analysis technique. Under electromagnetic illumination the sample can absorb fixed portions of energy from the source. Each chemical species has a unique absorption spectrum and analyzing which frequencies are absorbed by comparing the illumination transmission spectrums before and after the sample can qualitatively identify which absorbing chemical species (chromophores) are present. Quantitative concentration information can also be retrieved with high resolution instrumentation by measuring the transmission loss at a single wavelength affected by the chemical species absorption.

1.2 Glucose

Glucose is a good chemical species to explore in this research project. Reasons being it is non toxic and easy to work with. It also has a simple chemical structure made up of carbon, hydrogen and oxygen atoms ($C_6H_{12}O_6$). These three atoms are the basis for most organic compounds. In parallel, it also has medical significance. Relatively high concentrations of glucose in the blood is an indication of pre-diabetes. If left untreated, it can develop into full blown diabetes.

1.2.1 Continuous Glucose monitoring

Over 350 *million* people are affected by diabetes worldwide. Symptoms can include feeling very thirsty, urinating more frequently than usual, fatigue and blurred vision. Healthy people will also display spikes of high glucose concentrations in the blood after food is digested. However a hormone known as insulin, which is produced in the pancreas, transfers the excess glucose to the cells where it is broken down to produce energy. Diabetic patients are unable to break down the excess glucose into energy in the blood. The reason being, the pancreas has failed to produce enough insulin (type 1) or the insulin that is produced does not work properly (type 2). The effect, if untreated, can lead to many serious health conditions such as blood vessel damage, cardiovascular disease, strokes, and eye conditions like glaucoma for example [1].

At present, there is no cure for a diabetic diagnosis. Patients can only contain the effects of the disease by self managing glucose levels via an external intake of insulin. For type 2 diabetic patients, this involves oral digestion of insulin. For type 1 diagnosed patients, insulin injections are necessary. Therefore, continuous glucose monitoring is essential for a diabetic patient to maintain a healthy lifestyle and reduce the overall cost of treatment [1].

The continuous glucose monitoring device market is huge and competitive as the diagnosed global population is so large. However the present state of the art of devices are invasive. They include a needle sensor that is embedded to detect glucose levels in the blood or interstitial fluid inbetween cells as it also contains glucose. The invasive device stores the continuous data and sends an alarm to the patient when glucose levels are abnormal. These devices have a continuous lifespan of up to a week and are not available to everybody. The standard invasive test involves placing a small droplet of blood on a test-strip which includes an electronic meter that provides feedback [2].

1.2.2 Wearable Glucose sensor

Absorption spectroscopy potentially could offer an alternative device that overcomes the limitations of the current industry of continuous glucose monitoring devices. Most importantly it has the potential to introduce low cost, longer lifetime, *non-invasive* devices to the market.

The health wearable industry is growing very fast. Not just patients but consumers are display-

ing trends of becoming more health conscience. Society today, compared to the past, is more knowledgeable on the importance of preemptive methods to avoid developing serious health conditions. Current health wearables on the market offer continuous monitoring of sleep patterns, nutrition, fitness and activity, heart rate, UV light exposure to name a few. All with *non-invasive* sensors and transducers. These devices, in parallel, offer smartphone connectivity. Therefore, as well as health conscience consumers, these devices could open a door to home healthcare for certain diseases. A patients doctor could aid in a patients management and offer diagnosis remotely. Thus, reducing unnecessary clinical fees.

Adopting existing optical technology has allowed manufactures to move beyond the realm of prevention and into constant monitoring. The main health wearable companies have already adopted spectroscopy as a method to extract analytical chemistry information from a user. Fitbit and Garmin have included light sources and sensors that can measure pulse oximetry. This is the measure of oxygen in the blood and is key indicator of general health and well being. The concentration ratio of two bio-markers, oxy-hemoglobin and deoxy-hemoglobin measures the overall oxygenation in the body.

1.2.3 Thesis objective and challenges

Absorption spectroscopy via direct transmission of a sample is well understood. Most analytical chemical labs will have such measuring instruments known as spectrometers. Commercial spectrometers are extremely accurate and calibrated. However they require small *in-vitro* sample stages such as cuvettes. In parallel, they are not compatible to samples that exhibit scattering. Integrating spheres could be used for scattering samples, but this still does not address the limitation of *in-vitro* samples.

Therefore adopting a technique that could potentially provide accurate spectroscopic information both quantitatively and qualitatively from a turbid scattering medium would be advantageous for research and industry.

Diffuse reflection spectroscopy is a technique of allowing the concentration of target chemical species in a turbid diffuse environment. Human tissue can be described as a diffuse environment. Light traveling through it propagates in a diffuse manner.

Therefore the goal of this thesis is to build a set-up that can investigate analytical chemistry via diffuse reflection spectroscopy. Glucose will be the target chromophore of detection due to its non toxic and simple common organic compound arrangement. Also, in-lieu of the medical interest of glucose, detection of glucose will be tested in optical *in-vitro* phantoms that attempt to mimic the diffuse environment of human tissue. By proving the concept it could potentially pave the way for further research into *in-vivo* detection.

1.3 Thesis outline

The master thesis is outlined as follows: chapter two introduces the theory of molecular absorption spectroscopy and more specifically of glucose and water. It tackles the theoretical challenges predicted from simulations with detecting glucose in the *NIR* and *SWIR* spectrum. The thesis was designed in a three step process. Each section a pre-cursor to advance to the next. Chapter three involved mapping the exponential decay in the visible spectrum of scattering biological phantoms with absorbing ink concentrations. Chapter four introduces further developments of the experimental set-up and a broadband *NIR* source is integrated. Chapter five, introduces for the first time glucose based phantoms to investigate. A fourth step involves testing the detection with a broadband graphene based flexible detector. Future work is discussed in chapter six and finally the thesis project is concluded in chapter seven.

Chapter 2

Spectroscopic Detection of Glucose

2.1 Molecular Absorption Spectroscopy

Three processes can be used to explain the interaction present when a photon and a molecule come in contact: Scattering, absorption and transmission. The quantum mechanical model of molecules describes discrete molecular energy levels. Each molecule has a unique set of discrete energy levels associated with electronic, vibrational and rotational modes. It can change between two modes if it absorbs incident radiation energy that matches the energy gap between the two quantum mechanical levels. Since the energy absorbed is frequency dependent, $E = h\nu$, the absorption transitions of a molecule is wavelength dependent. This behaviour is intrinsic and unique to each molecule. Due to this quantum behaviour *molecular fingerprinting* becomes possible.

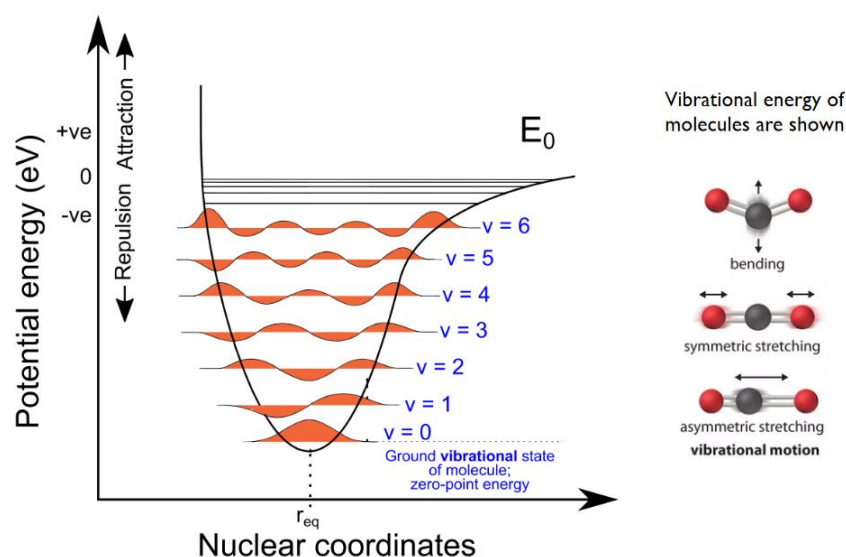


Figure 2.1: Vibrational energy level distribution

For performing molecular absorption spectroscopy three main regions on the electromagnetic spectrum are of interest (fig. 2.2). Electronic absorption transitions occur in the ultraviolet to visible range ($300 - 700nm$), vibrational molecular transitions occur in the infrared ($3 - 30\mu m$) and finally rotational transitions appear in the far-infrared to the microwave region ($100\mu m - 10mm$). Fundamental vibrations exist in the mid-infrared (*mid-IR*). They are a result of transitions due to absorption from the ground to the first excited state and are the most likely to occur. The mid-IR region does not carry enough energy to resonate electrons but it can induce vibrational excitation of covalently bonded atoms and groups. These bonds can classically be thought of as spring-like in nature. During a fundamental vibration a bond between atoms can exhibit stretching or bending resonance behaviour. The higher energies induce stretching while the lower energies induce bending.

Overtone transitions are absorption transitions from the ground to higher states after the first excited state. The probability of photons absorbing decreases with each overtone relative to the fundamental. A combination band also exists where two or more fundamental vibrations occur simultaneously such as bending or stretching. They are also weaker than the absorption of the fundamental band in the mid-IR. Both the first overtone band and the combination band exist in the short wave infrared window (*SWIR*).

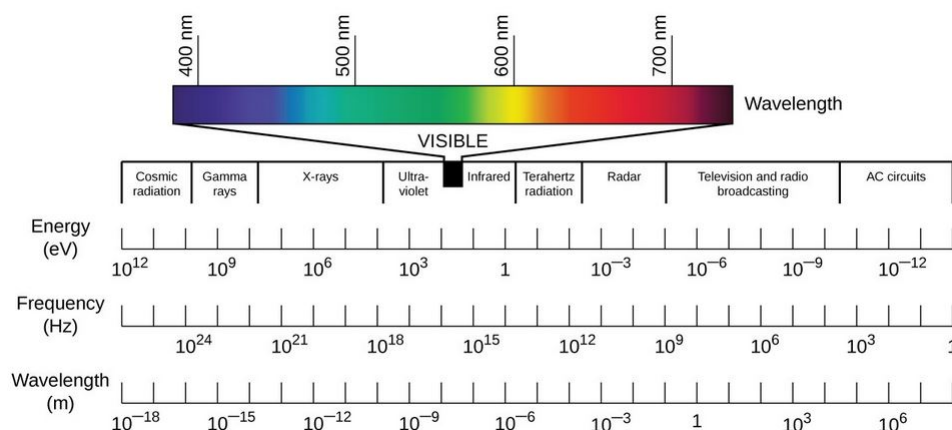


Figure 2.2: The electromagnetic spectrum

2.1.1 Fourier Transform Spectrometer

By sweeping the input wavelength and measuring the absorption of the sample, a spectral profile of molecules in the sample can be deduced. The traditional and most common technique is illuminating the sample with a continuous source. Energy is absorbed according to the characteristics of the molecules in the sample. A monochromator disperses the transmission light into spectral wavelengths. Analyzing changes in the resulting transmission spectrum can *fingerprint* or identify the presence of absorbing chromophores. From the intensity changes of the transmission spectrum, information on concentration can be deduced. The simplest dispersive technique exploits the chromatic dispersion properties of a prism when illuminated by a broad-band source. Chromatic dispersion is a consequence of the wavelength dependent nature of a materials refractive index. The result is contrasting path lengths and phase velocities for each frequency. Mechanically sweeping a slit along the deconstructed spectrum output of the prism allows selection of a single wavelength to output and illuminate a sample with. The resolution of which is defined by its resolving power to separate two wavelengths $\lambda + \Delta\lambda$:

$$R = \frac{\lambda}{\Delta\lambda} = Nm \quad (2.1)$$

N is the number of diffracting grooves on the grating and m is the number of diffracting orders. The average limiting resolution of a commercial dispersive spectrometers is $0.2 - 3nm$ in the *SWIR* [5].

In contrast, Fourier transform spectroscopy uses interference, rather than monochromators such as gratings or prisms, to probe the spectrum of a substance. It is not a new technique with original designs based on the Michelson interferometer from 1880. The advent of the computer and electronic technology complemented its advancement in the mid 1970's. The transmission output from the sample enters an interferometer. The beam is split and travels contrasting path lengths (due to a moving element) introducing a phase difference of constructive and

destructive interference fringes. The emerging output is an interferogram in the time domain by a photodetector, the fourier transform computation of which is the intensity spectrum in the frequency domain (fig.2.3) [7].

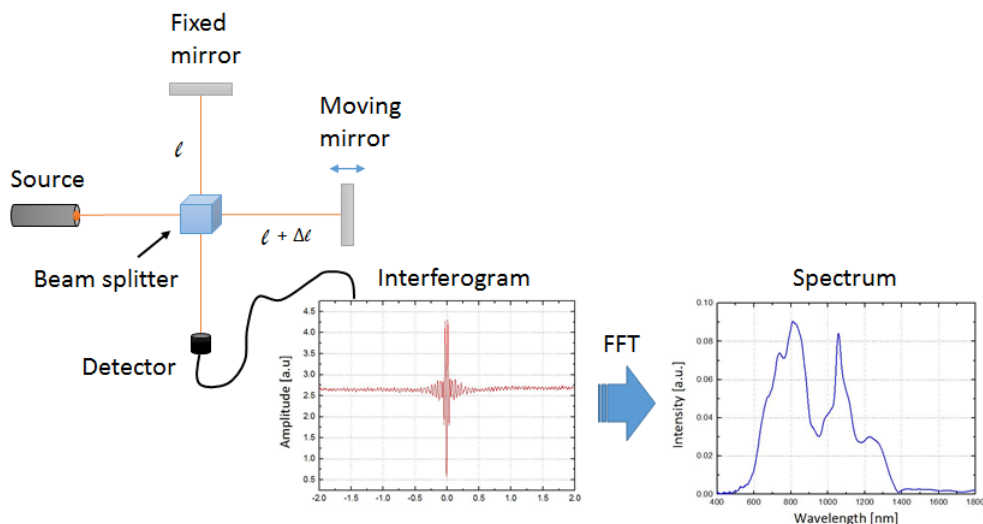


Figure 2.3: Schematic of a Michelson fourier transform spectrometer.

TWINS

The fourier transform spectrometer used during this research employs a contrasting interferometry architect to the Michelson design. TWINS (Translating-Wedge-based Identical pulses eNcoding System) was assembled in Politecnico di Milano by a group of researchers in affiliation with EPFL and University of Zurich, Switzerland [10]. At the heart of the interferometry physics is birefringent non-linear crystals. It demonstrates an extremely broad transparency range from $0.38\mu m - 20\mu m$, making it an ideal tool to investigate the molecular vibrational fingerprint region in the mid *IR* as well as the corresponding combination and overtone bands in the *NIR* and the electronic transitions in the *VIS* [10].

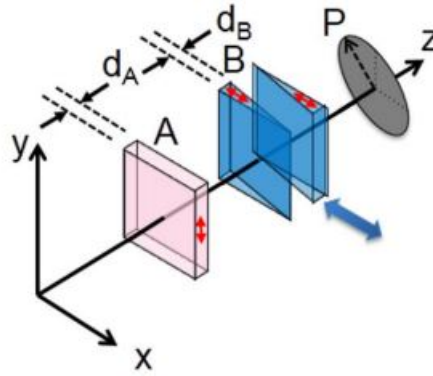


Figure 2.4: Schematic of TWINS [10].

The principle of TWINS is graphically depicted in figure 2.4. Two blocks *A* and *B* consist of a birefringent uniaxial crystal known as calomel (Hg_2Cl_2). It has a very high birefringence ($n_e - n_o = 0.55$). n_e and n_o are the refractive indices that a certain polarization of the incident light will follow. Light whose polarization is perpendicular to the optic axis is known as the ordinary axis and follows n_o . Light whose polarization follows the direction of the optic axis is governed by n_e and is called the extraordinary axis. The two blocks are rotated perpendicularly 90° relative to each other and perpendicular to the beam propagation. Block *B* is split into two wedges with same apex angle. The input beam is first polarized at 45° before coming into contact with block *A*. Block *A* introduces a fixed delay for both the extraordinary and ordinary axis. Block *B* introduces an inverse delay relative to block *A* resulting in zero delay for one. Movement between the wedges allows for fine tuning of the delay. A polarizer at the end recombines the two polarizing states creating the interferogram at the detector in the time domain.

The delay variation (Δt) between the two interferometer designs can be compared as follows:

$$\Delta t_{TWINS} = \frac{1}{G} \frac{2\Delta L}{c} \quad (2.2)$$

where ΔL is the displacement of the translation wedge of the TWINS. For comparison, the Michelson has a delay variation (δL) that follows:

$$\Delta t_{MI} = \frac{2\Delta L}{c} \quad (2.3)$$

where ΔL is the translation of the moveable mirror. G is known as the Gear ratio and it differentiates the two.

Gear ratio:

$$G = \frac{2}{(n_{ge} - n_{go}) \tan(\alpha)} \quad (2.4)$$

n_{go} & n_{ge} are the group index of the extraordinary and the ordinary axis and α is the apex angle between the wedges. Increasing the Gear ratio increases the resolution of the interferometer. Therefore a trade off exists in choosing the birefringent crystal material for a broad transparency range or for higher resolution. Calomel offers a $\Delta\lambda = \lambda/600$ which is sufficient for the spectral measurements in the *NIR-SWIR* for this project [10]. $\Delta\lambda$ represents the smallest resolvable wavelength difference. It is a resolution indicator for any spectrometer as introduced in equation 2.1.

2.1.2 Beer-Lambert Law

The Beer-Lambert law describes the attenuation of light due to absorption as it passes through a medium. It is the model used in absorption spectroscopy to link concentrations of an absorbing molecule to the transmission of light detected at the output. It can be written as follows:

$$I = I_0 10^{-\epsilon c L} \quad (2.5)$$

I_0 is the initial intensity incident on the volume and I is the output intensity of the volume. Therefore, the fraction of $I/I_0 = T$ is the complete transmission percentage at the output. ϵ corresponds to the molar absorptivity, also known as the molar extinction coefficient (typically known for tissue chromophores). It measures how a molecular species attenuates light at a certain wavelength and its units are $mM^{-1}mm^{-1}$. c is the molecular concentration of the absorbing molecule with units in mM . L describes the path length of the light in mm .

Absorption characteristics of a species is sometimes described with absorbance. This is a unitless parameter and is connected to the Beer-Lambert law as follows:

$$T = 10^{-\epsilon c L} = 10^{-A} \quad (2.6)$$

It is clear that absorbance is nothing more than transmission via natural logarithm. A further important parameter can be derived from the Beer-Lambert equation that will be used throughout the rest of this thesis. This is the absorption coefficient (μ_a).

$$T = 10^{-\mu_a L} = 10^{-A} \quad (2.7)$$

In this equation, μ_a is found in mm^{-1} but will be converted and expressed in cm^{-1} through the rest of this thesis. A few simplistic but important relationships can be extrapolated between these parameters. μ_a is wavelength dependent due to its relationship with ϵ and increases linearly

with concentration as:

$$\mu_a(\lambda) = \sum_i \epsilon_i(\lambda) c_i \quad (2.8)$$

The distance traveled by the photon is directly related to the absorption and the concentration and thus is linked to $\mu_a(\lambda)$ by:

$$l_a = \frac{1}{\mu_a(\lambda)} \quad (2.9)$$

Equation 2.8 is an important conclusion of using absorption spectroscopy as method of analytical chemistry. Quantitatively this reveals that studying a broad range of wavelengths gives an identifiable profile to a chemical species. Measuring individual wavelengths with higher resolution can reveal a qualitative assesment of chromophore concentration. Since all chromophores will contribute to μ_a , a basic assumption of only a few absorbers present is required.

2.2 Absorption Spectroscopy of Glucose solutions

The absorption spectrum of glucose is a consequence of its chemical composition ($C_6H_{12}O_6$). For *SWIR* spectroscopy the combination band and the first overtone band is of interest. The first overtone band is a product of $C-H$ stretching vibrations. The combination band meanwhile is so called as it is a byproduct of a combination of both stretching and bending vibrations of $C-H$ and $O-H$ bands. These three atoms are the building blocks for most organic compounds in nature. This makes glucose an ideal candidate to study for an analytical chemistry measurement.

2.2.1 Glucose Spectrum

A solution of glucose in deionized *Milli-Q*TM water was used to measure $\epsilon(\lambda)$ of the glucose spectrum. The concentration used was 24.7g of glucose in 50ml of water. Therefore the ratio of glucose in the bulk solution is 24.7g/50ml.

The glucose concentration must be converted to *mM* to agree with the Beer-Lambert law. *g/ml* can be converted to *mg/dL* easily and simply dividing by 18 converts the value to *mM*. Therefore 24.7g/50ml is converted to 49400mg/dL and dividing by 18 equates to 2744mM.

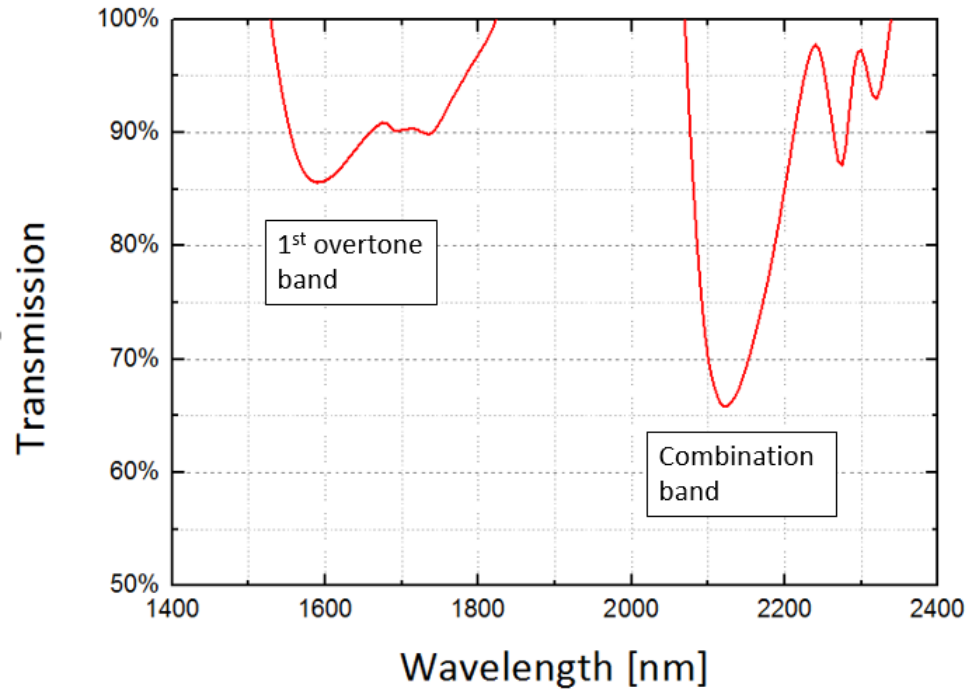


Figure 2.5: Glucose Spectrum found from onsite spectrometer, Cary 5000 UV-Vis-NIR.

The solution was placed in 1mm cuvette and placed in a commercial Carry 5000 UV-Vis-NIR spectrometer to measure the transmission profile. First a cuvette full only of the water used in the solution was baselined. This removes the absorption influence of water interfering with the glucose transmission spectrum. The transmission measurement found covering both the first octave and combination band is displayed in figure 2.5.

The transmission profile for the glucose peaks can now be used via the Beer-Lambert law (eq.2.5) to calculate $\epsilon(\lambda)$. For comparison, $\epsilon(1.59\mu m)$ and $\epsilon(2.1\mu m)$ will be calculated for the two main peaks in both the first octave band and the combination band. The optical path length through the cuvette is 1mm

1.59 μm Transmission is 85.6%:

$$\log_{10}(T) = -\epsilon(1.59\mu m)cL \quad (2.10)$$

$$\epsilon(1.59\mu m) = \frac{\log_{10}(0.856)}{(2744mM)(1mm)} = 2.5 \times 10^{-5}mM^{-1}mm^{-1} \quad (2.11)$$

2.1 μm Transmission is 65.9%:

$$\log_{10}(T) = -\epsilon(2.1\mu m)cL \quad (2.12)$$

$$\epsilon(2.1\mu m) = \frac{\log_{10}(0.659)}{(2744mM)(1mm)} = 6.5 \times 10^{-5} mM^{-1}mm^{-1} \quad (2.13)$$

Therefore, Glucose absorbs ≈ 3 times more in the combination band. In some literature it is noted up to 4-5 times more [11]. Hence the motivation for targeting the $2.1\mu m$ peak.

2.2.2 Water Spectrum

Water (H_2O) makes up 60% of the human body and is the main interfering molecule competing with glucose detection in human tissue for the *NIR-SWIR* range. However two windows of lower water absorption do exist from $1400 - 1850nm$ and $2000 - 2400nm$. These both correspond with the first overtone band and the combination band of glucose. This is match makes it ideal to target glucose in the human tissue in the *NIR-SWIR* range.

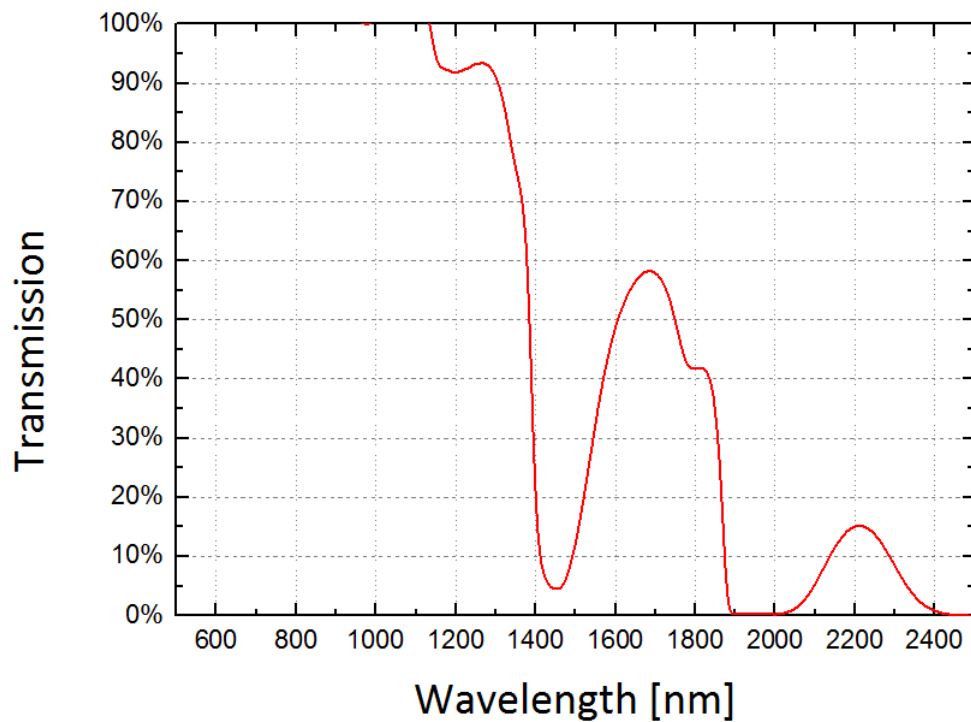


Figure 2.6: Deionized water transmission spectrum obtained from on-site commercial Carry UV-Vis-NIR spectrometer.

Outside of water, in real *in-vivo* biological samples, there are other biomolecules that can play a role in interfering with the detection of glucose. *Amerov et al* from the chemistry department of the University of Iowa published molar absorptivity data of these interfering biomolecules in

the first octave and combination bands which is plotted in figure 2.7. The molar absorptivity for glucose is slightly higher than water in the first overtone and combination band and higher than the other interfering molecules at the peaks of interest $1.59\mu m$ and $2.1\mu m$. Similar concentrations of these biomolecules as glucose could render glucose detection difficult. This is complex and depends on an individual's metabolism [11]. For this project, these interfering molecules are not present. Glucose is the only chromophore outside of water. The goal of this thesis will be to try and detect glucose concentrations in an environment where water has a much higher concentration.

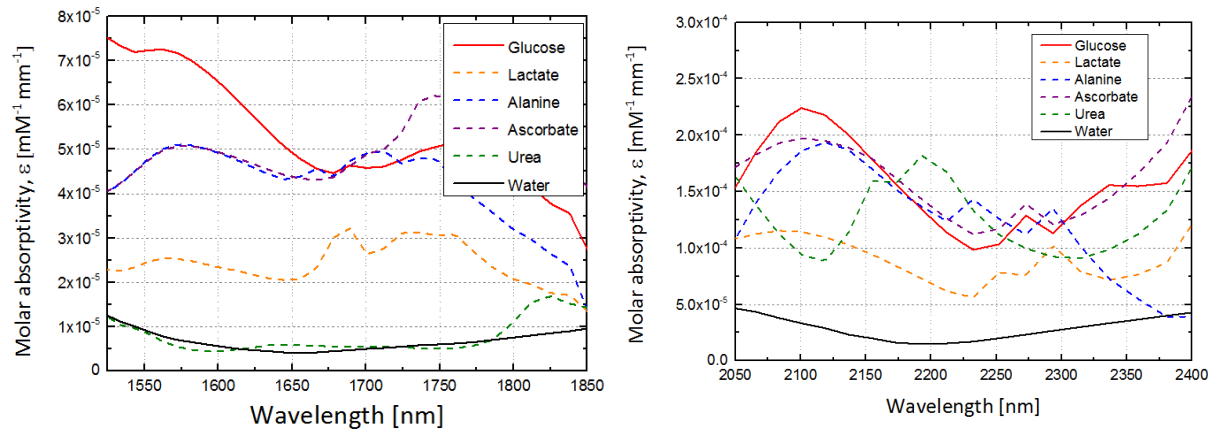


Figure 2.7: Molar absorptivity $\epsilon(\lambda)$ for interfering biomolecules in (a) the first octave band and (b) the combination band plotted with data from *Amerov et al.* [11]

2.2.3 Theoretical Signal-to-Noise Ratio

The following section is based upon research reported by *Ryckeboer E.* [5]. An optimal path length exists between the source and collection fiber that is characterized by the signal-noise ratio (SNR). In simple terms if the collection fiber is too far from the source fiber absorption of the water will dominate and any signal with glucose absorption information will be lost. However, if it is too close the signal will be very strong but with minimal information resulting from contact with glucose molecules. Therefore, a trade-off exists which dictates an optical path length.

A method to derive the minimally required SNR to detect glucose peaks for diabetic patients can be devised. The first step is defining the accepted medical concentration range of glucose that must be detectable by a device in a patient. Glucose concentrations in healthy patients usually sit in the range between 4.5mM – 6.8mM which can rise to $\approx 7.5\text{mM}$ after meals. A diabetic can exhibit concentration levels from 9mM to much as 20mM and is known as *hyperglycemia*. On the opposite side of the detection scale a condition exists where patients can exhibit abnormally low levels of glucose. This condition is known as *Hypoglycemia* and it is a consequence of concentration levels reducing below 4.5mM and plateauing at 3mM . Therefore a glucose concentration dynamic range for the in-vivo sensor can be defined for 3mM – 20mM . Clinically it is required for a medical device to have an absolute minimum resolution of 1mM [6].

The Beer-Lambert law is used to relate the optical path length and water absorption in the solution. The sensitivity of transmission by varying the concentration is:

$$s_i = \left| \frac{\delta T}{\delta c_i} \right| = T \ln(10) \epsilon_i L \quad (2.14)$$

To find the optimal sensitivity allow $\frac{\delta s_i}{\delta L} = 0$

$$L_{opt}(\lambda) = \frac{1}{\ln(10) \sum_{i=1}^n \epsilon_i c_i} \quad (2.15)$$

Water is the dominating factor in the absorption summation in the denominator. Optical path lengths are calculated as $L_{opt}(1.59\mu m) = 1.36mm$ and $L_{opt}(2.1\mu m) = 0.37mm$.

Using these lengths, a change in transmission due to a glucose solution can be calculated via an alternate form of the Beer-Lambert law:

$$T = 10^{-A_g} \quad (2.16)$$

Where A_g is the absorbance due to diluted glucose with a concentration c_g in a water solution. It is length dependent. A water displacement factor (f_w) corresponding to the molar concentration change of water caused by the dissolution of a unit molar concentration of a solute is taken into account. For glucose f_w is 6.245 [11].

$$A_g = \epsilon_g c_g L - f_w \epsilon_w c_w L \quad (2.17)$$

Therefore the change in transmission ΔT caused by diluting $1mM$ of glucose at wavelengths of $1.59\mu m$ and $2.1\mu m$ is calculated as:

$$\Delta T(1.59\mu m) = 1 - T_{1mM} = 0.01\% \quad (2.18)$$

$$\Delta T(2.1\mu m) = 1 - T_{1mM} = 0.008\% \quad (2.19)$$

The equivalent SNR is the reciprocal of ΔT . Therefore the $SNR(1.59\mu m)$ and $SNR(2.1\mu m)$ are respectively 10,000 and 12,500. This defines a sensitivity benchmark for the sensor device from its noise floor if it is to be a medically accepted device.

2.3 In-Vitro Tissue Like Optical Phantoms

Optical phantoms are used to mimic the scattering and absorption properties of a target in-vivo biological sample. The contents can range in complexity pending the body area and depth of interest. However, the vast majority seem to be comprised of oils and fats such as interlipids with ink in a bulk water solution. Interlipids are added to induce scattering properties and ink is for absorption.

Composition	Lipofundin MC-T/LCT 10%	Lipofundin MC-T/LCT 20%
Soya oil	50g	100g
Medium-chain triglycerides	50g	100g
Glycerol	25g	25g
Egg lecithin	8g	12g

Table 2.1: Composition of 1000ml of both Lipofundin MCT/LCT 10% 20% emulsions in bulk water [14].

Table 2.1 describes the composition in weight of both Lipofundin MCT/LCT 10% and 20% in a 1000ml emulsion volume. This was the mix used to modify the scattering in this thesis. These values were found on the brand website of the Lipofundin, i.e Braun [14]. Soya oil and medium-chain triglycerides are fats that combine as soybean oil. The glycerin dissolves into individual molecules in the bulk water solution and has no effect on scattering. The scattering component of Lipofundin MCT/LCT is due to the soybean oil encapsulated in a thin monolayer membrane of egg lecithin. lecithin is a type of lipid. This membrane spans a $2.5 - 5nm$ where the diameter of the soybean particle is on average between $25 - 75nm$, see fig (2.9). This scattering particle is known as the intralipid, which literally translates to inside the lipid. This is the reason Lipofundin is known as 10% or 20% as the concentration on the scattering intralipid component represents 10% or 20% of the bulk water emulsion. It is worth noting only half of the lecithin encapsulates the soybean oil the rest forms bilayer aqueous vesicles which do not impact the scattering [20]. A schematic interpretation of this can be observed in figure 2.8.

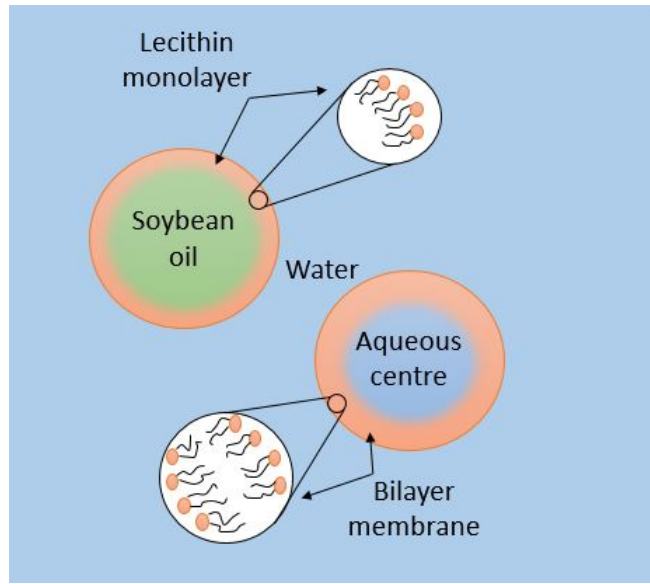


Figure 2.8: Schematic of interlipid scattering particles in Lipofundin MCT/LCT 20% as described in *Van Staveren et al.* [20].

Figure 2.9 displays the scattering particle diameter distribution in Lipofundin MCT/LCT 10%. It was plotted using data from *Van Staveren et al.* [20]. This group conducted in-depth research in 1991 to characterize the scattering properties of Lipofundin. As mentioned the scattering properties are highly dependent on the size of the particle and its concentric shape. They used a freeze fracture method to unlock the particle size information with an electron microscope. From this they found almost 50% were in the $25nm$ range, 25% at approximately $75nm$ and over 24% ranging from $125 - 450nm$. This is important information when calculating the reduced wavelength dependent scattering coefficient, μ'_s , further in the thesis. It is important to state that other literature *Kuntsche et al.* has studied lipofundin MCT scattering particles size via cryo electron microscopy [19]. They found a mean distribution size to be between $350nm$ and $400nm$. This would affect the scattering properties of the phantom especially for longer wavelengths. The concentration of Lipofundin-20% in bulk *Mili - QTM* deionized water will be diluted to a concentration of 6%. This concentration will be used to calculate scattering properties of the optical phantom.

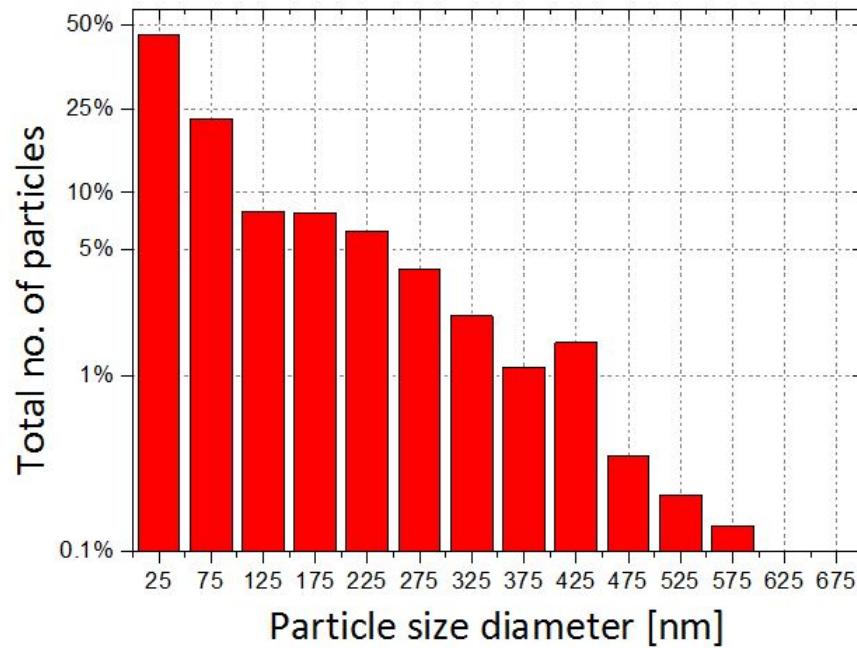


Figure 2.9: Particle size distribution of Lipofundin MCT. Graph based on data from [24]

2.4 Diffuse Reflectance Spectroscopy

Light has long been used to gain information into biological tissue. The discovery of *NIR* biological window occurred in the 1970's when Jobsis observed a deep penetration of light in the range of $650nm$ to $950nm$ [12],[13]. This was due to low absorption properties of water and hemoglobin at these wavelengths. However, how photons propagated through a scattering medium was still not clear. It is now well accepted that this propagation can be described well via diffusion [15]. The model, crucially, allows a quantitative separation of the tissue scattering and tissue absorption information. Using this model to gain clinically relevant knowledge about the physiological composition of tissue is known as diffuse optical spectroscopy. It provides the opportunity to obtain non-invasive measurements. In modern medicine it is used to measure in-vivo tissue hemodynamics to assess quantitatively concentrations of oxy- and deoxy-hemoglobin [17].

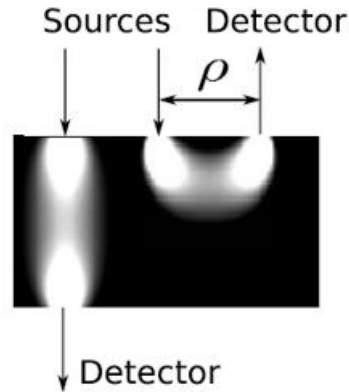


Figure 2.10: Reflection vs transmission [16].

Two types of diffusion detection in a volume exist reflection and transmission (fig.2.10). Reflection is usually implemented via a source fiber providing illumination on the tissue and a collection fiber positioned at a certain distance away (ρ) collecting the scattered output. This thesis will concentrate on reflection mode wherein the light that is reflected or scattered back through the medium will undergo spectroscopic analysis [16], [17].

2.4.1 Optical Propagation Path

The photon trajectory in biological tissue is heavily affected by scattering that can be described via the scattering coefficient μ_s . Two elastic scattering regimes are relevant in biological tissue, Mie scattering and Rayleigh scattering. Which one dominates is governed by the incident wavelength of light, the size of the scattering particle and the complex refractive index or the absorption properties of the surrounding medium. A unitless size parameter can relate the regime with particle size and wavelength of light:

$$x = \frac{2\pi r}{\lambda} \quad (2.20)$$

Where r is the radius of the scattering particle. Mie scattering is dominant when the wavelength is on a comparable scale relative to the diameter of the particle ($x \sim 1$). Rayleigh scattering takes over as the wavelength increases further ($x \ll 1$), see fig. 2.11. In biological tissue Mie scattering is the dominant process for wavelengths ranging from the *VIS* to *NIR*.

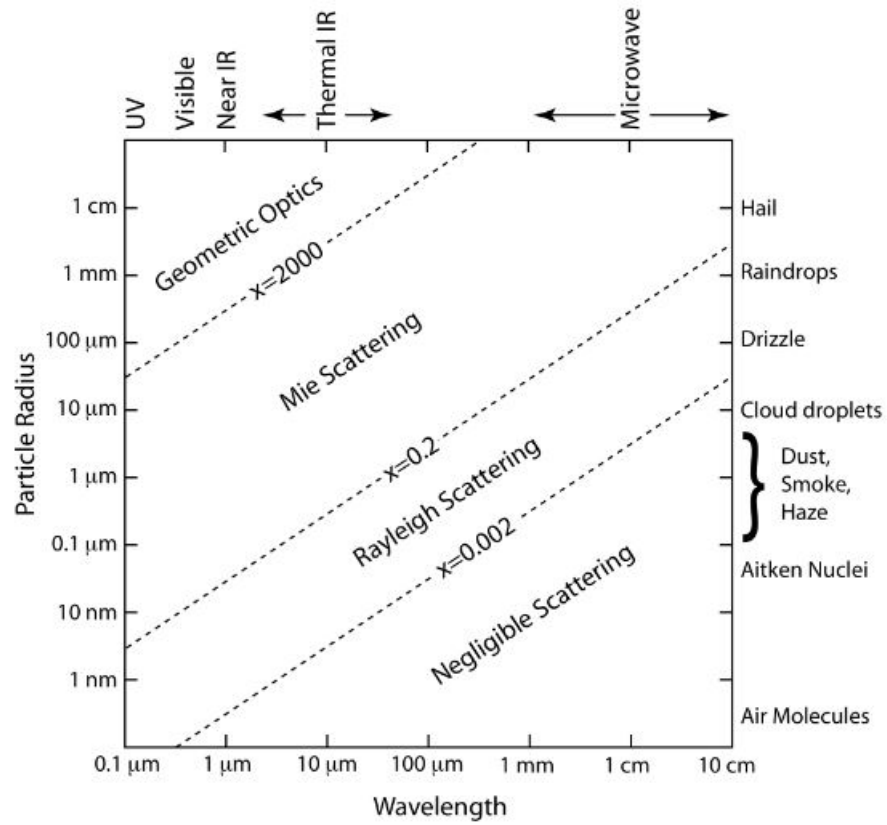


Figure 2.11: Light scattering regimes with respect to wavelength and particle size [16].

Mean free path

The mean free path is the average distance a photon travels before a scattering event occurs. It is the equivalent to the reciprocal of μ_s . However to describe the diffusion of photons before their direction is randomized, a longer *transport mean-free path* or *random walk step* is used. This distance is simply the reciprocal of a reduced scattering coefficient μ'_s :

$$l_{MFP} = \frac{1}{\mu'_s(\lambda)} \quad (2.21)$$

Where the reduced scattering coefficient is related to the scattering coefficient via an anisotropic value g as follows:

$$\mu'_s(\lambda) = \mu_s(\lambda)(1 - g) \quad (2.22)$$

The anisotropy factor g , is the ensemble average of the cosine of the scattering angle θ , i.e $g = \langle \cos\theta \rangle$. The range of $-1 \leq g \leq 1$ ranges from backscatter or reflection, to isotropic scattering or Rayleigh scattering, to forward scattering or Mie scattering as depicted in figure 2.12 [16]. In figure 2.12, the orange represents the probability of direction of propagation of scattering.

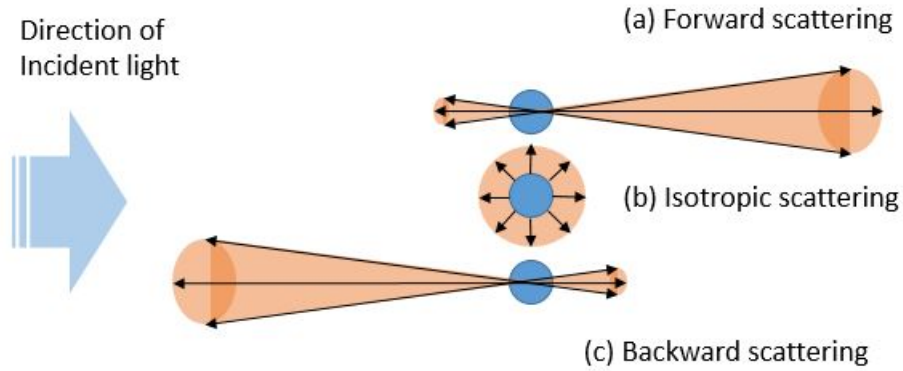


Figure 2.12: Schematic of scattering regimes (a) Forward ($g > 0$), (b) Isotropic ($g \approx 0$) & (c) Back scattering ($g < 0$).

Scattering angle

The scattering orientation can be described using the Henyey-Greenstein function. This is a phase function that describes the intensity probability distribution of the scattering event [23].

$$p(\theta) = \frac{1}{4\pi} \frac{1 - g^2}{[1 + g^2 - 2g\cos(\theta)]^{\frac{3}{2}}} \quad (2.23)$$

The function is normalized such that the integral over 4π steradians is unity:

$$\int_0^{2\pi} \left\{ \int_0^\pi p(\theta) \sin(\theta) d\theta \right\} d\theta = 1 \quad (2.24)$$

Simulations via MATLAB were created to display the Henyey-Greenstein phase function for contrasting g factors over a range of angles from $-\pi$ to π . From literature, biological samples can have a g factor from $0.6 - 0.98$ [16]. Therefore for contrast the isotropic $g = 0$, and $g = 0.98$ were simulated and also plotted in polar coordinates, see figures 2.13 & 2.14.

Photon reduced albedo

The final element to take into account to formulate a model of diffuse photon propagation in a scattering turbid medium is the photon absorption. The fraction absorbed is related to the scattering and absorbing coefficients as follows:

$$a' = \frac{\mu_s'}{\mu_a + \mu_s'} \quad (2.25)$$

a' is the reduced albedo. The closer it is to unity the greater results the diffuse approximation is expected to achieve. Therefore the diffuse approximation can be implemented when $\mu_s' \gg \mu_a$. As a rule of thumb, according to literature, μ_s' should be at least 10 times μ_a [[16], [20]]. Now, with the knowledge learned previously that the transport mean-free path and the absorption length are nothing more than the reciprocal of these coefficients, it is easy to see the absorption length of a photon must be at least 10 times longer than its transport mean-free path for the diffusion approximation to hold true.

Equipped with all this knowledge of functions and variables that describe a photon's trajectory in a turbid medium. Most literature describes using the Monte Carlo method to simulate light transport in tissue. The Monte Carlo method is a stochastic model that when provided with previously mentioned information, can calculate reflection, transmission rates and fluence rates in tissue [[22], [23]].

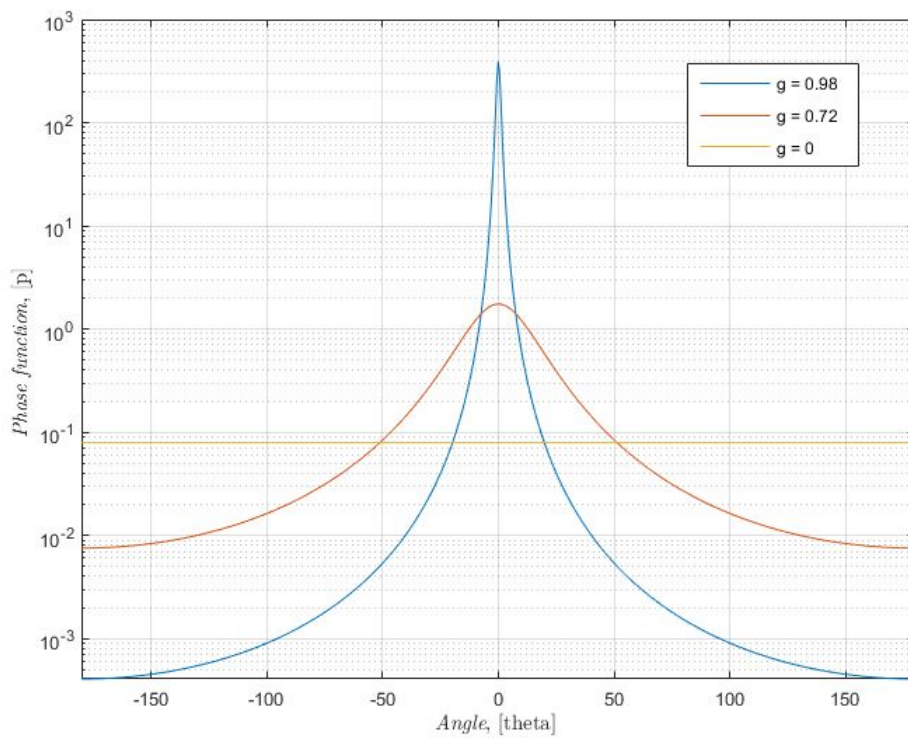


Figure 2.13: Henyey-Greenstein phase function simulation for contrasting anisotropic g factors.

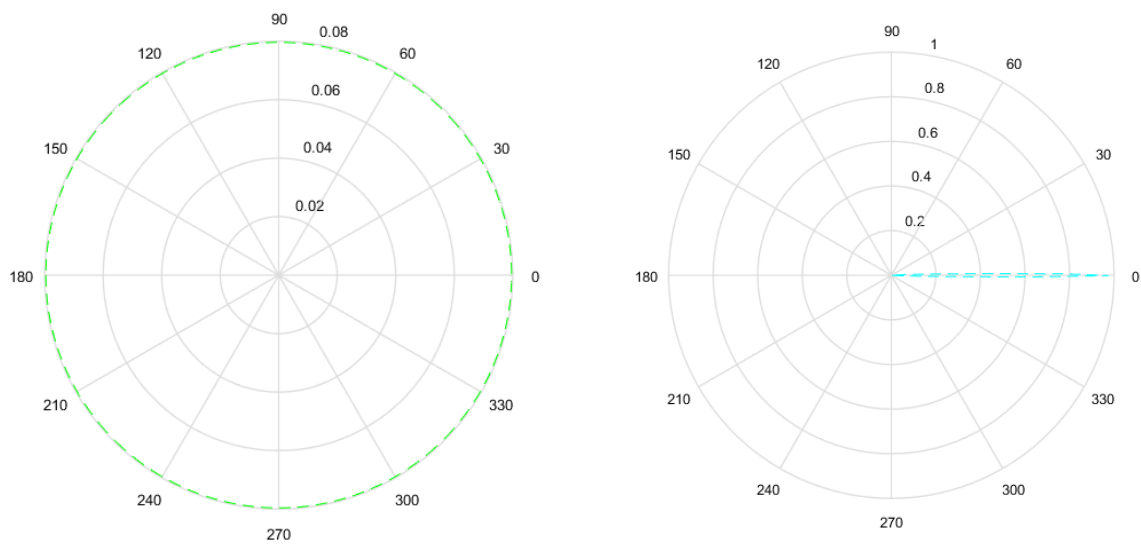


Figure 2.14: Polar plot simulations for (a) isotropic scattering of $g = 0$ & (b) forward scattering of $g = 0.98$

2.4.2 Distance Decay

The distance decay model is a technique of extracting the concentration information from a known chromophore absorbing in a scattering turbid media. Therefore it is the final crucial step towards spectroscopy. The exponential decay of intensity observed while moving the collection fiber away from the source fiber can be mathematically modeled as:

$$I(\rho) = \frac{I_0 e^{-\mu_{eff}(\lambda)\rho}}{\rho^2} \quad (2.26)$$

Where $I(\rho)$ is the intensity measured for a fiber separation distance ρ , I_0 is the initial source intensity and $\mu_{eff} = \sqrt{3\mu'_s(\lambda)\mu_a(\lambda)}$. It is clear a linear relationship exists between $\ln(\rho^2 I(\rho))$ and ρ via the linear slope which is $-\mu_{eff}(\lambda)$. It is possible to extract $\mu_a(\lambda)$ from $\mu_{eff}(\lambda)$ via:

$$\mu_a(\lambda) = \frac{\mu_{eff}^2(\lambda)}{3\mu'_s(\lambda)} \quad (2.27)$$

To use this method the absorption coefficients must be presumed constant by concentrating on an individual wavelength. Therefore a known absorption peak is chosen from a spectrum to analyze. Since μ_{eff} is a slope parameter that will be taken from a linear fitted graph and μ'_s is a parameter from the scattering media already known, μ_a is easily calculated. Knowing the molar absorptivity $\epsilon(\lambda)$ of the absorbing chromophore will decide the concentration information [29], [30].

$$c = \frac{\mu_a}{\epsilon} \quad (2.28)$$

2.5 Simulations of target glucose peaks

To have a stronger knowledge of the trials and challenges expected moving forward throughout the thesis it is important to create simulations of the models presented in section 2.2 for the absorption peaks and profiles for glucose and water (section 2.4). Although other glucose absorption peaks exist in both the first overtone band and the combination band, the main peaks of $1.59\mu m$ and $2.1\mu m$ will be chosen to represent possible detection simulations for both bands.

2.5.1 Lipofundin scattering

The scattering characteristics of Lipofundin MCT/LCT 20% will be found using data from two papers. This is the same database the Oregon Medical Laser Center (OMLC) uses to characterize optical phantoms based on Lipofundin MCT/LCT 10% [21]. The emulsion contents and

simple conversion of Lipofundin-10% to Lipofundin-20% have been described in section 2.3.

The first paper, *Flock et al.* [18], studied the optical properties on Lipofundin-10% via diffuse reflectance measurements with and without an added absorber in the *VIS* range from 460nm to 690nm. The second, Van Staveren et al. [20], also reported experimental measurements of light diffusion within Intralipid-10% with and without an added absorber from 400nm-1100nm (*VIS – NIR*). They also achieved an accurate correlation ($\approx 6\%$) between the theoretical anisotropic g factor from the Mie approximation and experimental retrieved g factor data from recording particle size distribution in lipofundin 10% (fig. 2.9).

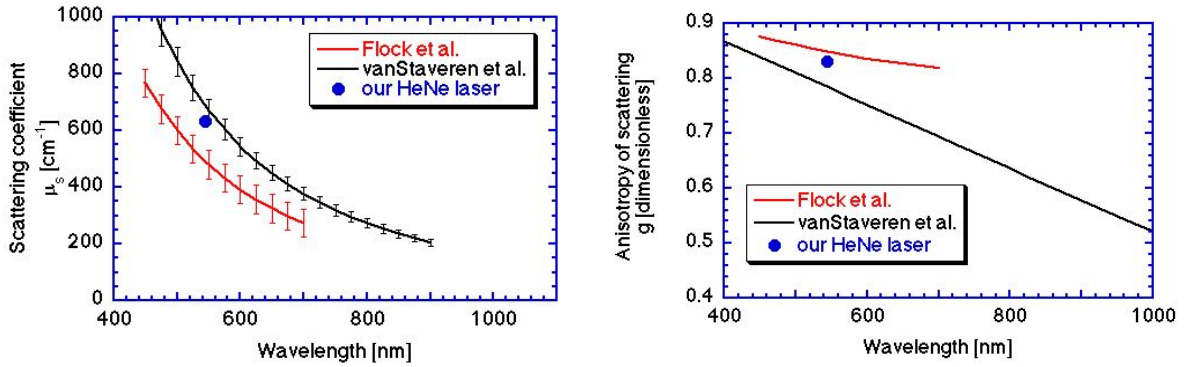


Figure 2.15: OMLC, *Flock et al.* & *Van Staveren et al.* characterization of Lipofundin MC-T/LCT 10% (a) Scattering coefficient μ_s & (b) the anisotropic factor g . [21]

Figure 2.15 (a) displays the μ_s vs λ spectrum from both bodies of research as well as a single λ HeNe source experiment provided by OMLC. Although the experimental data ceases in the *VIS – NIR* window, an extrapolation function can be used to follow the curve fittings of both to achieve contrasting μ_s value for the glucose peaks.

Flock et al. approximation is as follows:

$$\mu_s(\lambda) = 1.17 \times 10^9 (\lambda[nm]^{-2.33}) cm^{-1} \quad (2.29)$$

Mie theory approximation (*Van Staveren et al.*) is as follows:

$$\mu_s(\lambda) = 2.54 \times 10^9 (\lambda[nm]^{-2.4}) cm^{-1} \quad (2.30)$$

The $\mu_s(\lambda)$ will be multiplied by a factor of 0.12 to account for its concentration in bulk *Mili – QTM* water explained in section 2.3. 685nm scattering properties in Lipofundin are also found as this wavelength will be used in the first section of the project.

Wavelength	Flock approx. $\mu_s(\lambda)$	Mie approx. $\mu_s(\lambda)$	Flock approx. l_{MFP}	Mie approx. l_{MFP}
685nm	$34.68cm^{-1}$	$47.68cm^{-1}$	$0.03cm$	$0.02cm$
1590nm	$4.88cm^{-1}$	$6.32cm^{-1}$	$0.2cm$	$0.12cm$
2100nm	$2.55cm^{-1}$	$3.24cm^{-1}$	$0.4cm$	$0.3cm$

Table 2.2: μ_s & l_{MFP} values for 685nm, 1590nm & 2100nm for both approximations

2.5.2 Lipofundin anisotropic g factor

The anisotropic g factor (fig. 2.15 (b)) displays the decline of g with increasing wavelength for both papers. An extrapolated function is applied to both best fits again for the glucose peaks.

Flock et al. approximation is as follows:

$$g(\lambda) = 2.225(\lambda[nm])^{-0.155} \quad (2.31)$$

Mie approximation:

$$g(\lambda) = 1.1 - (0.58 \times 10^{-3})(\lambda[nm]) \quad (2.32)$$

Wavelength	Flock approx. $g - factor$	Mie approx. $g - factor$	Flock approx. $\theta_{90\%}$	Mie approx. $\theta_{90\%}$
685nm	0.81	0.7	23°	38°
1590nm	0.71	0.18	39°	-
2100nm	0.68	-0.12	42.5°	-

Table 2.3: Anisotropic g values & angle θ for 90% scattering of the light after the event for 685nm, 1590nm & 2100nm for both approximations

Once $g(\lambda)$ is found for both approximations, The Henyey-Greenstein function (eq. 2.23) is used to simulate the corresponding phase function in figure 2.16 (a) in log format.

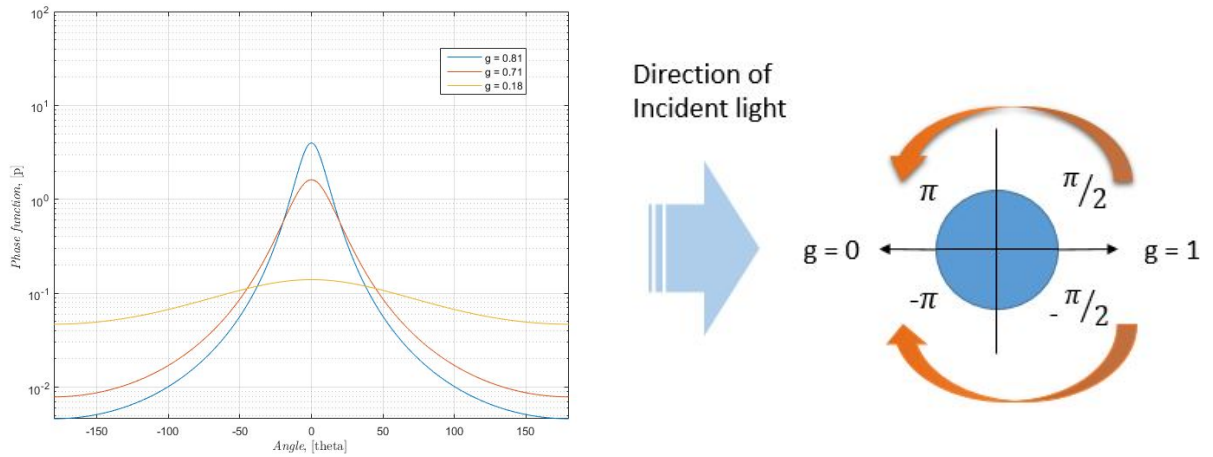


Figure 2.16: (a) Simulation via MATLAB of the phase function for different anisotropic $g(\lambda)$ factors for Lipofundin & (b) Schematic of corresponding physical representation

From the Henyey-Greenstein functions, to develop a simple map of the optical path a photon travels before meeting a collection fiber, a maximum scattering angle was chosen where 90% of the light is directed within. The 90% intensity is evenly split between both sides of the phase function from the peak so it is scattered equally in $+/-\theta$ directions (fig. 2.16). The angle $+\theta$ is used to plot this diffuse reflectance path to the collection fiber.

These angles are recorded in table 2.3 and their polar simulations are plotted in figure 2.17. Figure 2.17 (b) displays an interesting prediction by the Mie approximation in that for $g(1.5\mu m)$ it is almost isotropically scattering and for $g(2.1\mu m)$ it is beginning to displaying backscattering.

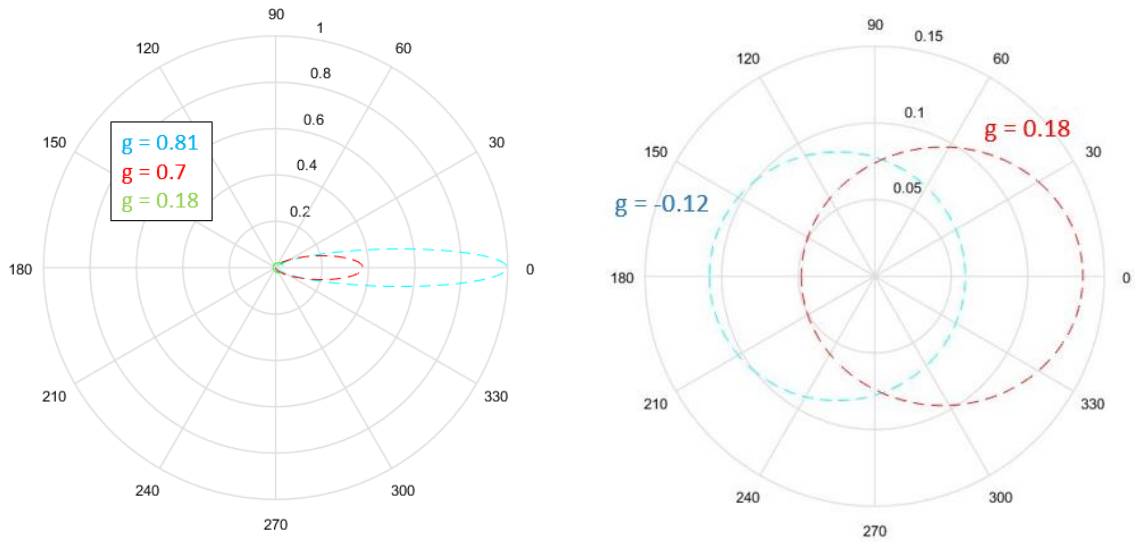


Figure 2.17: (a) Polar simulations via MATLAB of the anisotropic g factors scattering for Lipofundin & (b) Mie approximations for $g(1.5\mu m) = 0.18$ and $g(2.1\mu m)$

2.5.3 Lipofundin reduced scattering coefficient

All the information is now available to calculate the reduced scattering coefficient and its reciprocal transport mean-free path for each case from eq. 2.22. They are calculated in 2.4 as follows:

Wavelength	Flock approx. $\mu'_s(\lambda)$	Mie approx. $\mu'_s(\lambda)$	Flock approx. l_{TMFP}	Mie approx. l_{TMFP}
685nm	$6.59cm^{-1}$	$14.3cm^{-1}$	0.15cm	0.07cm
1590nm	$1.42cm^{-1}$	$5.18cm^{-1}$	0.7cm	0.19cm
2100nm	$0.82cm^{-1}$	-	1.21cm	-

Table 2.4: μ'_s & l_{TMFP} values for 685nm, 1590nm & 2100nm for both approximations

2.5.4 Fiber separation approximation

A simple model for the minimum separation distance between the source and collection fiber can be developed with knowledge of l_{TMFP} and the scattering angle $\theta_{90\%}$. A simple regular polygon geometry is assumed for the reflection geometry of the photon path. l_{TMFP} represents the polygon side length and the exterior angle θ_{ext} is the scattering angle $\theta_{90\%}$. The number of

sides n of the regular polygon is calculated by:

$$\theta_{int} = \frac{180^\circ(n-2)}{n} \quad (2.33)$$

Where $\theta_{int} = 180^\circ - \theta_{ext}$. The numerical aperture of the fibers (0.22) is used to calculate the diffraction angle of input and collection assuming the refractive index is ≈ 1.33 of the phantom:

$$\theta_{NA} = \sin^{-1}\left(\frac{NA}{n}\right) = 9^\circ \quad (2.34)$$

The radius of the polygon or the distance from the center to one of the polygon vertices is the same as $\rho/2$. Figure 2.18 displays a schematic of the simplistic model and was plotted for the Flock approximation at the $685nm$ wavelength.

$$R = \frac{l_{TMFP}}{2\sin\left(\frac{180^\circ}{n}\right)} \quad (2.35)$$

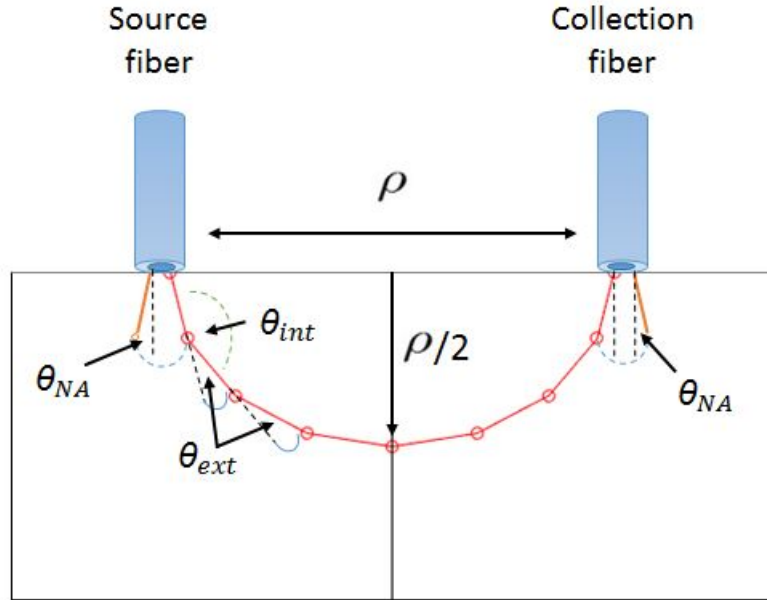


Figure 2.18: Schematic of fiber separation approximation model

The fiber separation approximation (ρ) for both models is calculated in table 2.5. Comparing these distances to the experimentally achieved values will provide a good indication of which approximation can be extrapolated accurately for Lipofundin into the *SWIR* window.

Appr.	Scattering length l_{TMFP}	Scattering angle $\pm\theta_{90\%}$	Scattering events n	Polygon radius R	Fiber sep- aration distance ρ
Mie (685nm)	0.7mm	38°	9.47	1.07mm	2.15mm
Flock (685nm)	1.5mm	23°	15.65	3.76mm	7.52mm
Flock (1590nm)	7mm	39°	9.23	10.5mm	21mm
Flock (2100nm)	12.1mm	42.5°	8.47	16.7mm	33.4mm

Table 2.5: Fiber separation distance approximations for both models for 685nm, 1590nm & 2100nm

2.5.5 Human tissue anisotropic g factor

One would expect the g factor of human tissue to decrease with higher wavelengths like any other turbid medium with fixed particle size distribution. For example if one chooses an intralipid solution to mimic the scattering properties of tissue in the visible it would be expected that the Mie approximation for a fixed particle size would follow for longer wavelengths. However it does not appear to follow this trajectory like the simple optical phantoms. As displayed in fig. 2.19 (a), it appears to increase in the VIS and plateau to a relative constant g value. This is evident in most literature where the usual wavelength dependent g parameter is expressed as a constant in the range of 0.6 - 0.98. This is a strange result that most likely is due to the complex multi-heterogenous environment of human in-vivo tissue. This should be taken into account when designing a phantom for a particular wavelength range.

Figure 2.19 (b) displays the wavelength dependent reduced scattering coefficients for human tissue. The research, by *Bashkatov et al.*, took the measurements from *in-vitro* tissue samples and. They used spectrophotometry with integrating spheres to achieve scattering as well as absorption information [9].

Ignoring chromophores in human tissue for a moment. These results show an important conclusion about the viability of diffuse reflection spectroscopy using the *SWIR* range to probe human tissue. It is theoretically possible. The reduced scattering coefficient of human tissue displays a small slope as it approaches $2\mu m$.

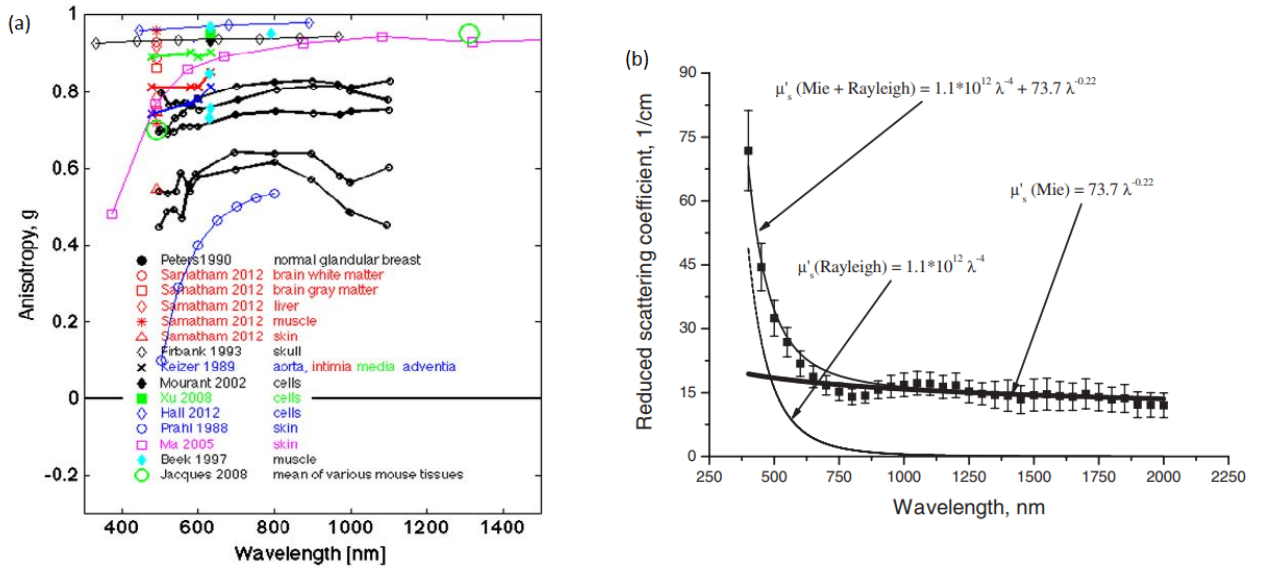


Figure 2.19: (a) Wavelength dependent anisotropic g values for human tissue for contrasting studies [8] & (b) the wavelength dependent reduced scattering coefficient for human tissue [9].

2.6 Glucose Sensor Based on a Broadband Flexible Detector

For continuous diabetic measurements as described in the introduction, a detector that can be applied to human tissue with ease and minimal discomfort must be realized. Presented in the following section is a detector that was designed, patented and manufactured at ICFO. It has the capabilities to overcome the limitations presented and possibly offer the sensitivity to detect the target glucose peaks of $1.59\mu m$ and $2.1\mu m$ of the first overtone and combination bands.

2.6.1 Integrating an electrically active colloidal quantum dot photodiode with a graphene phototransistor

Most commercial photodiodes are designed from semiconductor physics. This hybrid photodetector is an integration of colloidal quantum dots (CQD), acting as the photodiode, on top of a graphene amplifying layer. The result is a broadband device that can stretch from the *UV - NIR* range ($300nm - 3000nm$).

The external quantum efficiency (EQE) is a measure of a device's ability to transfer photons that are incident on the device into electrons. The *EQE* can be tuned to as high as 75% and is only in principle limited by reflection. It has a sub *millisecond* temporal response and the noise floor is dominated by $1/f$ noise. It has a gain-bandwidth product in the order of 10^8 and a linear dynamic range of 110dB. Its sensitivity of figure can be characterized via the specific detectivity value and is $D^* = 1 \times 10^{13} J$.

The hybrid detector is compatible with a number of contrasting substrate materials. It can be integrated with a *Si* substrate to make it compatible with *complementary metal oxide semiconductors* (CMOS) technology. It has the diversification to integrate with *sapphire* developing rigid transparent devices. As mentioned, in interest of medical applications, the device can be integrated with flexible transparent polymer that is conformal to human skin. This paves the way for research design into medical patch detectors [3], [4].

2.6.2 Sensor Configuration

The broadband characteristic of the device is due to the absorption of the *CQDs*. This photodiode layer ($\approx 300nm$) absorbs the incident light and creates electron hole pairs. Without an external voltage applied a natural narrow depletion region exists at the interface between graphene and the *CQDs* ($80 - 90nm$). Holes in this depletion region will transfer into, and dope, the graphene layer via drift while holes outside of the depletion region will travel via diffusion (fig 2.20 (a)).

The graphene layers resistivity changes with doping. Therefore the change in resistance is directly proportional to the light incident on the device. Hence, the device is a resistive read out

circuit.

The EQE of this device design is $\approx 20\%$. However this can be improved by creating a gain effect by applying an external voltage. As displayed in figure 2.20 (a), An external bias voltage can be applied via a transparent top contact electrode or via a back gate electrode situated at the graphene interface. Increasing the voltage extends the depletion region in the $300nm$ thick CQD region and significantly enhances charge collection in the graphene layer. An optimum V_{TD} exists at $1.2V$ after which improves the EQE to $\approx 75\%$. Increasing the voltage further causes saturation. A EQE of 75% is the theoretical limit due to reflections at the Pbs-QD to ITO to air interface. Therefore in principle applying the optimum bias voltage achieves 100% charge collection efficiency.

The response curve of absorption follows the profile as displayed in figure 2.20 (b) and (c). Fabrication of the $CQDs$ dictates how far this spectral response reaches. The excitation peak observed at $920nm$ in 2.20 (b) and $1670nm$ in figure 2.20 (c) Can be tuned during fabrication of the $CQDs$ by changing their diameter. Therefore the excitation peak could potentially be tuned to the glucose absorption peaks of $1.59\mu m$ and $2.1\mu m$ for a specific device [3], [4].

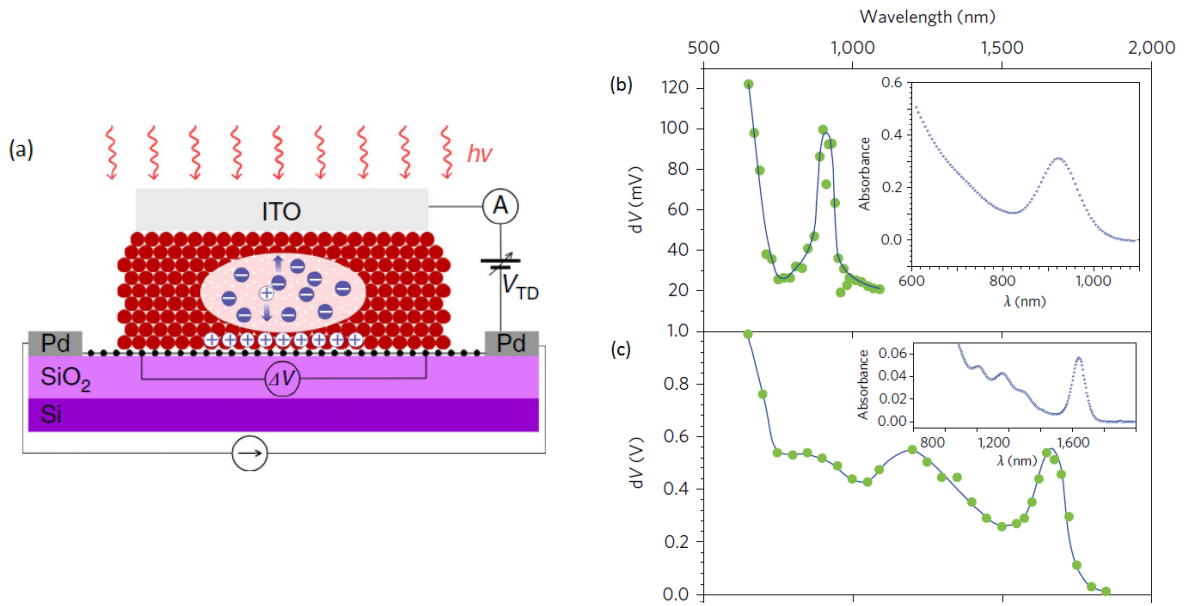


Figure 2.20: (a) Schematic of Pbs-QD & graphene hybrid photodetector [3] (b) Spectral dependence of the photoresponse of CQDs with an excitation peak of $920nm$ & (c) Spectral dependence of the photoresponse of CQDs with an excitation peak of $1,670nm$ [4]

2.7 Conclusion

Trying to detect glucose in a much larger volume of water in the *NIR-SWIR* window is a well documented problem and covered in-depth in this theoretical section. However an interesting unknown challenge moving forward with this research is the viability of Lipofundin MCT/LCT 20% as a proficient scattering medium to detect glucose wavelength peaks in the first overtone band and in the combination band.

As an optical phantom it mimics human tissue very well in the visible region but very little research has been conducted into its scattering properties after $1000nm$. The best model of prediction that can be applied is extrapolating the best fit from the data provided by *Flock et al.* and *Van Staveren et al.*. The factors $\mu'_s(\lambda)$ and the anisotropic $g(\lambda)$ factor dictate the scattering path of the photon and relative to $\mu_a(\lambda)$ of water in the phantom, determine if it is in a diffuse regime. The method that *Van Staveren et al.* used to calculate $g(\lambda)$ and $\mu'_s(\lambda)$ by freeze fracturing the scattering particles and calculating size distribution models is very comprehensive. Their results followed the Mie approximation of scattering with high accuracy. The extrapolation of this would mean the $1.59\mu m$ is at the extreme edge of detection via the diffuse model and $2.1\mu m$ cannot be detected.

It must be reminded that one comparative study, *Kuntsche et al.*, used cryo-electron microscopy to measure a mean diameter of $350 - 400nm$ of the Lipofundin scattering particle. This would greatly increase the chances of the $1.59\mu m$ and $2.1\mu m$ being detected via the diffuse reflection model if true. According to figure 2.11, a mean particle radius of $175 - 200nm$ would induce Mie scattering in the *SWIR* range of illumination ($1.59\mu m$ to $2.1\mu m$). Therefore there is a theoretical unknown moving forward whether the first overtone and combination band of glucose can be probed using diffuse reflection spectroscopy on Lipofundin MCT-20 as a diffuse medium. This must be experimentally explored.

There is not much theory available for the scattering properties of *in - vivo* human tissue in the *SWIR* range ($1100 - 2100nm$). The bulk of research has concentrated on the *near-infrared window* ($650 - 1300nm$) where water absorption is at its lowest. However it is interesting to find out that human tissue does not appear to follow the same Mie scattering trend as Lipofundin for higher wavelengths. Its scattering properties hold relatively well as it approaches the *SWIR* limit of $2.1\mu m$. Hence, ignoring the unknown effect of absorbing chromophores at this wavelength at this time, diffuse reflection spectroscopy is theoretically achievable for the $2.1\mu m$ wavelength in human tissue.

It is interesting to note that although $g(\lambda)$ is an intrinsic characteristic of the scattering particles spherical radius, $\mu'_s(\lambda)$ is related to concentration. Therefore, can be altered by increasing the volume of Lipofundin in bulk water. This could increase the chances of diffuse detection marginally. The low $g(\lambda)$ factor will still dictate that the scattering angles are closer to isotropic in all angles rather than forward. As the research moves forward, comparing the distance ρ between the source and collection fiber to the values theoretically calculated for both approximations in table 2.5 will allow access to a better understanding of Lipofundin scattering properties

in the *NIR-SWIR* range.

Chapter 3

Mapping the exponential decay in the visible spectrum

3.1 Introduction

Water exhibits maximum transmission in the *VIS-NIR* ($300nm - 1100nm$) spectrum as shown in fig. 2.6. It also offers the additional advancement of allowing visible access to alignment issues, troubleshooting possible construction problems of the initial experimental set-up. Gaining confidence of troubleshooting errors in the set-up at the beginning of the project is an important step to master as this will become more complex working in the non-visible NIR spectrum.

The goal of this part of the project is to design an experimental set-up that can be used to perform diffuse reflection analysis on phantom samples. This set-up will be the core structure for further sections of the project where extra elements will be combined.

3.2 Experimental set-up design

The separation distance between fibers as predicted by the *Van Staveren et al.* and *Flock et al.* approximations is *millimeters*. Therefore, for reproducibility and precise measurements, a system where distance (in x, y and z) between the source and collection fibers that are mechanically controlled on a *micrometer* scale is required.

The Stepper Motors

Four stepper motors were used to automate the relative movements between the fibers in the sample. To ensure mm resolution accuracy, movement steps of $2.5\mu m$ were chosen. Two motors were fixed to allow movement of both fibers in the z direction, both up (+) and down (-). The other two motors were fixed to allow control of the collection fiber in both the y and x directions (fig. 3.6). The x and y movements of the source fiber did not need to be mechanically controlled. The position of the source fiber can be manually chosen in the phantom, as the controlled movements of the collection fiber relative to the source fiber is what is important.

The stepper motor consists of a series of magnets surrounded by electromagnetic coils. Supplying the coils with current induces magnetic fields which repulses or attracts the magnets. This causes the shaft to rotate one direction or the other. The collection fiber and source fiber are built onto two position stages that can be moved in the x and y directions via micrometer screws. To manage this movement mechanically for the collection fiber position stage, the micrometer screws are connected to the rotational movements of the stepper motor shaft via timing belt pulleys and a rubber belt. Ensuring stiffness of the timing belts through the required movements provides a high level of accuracy and reproducibility.

The Arduino board controlling the voltage information that rotates the four motors is connected via USB to a computer. QTLab was used to code functions to control the automation. QTLab is a python based measurement environment.

The source

To prove the system runs correctly for diffuse reflection testing a visible source is used to ensure minimum absorption in the bulk $Milli - Q^{TM}$ water solution. Therefore a red visible laser source was chosen with a central wavelength of $685nm$ and a modulated power of $12mW$. The optical source chosen was a Thorlabs HL6750MG laser diode. The spectrum of which is detailed on the data sheet $\lambda_{min} = 675nm$ and $\lambda_{max} = 695nm$. The TWINS spectrometer was used to retrieve its spectrum in fig. 3.1. The central wavelength is slightly adrift at $682nm$ but λ_{min} and λ_{max} is $\pm 10nm$ from the central wavelength as expected. The laser source was modulated by an external frequency generator at $3KHz$ which is in parallel connected to a lock-in amplifier to extract the signal collected from the sample and minimize noise.

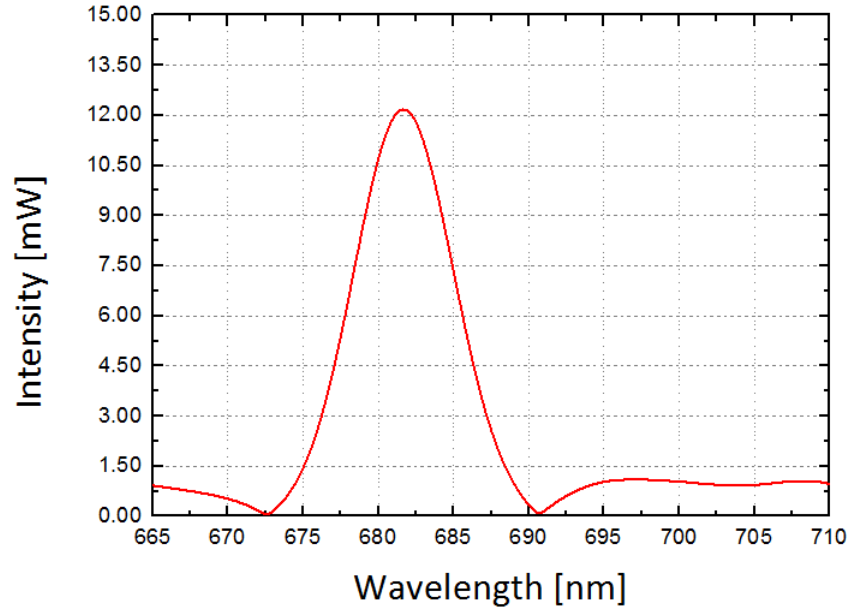


Figure 3.1: Spectrum of Thorlabs visible laser diode.

The phantom

The phantom concentration ratio is 6% Lipofundin MCT-20, 94% water mixed in a 60ml container as explained in chapter two, section 2.3. The reduced scattering coefficient at an illuminating wavelength of 685nm was previously calculated for this ratio as $\mu'_s(685nm) = 14.3cm^{-1}$ according to Mie approximation.

In this section the absorption properties, $\mu_a(\lambda)$, will be controlled via black china ink. The transmission profile is flat with a gradient that decreases slowly towards the shorter wavelengths. This was found for contrasting concentrations of dissolved ink in bulk water solutions via the commercial Carry UV-VIS-NIR spectrometer at ICFO. The concentration transmission profiles chosen to measure are 0.0001%, 0.001% and 0.01% (fig. 3.2). 0.001% of ink, 99.999% water is the ratio that will be used. From the transmission spectrum in figure 3.2, the Beer-lambert law can be used to derive $\mu_a(\lambda)$ for 685nm. Since the concentration black ink in the phantom is known, $\epsilon(685nm)$ can also be calculated. This value can be used to find $\mu_a(685nm)$ for different ink increments to test the exponential decay predicted by diffuse reflection spectroscopy.

Calculating the molar absorptivity of ink at 685nm:

The transmission of 0.001% concentration of ink at 685nm is 1.315% from figure 3.2. Using the Beer-lambert law (eq. 2.5):

$$\log_{10}(T) = -\epsilon(685nm)cL \quad (3.1)$$

The path length of the cuvette is $1mm$. The concentration can be converted to $0.05mM$ as descibed in chapter two, section 2.2.1. The molar absorptivity of black china ink becomes:

$$\epsilon(685nm) = -\frac{\log_{10}(0.01315)}{(0.05mM)(1mm)} = 37mM^{-1}mm^{-1} \quad (3.2)$$

Calculating the absorption coefficient of ink at 685nm

The 0.001% ink and water solution are added to the optical phantom in increments. The optical phantom is contained in a $60ml$ volume. μ_a must be calculated for an increment to understand the absorption properties of the phantom. Adding $1ml$ of the ink solution into the optical phantom will create a ratio mix of $1 \times 10^{-5}g/61ml$. This converts to an ink concentration of $0.01639mg/dL$. The units mg/dL can be converted into $mmol/L$ by dividing by 18. $mmol/L$ can be expressed as mM . This results in a concentration of $9.1 \times 10^{-4}mM$ of ink in the phantom. Therefore:

$$\mu_a(685nm) = \epsilon(685nm)c = (37.6mM^{-1}mm^{-1})(9.1 \times 10^{-4}) = 0.34cm^{-1} \quad (3.3)$$

This agrees well with biological tissue conditions and the diffusion model presented in chapter two, section 2.4. The reduced albedo a' becomes 0.98 and therefore satisfies the diffusion model in section 2.4.1.

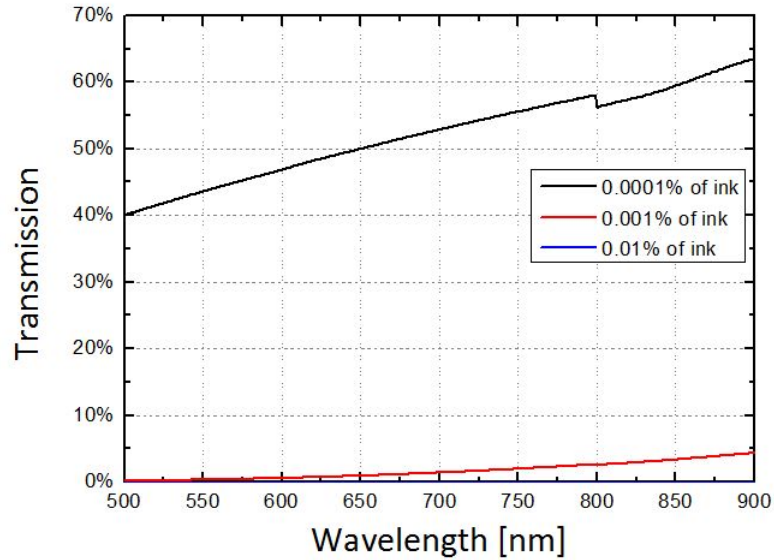


Figure 3.2: Transmission spectrum of black china ink for contrasting concentrations in bulk water solution.

The Detector

The PDA36A silicon based photodetector was used to collect the light from the sample and pass the modulated information to the lock-in amplifier. It is a switchable gain detector which allows the user to increment the gain in 10dB steps from 0dB to 70dB. It is designed to detect wavelengths from the visible into the NIR, from 350nm to 1100nm. It is a relatively fast device ($\tau = 35ns$) with a bandwidth of 10MHz. If operating at 70dB gain the bandwidth is 5kHz ($\tau = 70\mu s$). It has from the response curve in the figure 3.3, a responsivity of $\approx 0.38A/W$ for the 685nm output of the visible source [36].

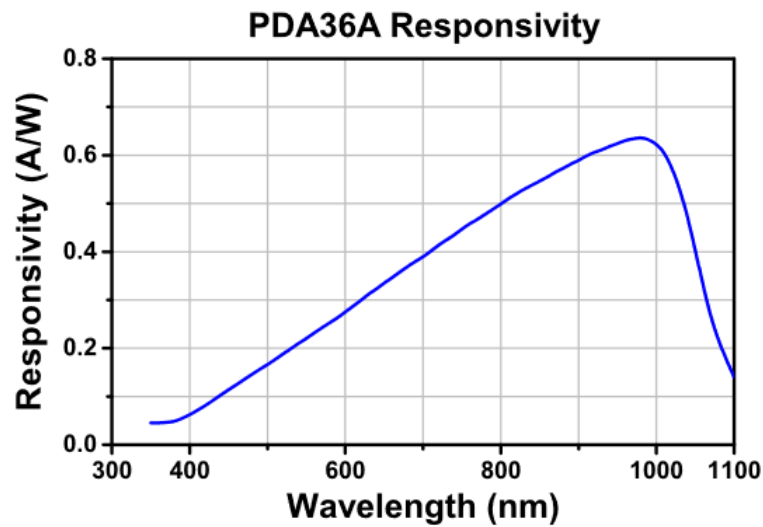


Figure 3.3: Response curve of the PDA36A Si photodetector [36].

3.2.1 The fibers

A predominant feature of the next stage of the project is coupling a broadband *NIR-SWIR* spectrum into the sample via the source fiber and into the TWINS via the collection fiber. Therefore using the correct multimode fiber with a broad transmission range is crucial. Thorlabs FG050LGA multimode fiber was chosen with the specific characteristics of a 0.22 numerical aperture, a $50\mu m$ core and a broadband transmission range of $0.4 - 2.4\mu m$.

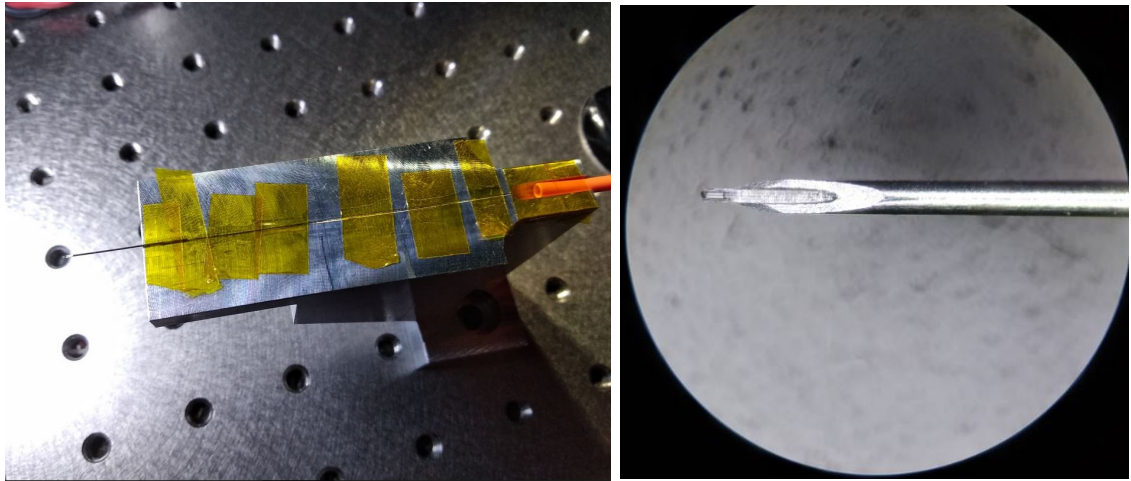


Figure 3.4: (a) Attachment of a stripped and cleaved fiber through a needle & (b) microscope image of the exposed fiber end.

The fibers are stripped to ensure minimum distance of separation in the sample is possible. The minimum theoretical separation distance between the fibers is cladding to cladding $100\mu\text{m}$ (fig.3.5 (a)). The end of the fiber is cleaved and the stripped component is cleaned with isopropyl alcohol (IPA). The stripped section is placed through a needle for protection and stiffness when moving through the phantom. The cleaved end of the fiber is fixed slightly protruding from the needle holder to ensure maximum illumination and collection in the phantom (fig. 3.4 (b)). In the final step they are securely fastened to the metallic block via thermal tape as shown in figure 3.4 (a), and connected back in the set-up as shown in figure 3.5 (b).

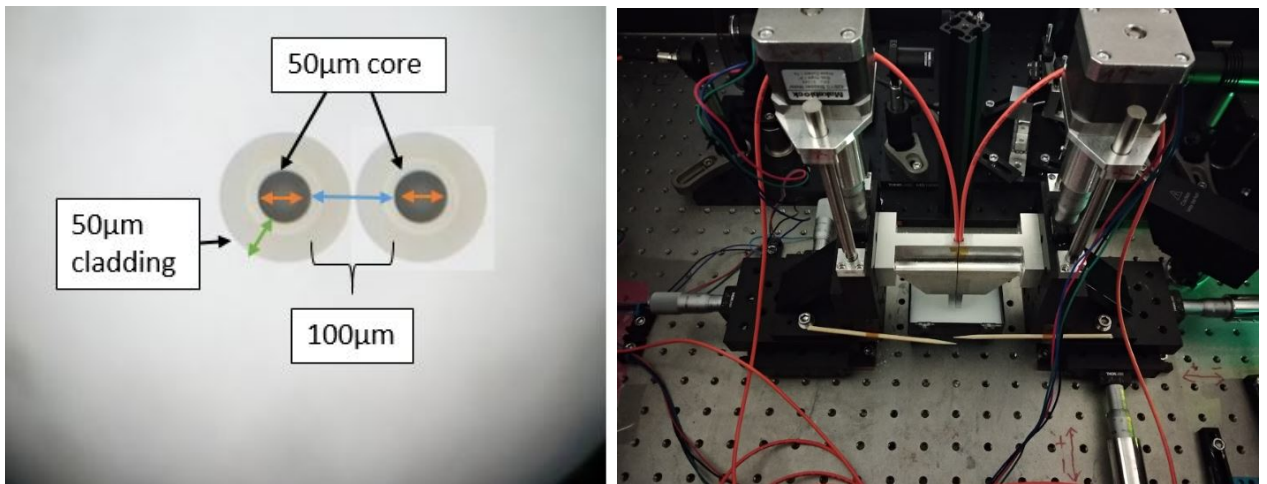


Figure 3.5: (a) Fiber microscope image of the minimum separation distance between two stripped fibers & (b) The final set-up of source and collection fiber in an optical phantom.

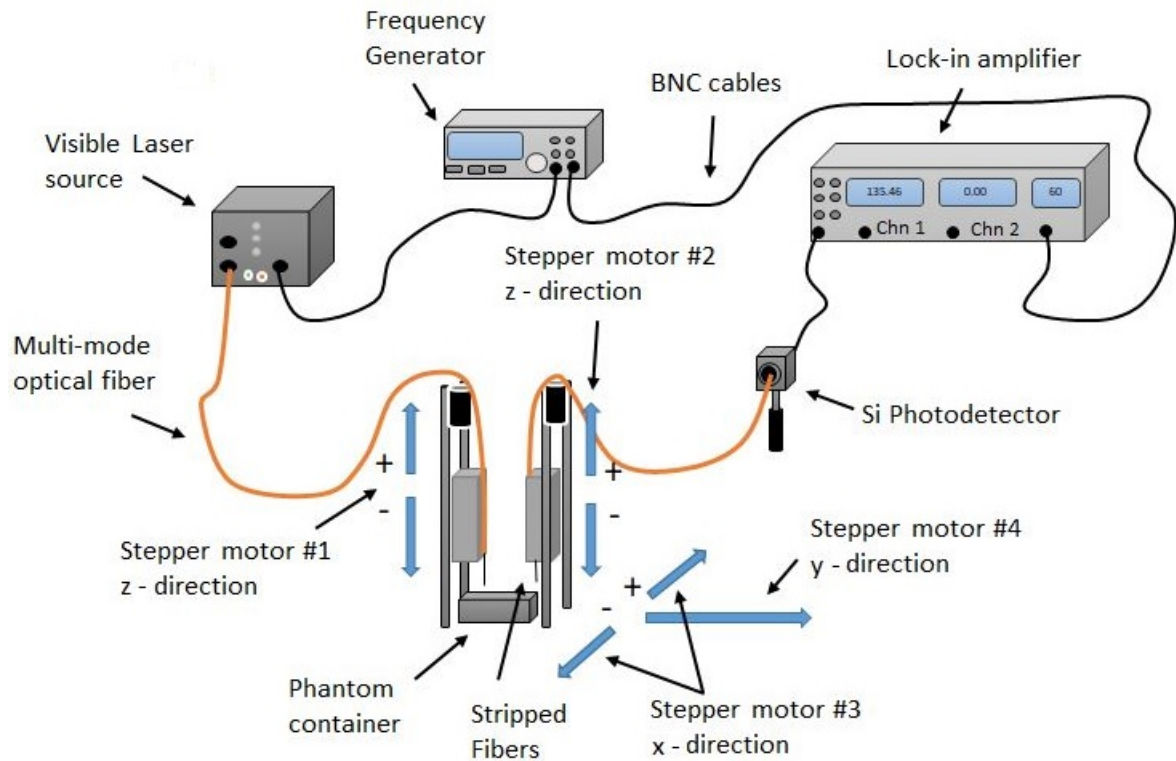


Figure 3.6: Schematic of the experimental set-up.

3.3 Map the intensity tomography of the solution

The aim of this part is to prove that the set-up designed can extract the information required to move onto further stages of the project. Therefore the two fibers were placed just inside the surface of the phantom and the collection fiber was moved in a sweeping system to map the exponential intensity decay in the phantom tomography relative to the source fiber (3.7). A sweep function written into the QTLab environment allows direct data file recording of the results from the lock-in amplifier measurements. Black china ink was then added to the solution to increase the absorption properties of the phantom and the resulting decay was measured. The ink was added at increments of 1ml, 2ml, 2.5ml, 3ml. It was chosen as it displays a relatively flat absorption profile for a broad wavelength spectrum as displayed in figure 3.2.

The source fiber was anchored in position and all movement were made with the collection fiber relative to the source. The x sweeps were incremented from small to larger distances to document the exponential decay with higher accuracy closer to the source fiber. x Sweeps were therefore taken at 0mm, 0.05mm, 0.2mm, 0.35mm, 0.5mm, 0.75mm, 1mm, 1.5mm, 2mm, 2.5mm, 3mm, 3.5mm, 4mm, 4.5mm for the phantom with no ink present. For the tests where ink was added to the solution, sweeps were measured up to 2.5mm, as distance recordings after were deemed unnecessary. A y sweep was also taken for each ink increment starting at the 0mm

position at the source fiber.

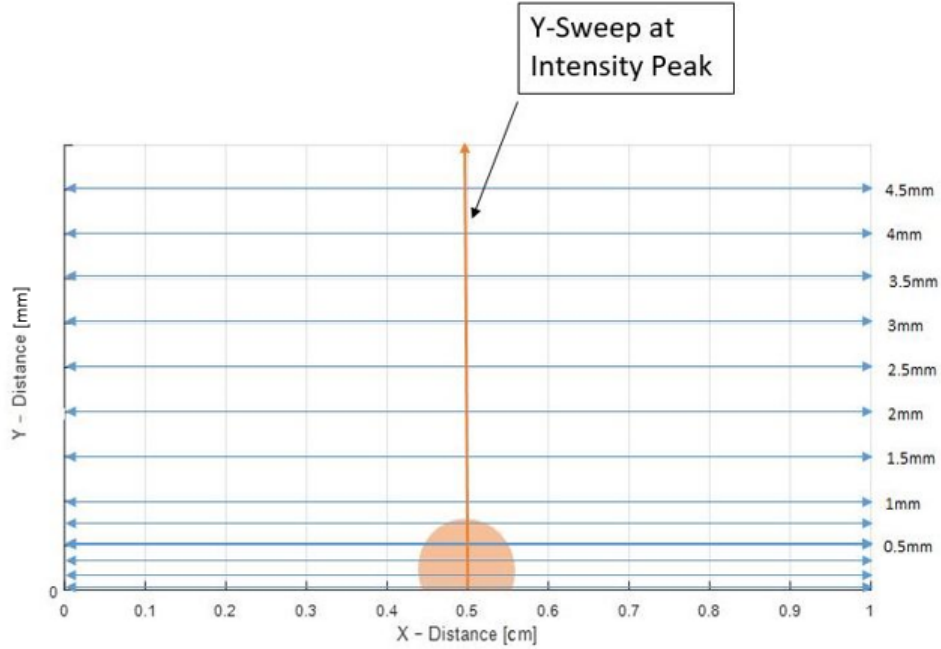
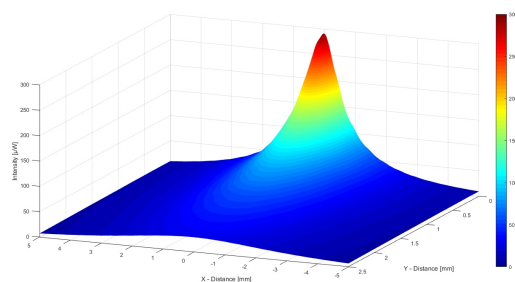


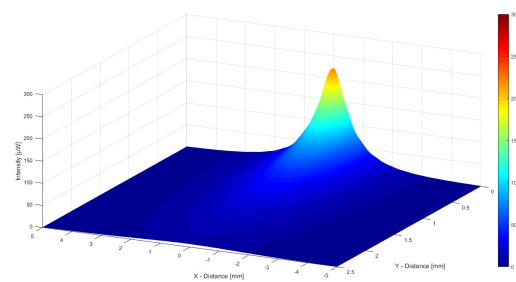
Figure 3.7: Schematic of x & y sweep of the phantoms tomography.

The decay results with ink increments were plotted via MATLAB and using extrapolation functions, 3-D images were created to visualize the intensity decay with distance. The results are plotted in figure 3.8, a 2-D top-down view in figure 3.9 and the logarithm of the intensity to further visualize any noise in the set-up in figure 3.10.

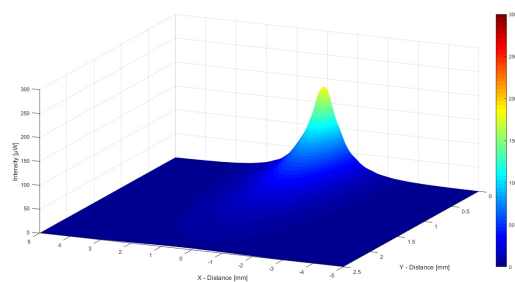
3.3.1 3-D plot: Exponential radial distance decay results



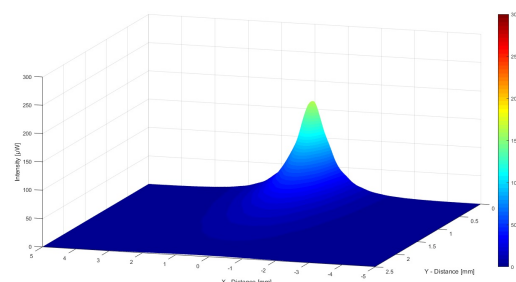
(a) No ink



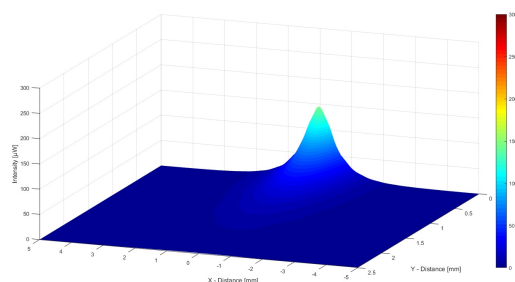
(b) 1ml of ink



(c) 2ml of ink



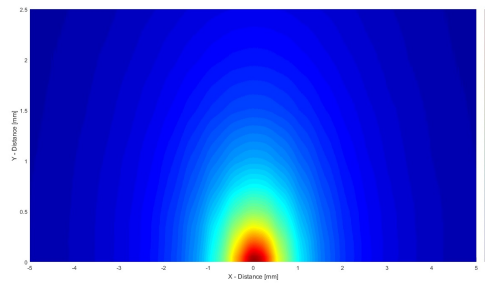
(d) 2.5ml of ink



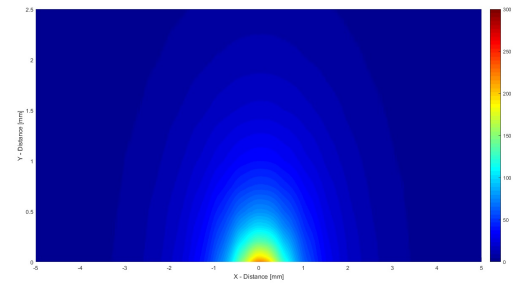
(e) 3ml of ink

Figure 3.8: 3-D intensity tomography profile of the exponential distance decay in the Lipofundin solution for (a) 0ml of ink (b) 1ml of ink (c) 2ml of ink (d) 2.5ml of ink & (e) 3ml of ink.

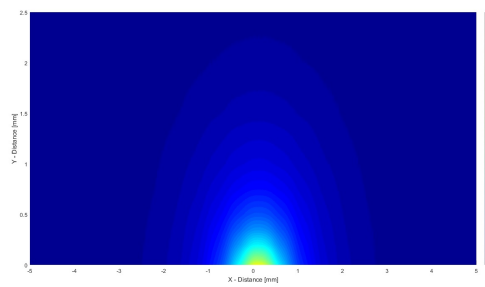
3.3.2 2-D plot: Top down view



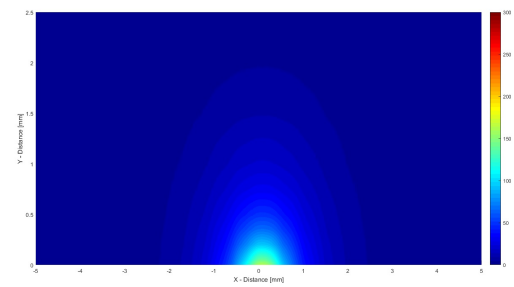
(a) No Ink



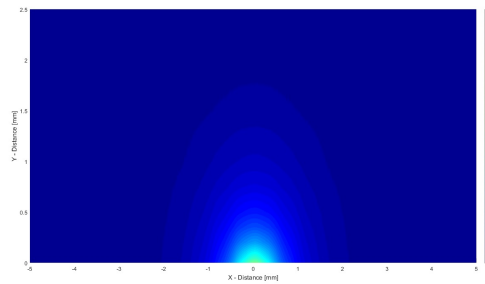
(b) 1ml of Ink



(c) 2ml of Ink



(d) 2.5ml of Ink



(e) 3ml of Ink

Figure 3.9: 2-D top down view of the tomography profile of the exponential distance decay in the Lipofundin solution for (a) 0ml of ink (b) 1ml of ink (c) 2ml of ink (d) 2.5ml of ink & (e) 3ml of ink.

3.3.3 3-D plot: Log scale of intensity

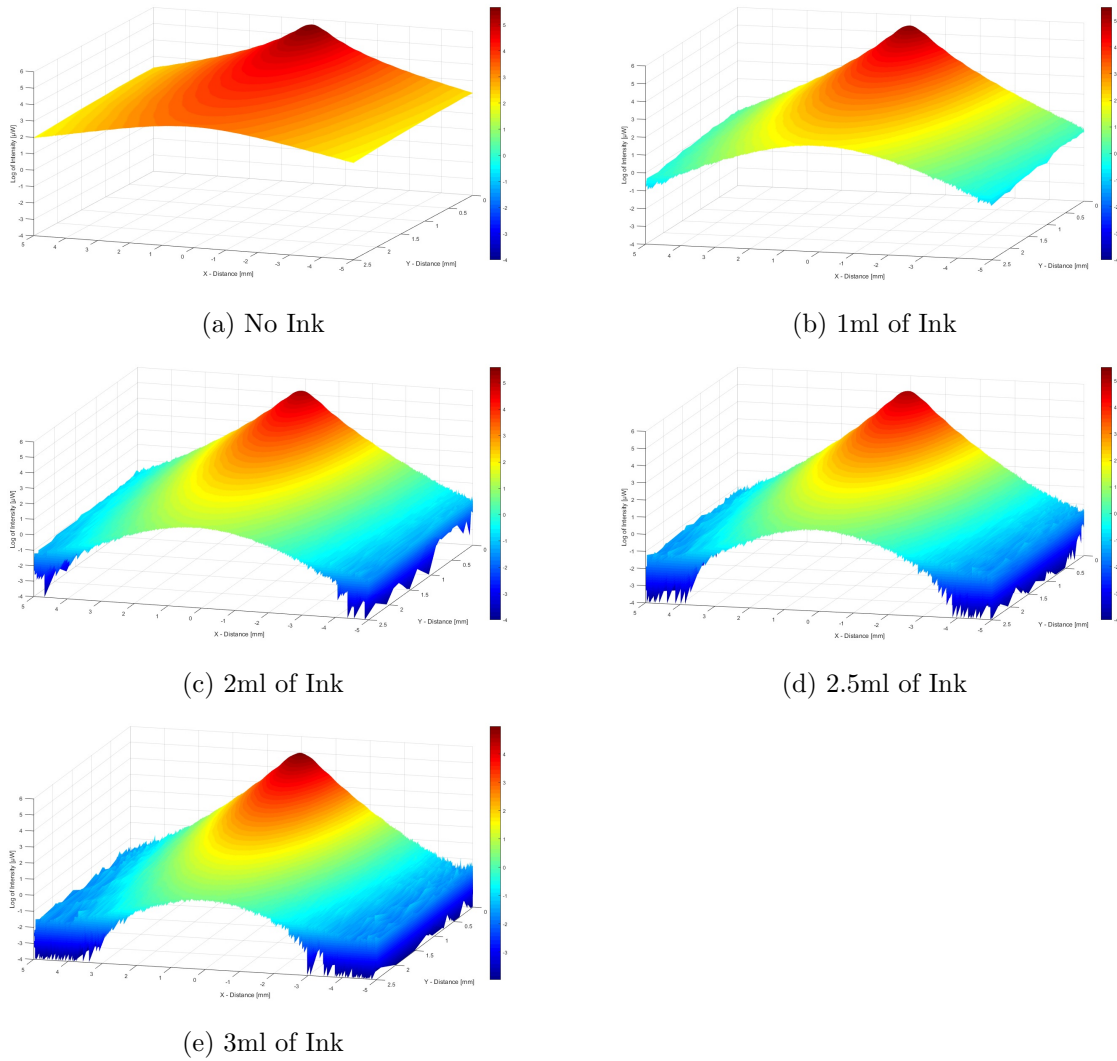


Figure 3.10: 3-D view of the logarithm of the intensity profile of the exponential distance decay in the Lipofundin solution for (a) 0ml of ink (b) 1ml of ink (c) 2ml of ink (d) 2.5ml of ink & (e) 3ml of ink.

Conclusion

There is a clear exponential intensity decay with distance separation of the fibers. Increasing μ_a by increasing black ink concentration has dampening effect on the intensity detection in both lateral x and y directions as well as the z axis. To learn more about the reproducibility of the set-up and whether concentration information can be extracted accurately the data must be analyzed further.

3.4 Exploring axial symmetry

To understand in more detail the accuracy and reproducibility of the stepper motor set-up, y sweeps and x sweeps are plotted against each other. Theoretically they should be the same. Any discrepancies that are consistent would provide some information that could lead to improvements.

In this section the data gathered from the x -sweeps both left and right are plotted against the data from the y -sweep (fig. 3.11). The results are plotted for each ink increment in figure 3.12.

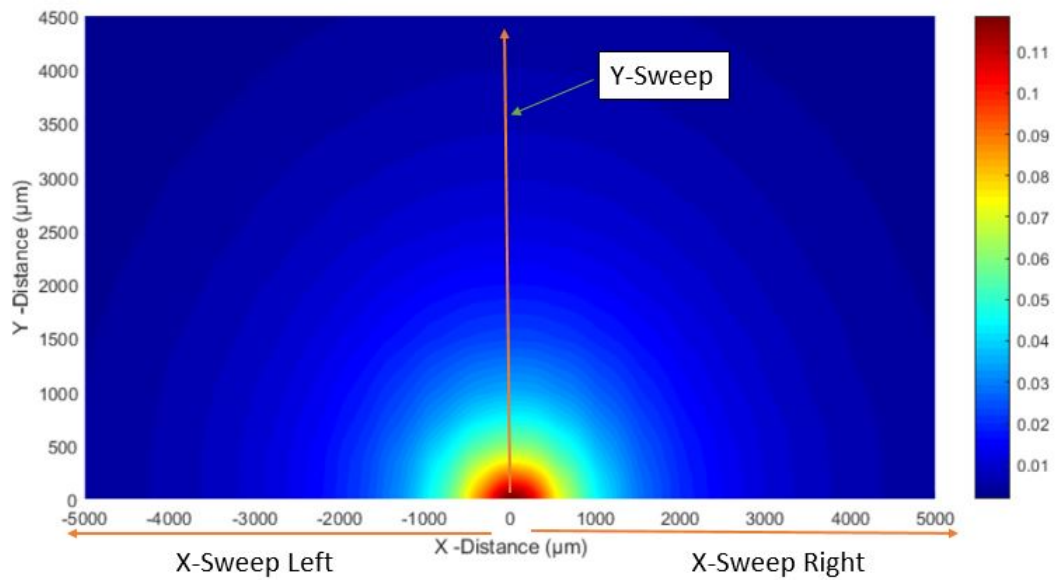
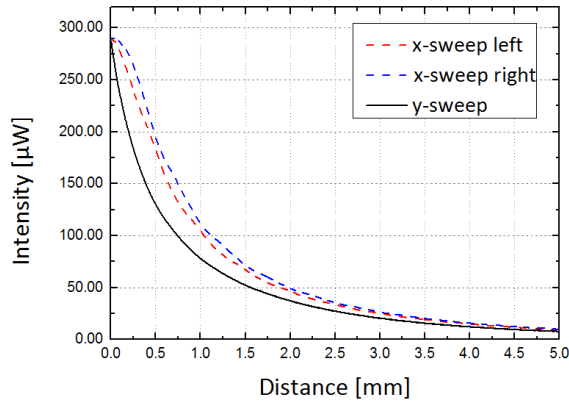
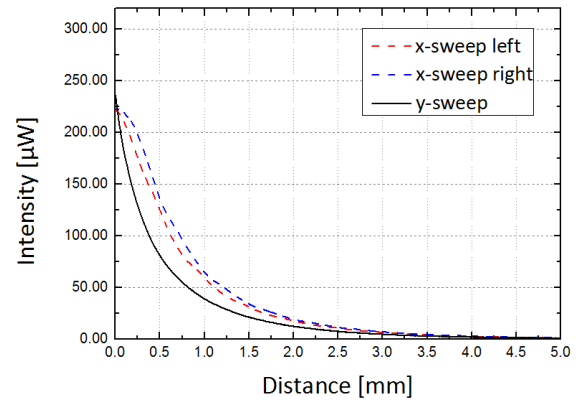


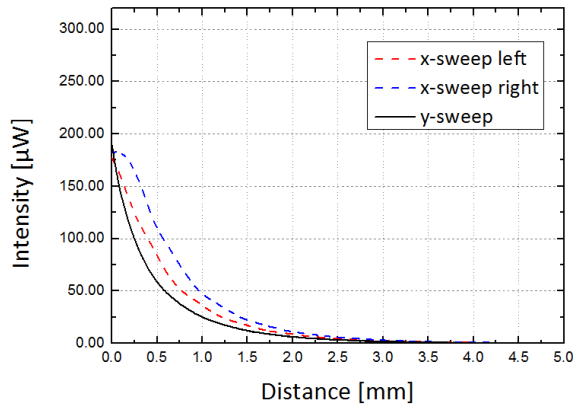
Figure 3.11: Tomography direction of x -sweeps & y -sweep.



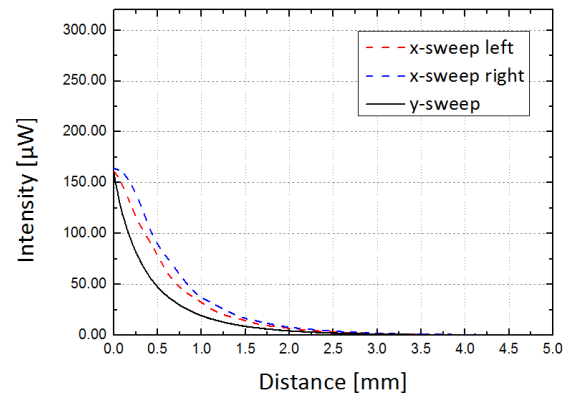
(a) No Ink



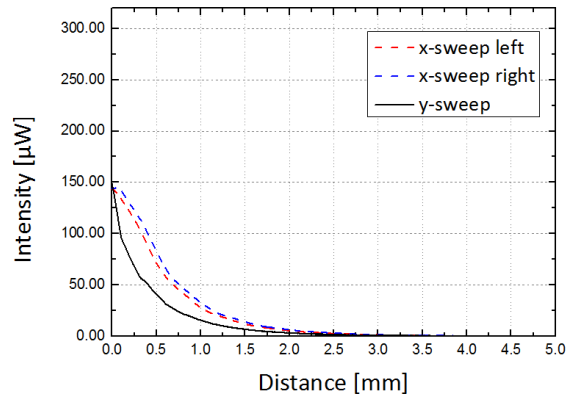
(b) 1ml of Ink



(c) 2ml of Ink



(d) 2.5ml of Ink



(e) 3ml of Ink

Figure 3.12: 2-D cross section in the x & y direction of the distance decay data for (a) 0ml of ink (b) 1ml of ink (c) 2ml of ink (d) 2.5ml of ink & (e) 3ml of ink.

3.4.1 Reproducibility of results

To ensure set-up built is operationally valid a final measurement was taken. Data points recorded at the 0.5cm mark of every x -sweep were taken and plotted (fig. 3.13). Values in-between were interpolated and a best fit curve was plotted against the original y -sweep. The results of which are displayed in figure 3.14.

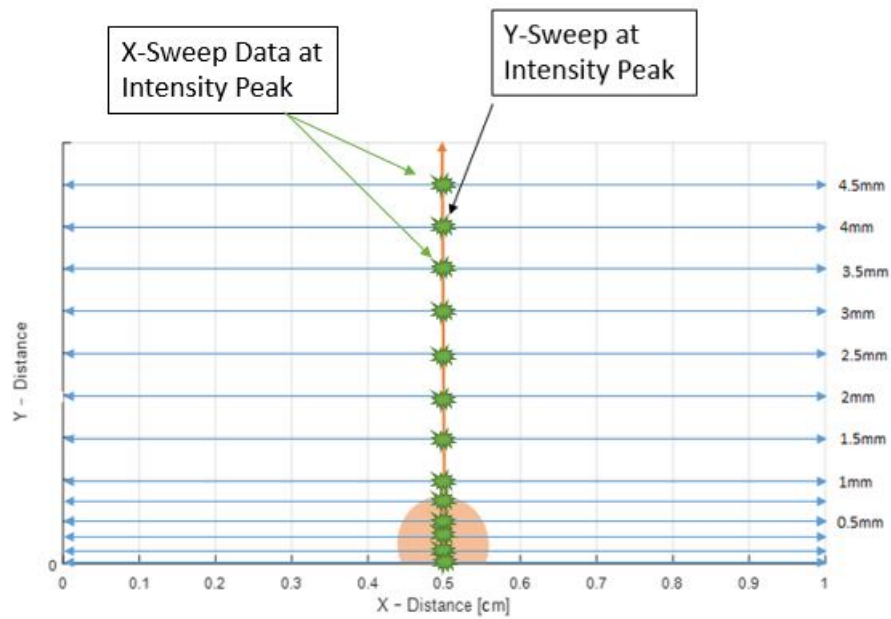
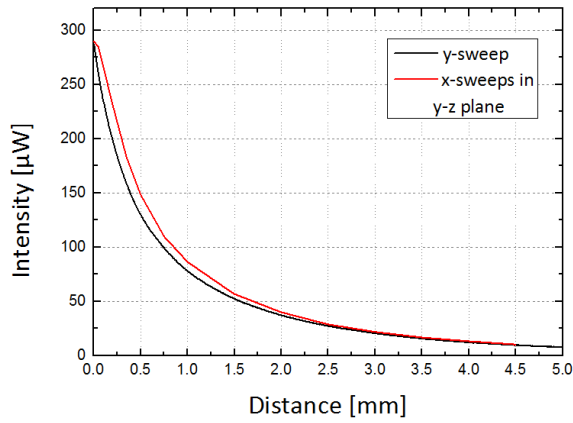
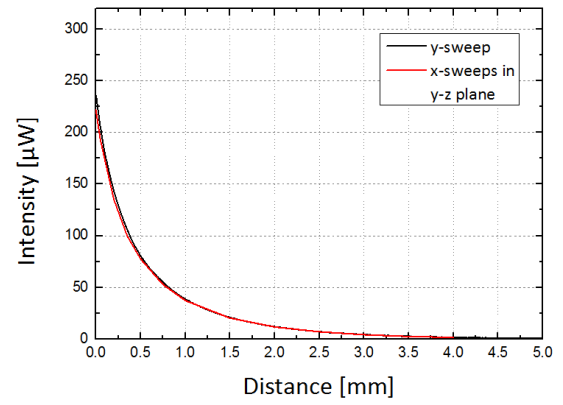


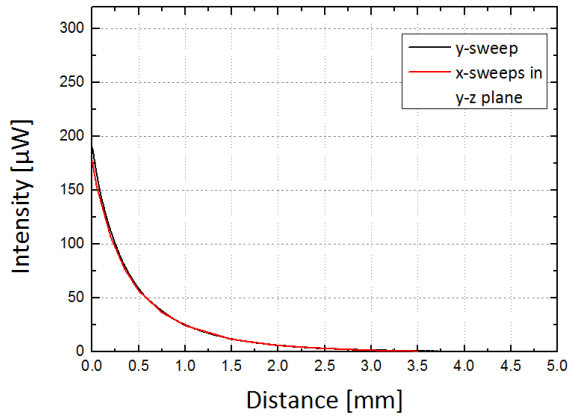
Figure 3.13: Tomography map of data points taken at 5mm of every x -sweep.



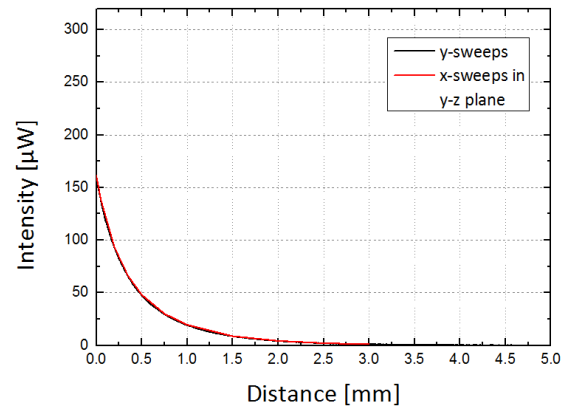
(a) No Ink



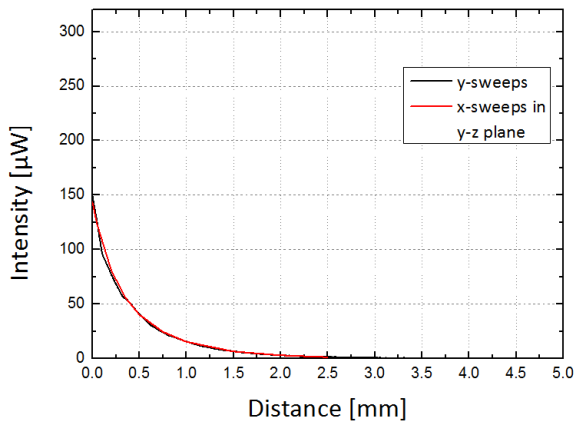
(b) 1ml of Ink



(c) 2ml of Ink



(d) 2.5ml of Ink



(e) 3ml of Ink

Figure 3.14: Reproducibility of results for same data recorded in both x & y -sweeps for (a) 0ml of ink (b) 1ml of ink (c) 2ml of ink (d) 2.5ml of ink & (e) 3ml of ink.

Conclusion

The results from figure 3.12 reveal that although the exponential decay is relatively consistent for x -sweep left and right, a discrepancy exists with y -sweep. However plotting the data for when both the y and x -sweep overlap (fig.3.14) is very consistent. Therefore the issue is not with the stepper motor moving in the x vs y -axis.

A possible reason is the geometry of the needle holding the fiber. It has an angled metallic opening which can be observed in figure 3.4. Both fibers were placed in the needle in such an arrangement that both opening sides of the needles are facing each other. This needle geometry would stay constant during the y -sweep and every x -sweep where it crosses the y -sweeps path. However, during x -sweeps left and right there is different geometry relative to the fixed source fiber. The schematic of which is shown in figure 3.15. This could affect collection of the intensity. In the next steps of the project only y -sweeps will be explored. Care will be afforded to larger exposure lengths of the stripped fiber from the needle holder. The thought process is by keeping the metallic tip relatively far from the coupling zone, the cleaved fiber end will be unaffected in the medium.

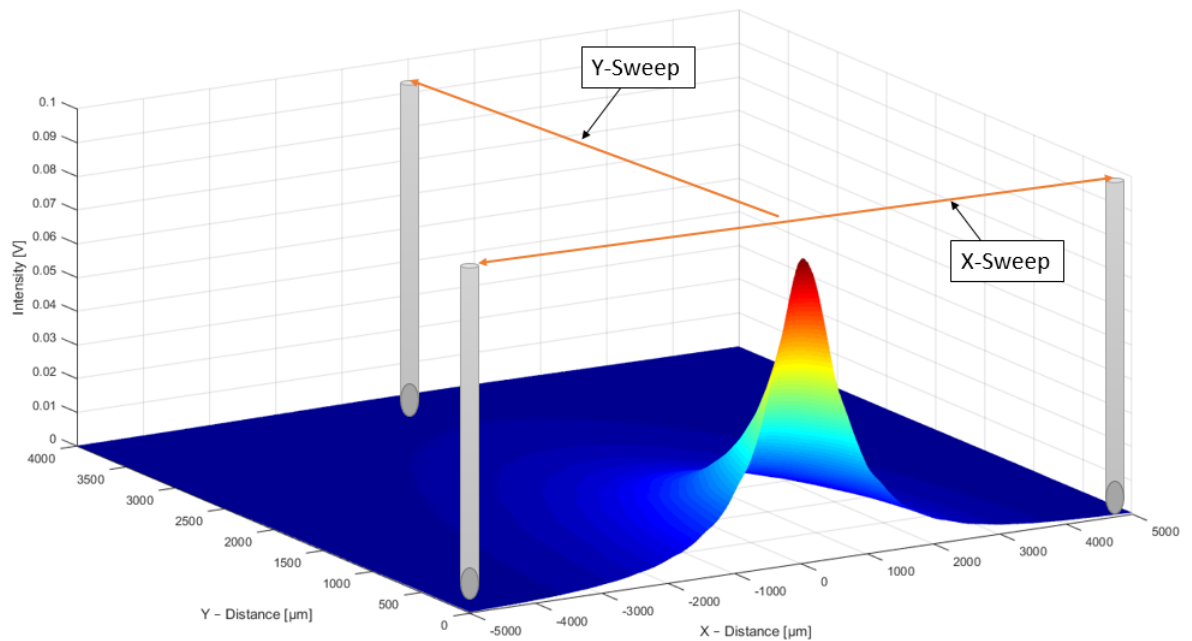


Figure 3.15: Schematic of possible discrepancy issue between x and y sweeps.

3.5 Extract μ_a concentration from intensity and radial distance

The final step on this section of the project is to prove a relationship between the exponential intensity decay at certain distances and ink concentration. The same process of adding ink increments into the lipofundin and water phantom was repeated but with smaller increments of ink to retrieve more data points to plot. The ink was incremented at $0.2ml$ steps at fiber separation distances of $0mm$, $0.2mm$, $0.5mm$, $0.75mm$, $1mm$, and $1.5mm$.

The results are displayed in figure 3.16. It can now be measured quantitatively how ink concentration affects the decay. The decreasing slopes of the linear fit for each distance is acknowledged in table 3.1.

Radial distance	Gradient
$0mm$	0.0147
$0.2mm$	0.0134
$0.5mm$	0.0104
$0.75mm$	0.0089
$1.0mm$	0.0073
$1.5mm$	0.0052

Table 3.1: Gradient values of intensity vs ink concentration.

From the linear equation $f(x) = ax + b$ a simple relationship can correlate the concentration from the intensity value found at a given distance. Where x is the concentration of ink, a is the gradient found at a given radial distance, $f(x)$ is the intensity and b an intercept constant. Therefore the equation to find concentration would be:

$$x = \frac{f(x) - b}{a} \quad (3.4)$$

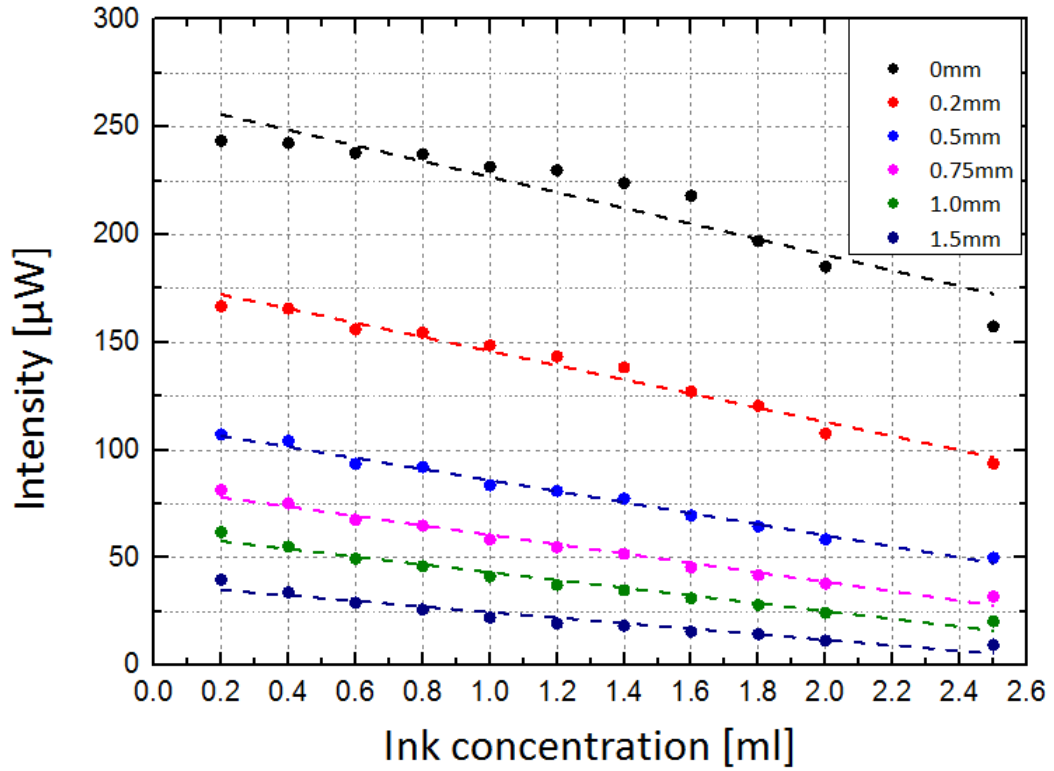


Figure 3.16: Intensity vs for ink concentrations for six set distances.

Conclusion

A clear linear relationship exists between radial intensity decay and concentrations of the absorbing chromophore, in this case ink. As mentioned in chapter two there is not much literature that covers distance decay on a *millimeter* scale. The fact that there is a clear linear relationship is proof required to move to the next section of this research project. The ability to extract the concentration information from the radial decay is the first steps towards spectroscopy. The conversion efficiency of light at $25mW$ entering the optical phantom and what is collected via diffuse reflection spectroscopy is $\approx -21dB$ for the $685nm$ source.

A simple model constructed for both *Mie* and *Flock* approximations of photon scattering for just the lipofundin and water solution predicted an ideal fiber separation distance of $\approx 2.15mm$ (*Mie*) and $\approx 7.52mm$ (*Flock*) to collect the signal. It can now be understood from experimental results that this experimental set-up follows *Van Staveren et al* & the *Mie* approximation relatively well. Whether it is accurate to extrapolate this model into an unknown territory of longer, $1.59\mu m$ and $2.1\mu m$, wavelengths it is unclear. If the extrapolation of the model is accurate, the $1.59\mu m$ peak of glucose in the first overtone band will be difficult to retrieve via diffuse reflection photon propagation and the $2.1\mu m$ glucose peak in the combination band should not be detectable by the collection fiber. In other words, Lipofundin MCT-20, as a scattering turbid environment, is

potentially on the fringe of acting as a competent medium for diffuse reflection spectroscopy for the $1.59\mu m$ peak if at all for the $2.1\mu m$ peak.

It should be noted at distances very close to the source fiber there seems to be a slight discrepancy with the linear fit. Potentially this might indicate that at very close distances between the source and collection fiber this relationship becomes inaccurate. However, errors can scale with intensity and slight discrepancy could be also apparent at lower intensities but difficult to measure due to the detection resolution.

It should also be noted that the gradient extraction model breaks down as presented in chapter two, section 2.4.2. *Fantini et al.* described how the gradient of the plot $\ln(I(\rho) * \rho^2)$ vs ρ is $-\mu_{eff}$. μ_{eff} is nothing more then $\sqrt{3\mu'_s\mu_a}$ in which the concentration can consequently be extracted. They describe the model as most accurate between the range of $1.5 - 2cm$. However figure 3.17 shows no linear relationship between the natural log of $I(\rho) * \rho^2$ and distance in the *millimeter* scale. To conclude, the gradient extraction model is not accurate for diffuse reflection spectroscopy with fiber separation distances under $5mm$.

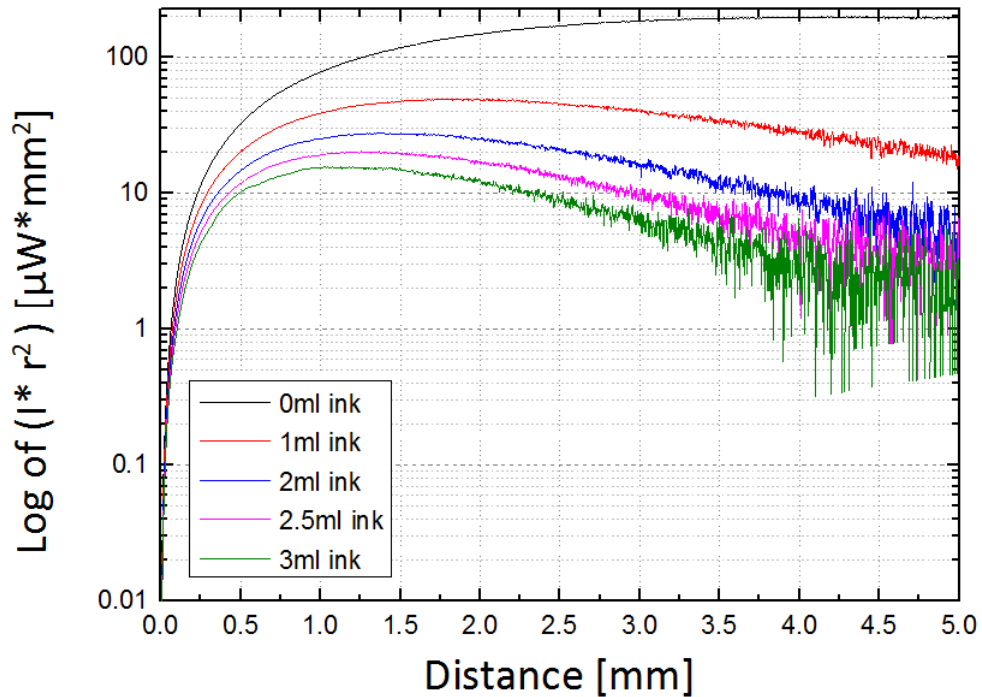


Figure 3.17: Distance decay model $\log(I * \rho^2)$ vs ρ .

Chapter 4

Integrating a broadband NIR source and complimentary NIR detector

4.1 Introduction

The goal of this section of the project is to expand on the current experimental set-up. To investigate the first overtone band as well as the combination band of glucose a broadband source is required. Ink increments will be used again to mimic the absorption coefficient (μ_a) of glucose. The aim is to build a secure system that is accurately able to detect glucose increments to move onto the next stage of the project.

4.2 Experimental set-up design

The source

A broadband source is required that covers the NIR regions of interest ie. $1.5 - 2.4\mu m$. The optical source chosen was an NKT EXR-20 [26]. It is a supercontinuum source, therefore the broadband output is formed from a collection of non-linear processes that act upon an individual pump beam. The combination of a broadband output that is high in intensity renders this technology highly suitable for spectroscopy measurements.

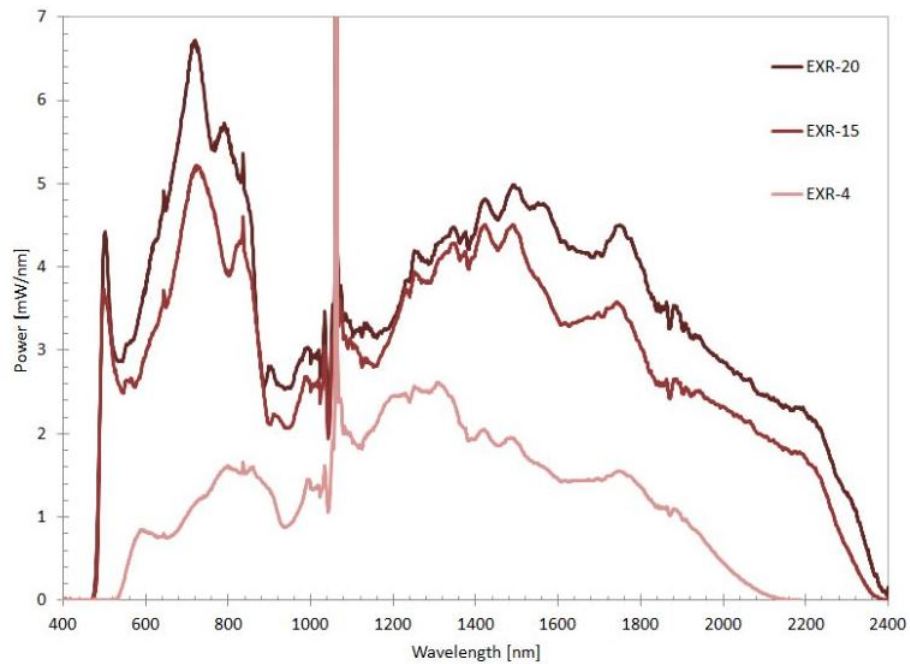


Figure 4.1: NKT EXR-20 output power spectrum [26]

At the heart of the supercontinuum process is a *photonic crystal fiber* (PCF). This is a fiber design that has a higher refractive index core surround by a lower index cladding like conventional optical fibers. However, unlike the conventional fiber designed to induce total internal reflection, a photonic crystal is a matrix of high and lower index dielectric materials. This is created in the cladding material of figure 4.2. This matrix can take designs found in crystals, thus the name. In this example, a hexagonal design of periodic distributed air filled holes is present in the cladding layer, running the length of the fiber, encasing a silica core creating an air-silica hybrid.

Three main factors dictate the output of the supercontinuum process:

- The dispersion of the fiber relative to the pumping wavelengths and also the sign of the dispersion induced i.e. anomalous vs normal dispersion.
- The pulse length
- The peak power

The advantage of PCF's is they can be designed to engineer specific dispersion properties, they can therefore introduce high non-linearity and enhance the broadband effect. Unlike the conventional silica glass fibers where the zero-dispersion wavelength is anchored to $1.3\mu m$, PCF's have a customizable zero-dispersion wavelength. This engineering leads to higher field-confinement and localization to induce greater light-matter interactions allowing better control of the phase velocity of the field to induce phase matching. Pulsing the source for short lengths of time, such as femtoseconds, interacts with the varying refractive indices to produce a phase shift and induce a change in the frequency spectrum. The dominant non linear processes responsible for

the broadband supercontinuum are *self-phase modulation* and *four-wave mixing*.

In the design (fig. 4.2) used in NKT products the PCF structure and thus the supercontinuum output is determined by the hole size (d) and the hole pitch or gap between the holes (Λ). By choosing a sufficiently small hole-size one can design a fiber with no second-order mode cut-off and therefore single-mode for every wavelength. This a main feature of the NKT EXR-20 source [31].

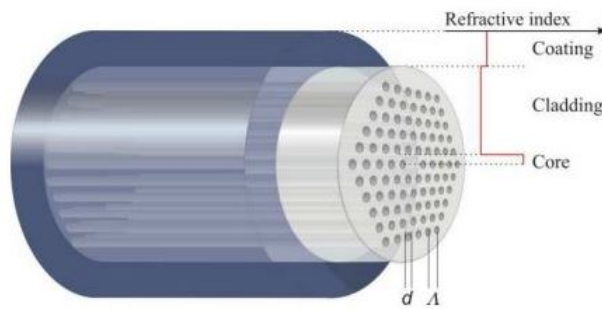


Figure 4.2: Schematic of a PCF fiber used in NKT products. Light is guided by a high index embedded solid core surround by a low index cladding housing a hexagon lattice of air holes. A polymer outer coat offers protection. [31]

SuperK Optical Specifications	
Repetition rate	78MHz
Total visible power stability	$< \pm 0.5\%$
Polarization	Unpolarized
Beam Output	Gaussian, single mode
M^2	< 1.1
Output options	collimated
length of output fiber	1.5m
Beam diameter	$\approx 1mm$ at 530nm $\approx 2mm$ at 1100nm $\approx 3mm$ at 2000nm
Beam divergence (half angle)	$< 5mrad$
Beam pointing accuracy	$< 1mrad$
Beam pointing stability	$< 50\mu rad$
Typical single mode coupling efficiency	$< 70\%$

Table 4.1: SuperK EXR-20 optical specifications from NKT datasheet. [26]

Alignment mirrors

An earlier design of the experimental set-up employed free-space mirrors for aligning the beam for collimation. However it was found after early initial testing that the conversion efficiency could be drastically improved by using a component built by NKT photonics. The NKT SuperK EXR-20 has a large collimation piece at the end of its output fiber. It is not compatible to attach via an adapter to a regular fc fiber end as with single wavelength laser.

The new component is a SuperK CONNECT. It allows direct locked attachment of the unique fiber collimator output of the source and easy alignment via adjustment screws (fig.4.3). This encased alignment section was securely fastened to the optical bench so this component is completely mechanically stable. It was untouched for the duration of the project except for alignment adjustments of the screws (fig. 4.5) [31].



Figure 4.3: NKT SuperK EXR-20 collimator fiber end and corresponding SuperK CONNECT alignment case [31].

The collimator

The collimator was selected to ensure maximum coupling of the NIR region of interest from the broadband SuperK source. The model chosen was Thorlabs PAF-X-18-PC-D. Coupling a source as broad as the SuperK is extremely difficult. Individual alignment over specific target ranges is required, however there are some important characteristics to consider when choosing the collimator. These are addressed in the characterization section [32].

Filters

Early attempts to extract the information from the $1.59\mu\text{m}$ wavelength region of interest while using the full SuperK spectrum proved futile as the extended InGaAs detector experienced sat-

uration. Therefore filters were adopted to ensure only the region belonging to the first overtone band and the combination band of glucose would be explored. Thorlabs FEL-1500 and FEL-1400 are longpass filters blocking all the wavelengths below $1.5\mu\text{m}$ and $1.4\mu\text{m}$ respectively [33]. To ensure minimum saturation when attempting to detect the $2.1\mu\text{m}$ peak in the combination band a Thorlabs FB2250-500 bandpass filter was used. It allows light with between $2 - 2.5\mu\text{m}$ to pass with a central wavelength transmission at $2.25\mu\text{m}$ [34]. All three filters were used at different stages of measuring.

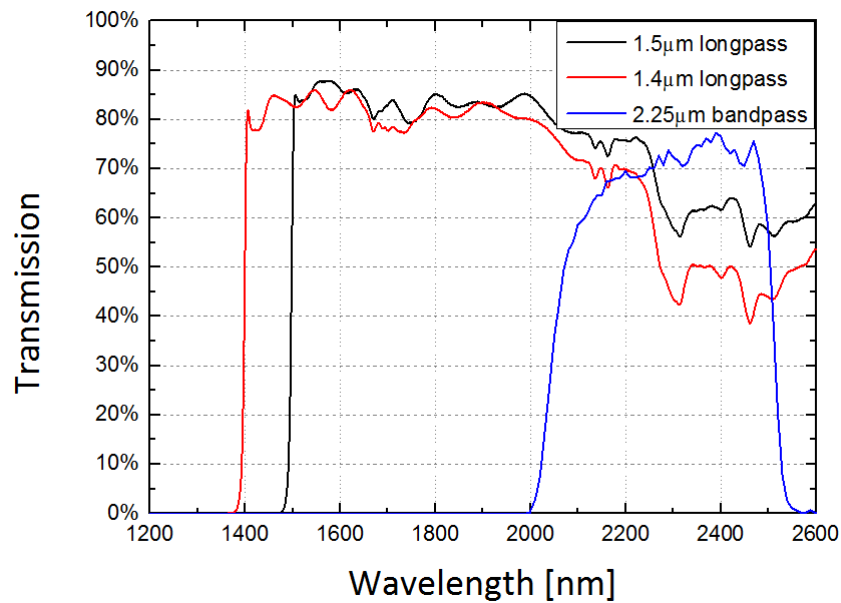


Figure 4.4: Transmission profiles of the each filter, data plotted from Thorlabs specification sheets [33], [34].

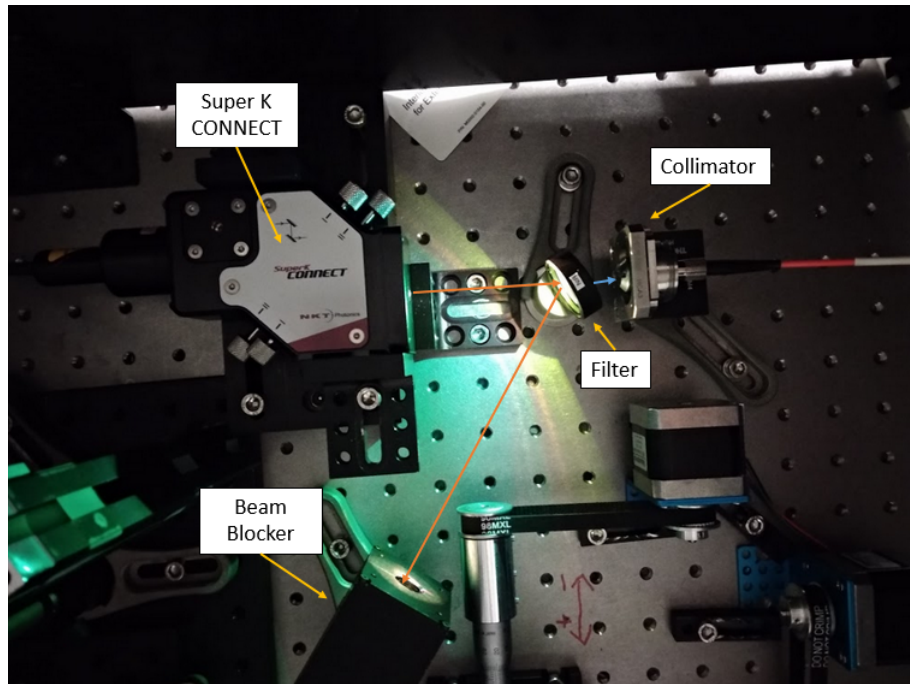


Figure 4.5: Filter and collimation component of experimental set-up.

The spectrometer

As described in chapter two, a spectrometer is needed to study the spectrum collected from the sample. The TWINS set-up as detailed in chapter two, section 2.1.1 is added to the optical bench as shown in figure 4.7. It creates a free space element in the set-up that does introduce some losses. These will be characterized in the next section. The elements in the TWINS set up were aligned and tested then left untouched for the duration of the project. The only elements that are routinely altered in this section are the chopper, the fiber collimator and the detector.

The detector

The commercial detector chosen to investigate both the first overtone and combination band is a New England thermo electrically cooled extended InGaAs photodiode [35]. It has a spectral range from $1.2\mu m$ to $2.6\mu m$ as shown by its response curve in figure 4.6. Experimentation proved it was sensitive to wavelengths far into the visible. It could detect the $685nm$ source for example.

The sensitivity of the device is very important as the collected signal could be very small. A few parameters characterize the overall sensitivity of the detector. The noise floor is relatively low with an NEP of $3 \times 10^{-13} W/\sqrt{Hz}$. This is the minimum power required to have a SNR of 1 or a signal that equates the noise floor. The noise that does affect this device is Johnson and shot noise and therefore has a flat noise floor over all frequencies. Knowing the device saturates

at 10V an SNR of 90dB can be calculated. The specific detectivity of the device is comparative figure of merit to other devices. It can be calculated via:

$$D^* = \frac{Af_B}{NEP} = \frac{R\sqrt{A}}{S_n} \quad (4.1)$$

Where A is the area of the photosensitive region, f_B is the noise bandwidth, R is the responsivity and S_n is the noise spectral density of the detector. This photodiode has an active area diameter of $1000\mu m$ and D^* can be calculated as $2 \times 10^{11} \sqrt{cm} Hz/W$ this unit is also expressed in *Jones* [35].

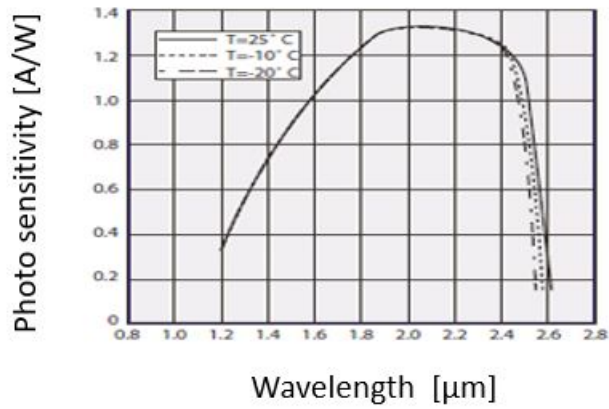


Figure 4.6: Responsivity curve for the New England ext. InGaAs photodiode [35].

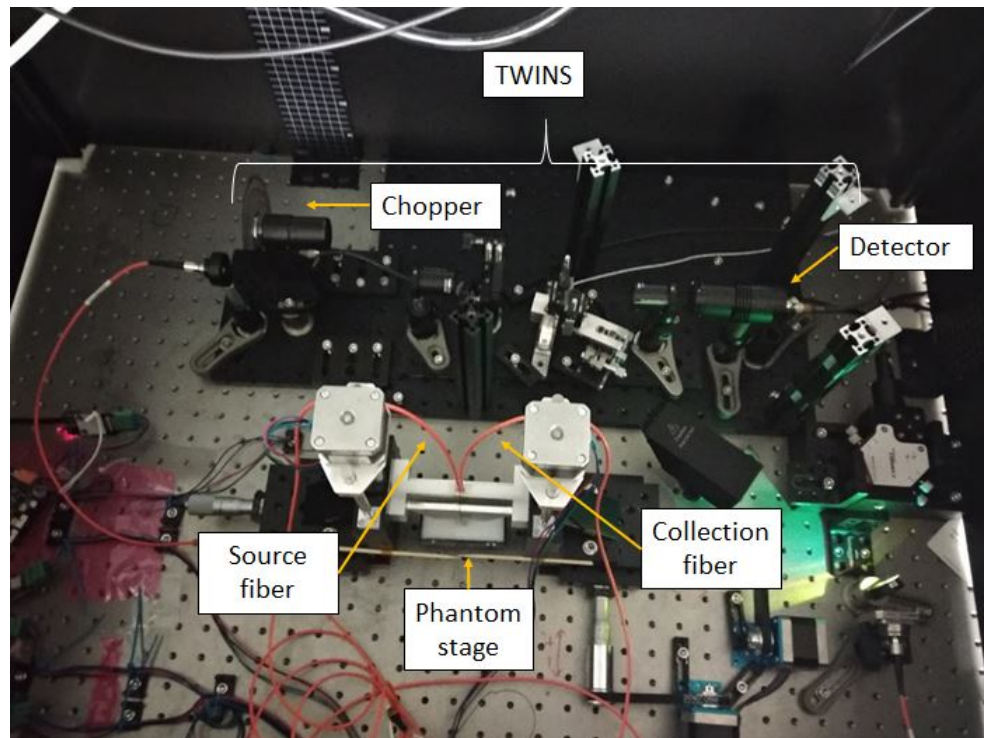


Figure 4.7: Image of full experimental set-up with new components added.

4.3 Characterization of set-up components

Maximum power conversion efficiency at each step is very important. Therefore, each variable in the set-up must be characterized and troubleshooted.

The broadband optical source

A test was designed to observe any fluctuations or strange behaviours in the optical source that would disagree with the data sheet in fig. 4.1. The SuperK EXR-20 has a simple power control from 12% to 100%. To learn more about which power setting to record optimal measurements, a test was designed as follows:

The SuperK was connected directly from the free space collimation component into the TWINS element to retrieve the spectrums (fig 4.8). The extended InGaAs photodetector has a sensitivity of 10V. The SuperK, after the $1.5\mu m$ longpass filter, has a power of 50 – 100mW (calculated in section 4.3). Therefore to avoid damaging the detector, neutral density filters were used to absorb the majority of the transmission.

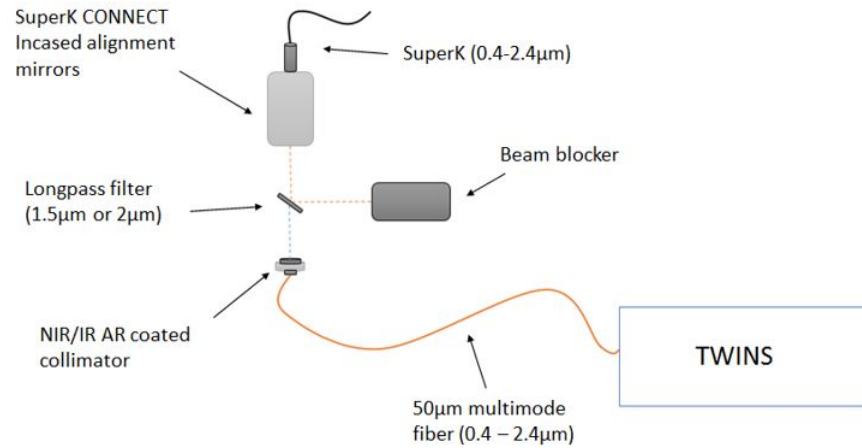


Figure 4.8: Schematic of set-up design to test the SuperK EXR-20. output.

The neutral density filters chosen were Thorlabs NE50A, NE40A and NE20A. The transmission spectrums were plotted for the wavelength range of interest from data files provided from Thorlabs (fig 4.9) [37]. The physics behind the attenuation of these filters is absorption, therefore caution was taken when dealing with the high power NIR source directly. The three filters were connected in succession with the highest transmission profile filter (NE20A) first and the lowest (NE50A) last. The spectrum of the SuperK was corrected via the neutral density filter data in figure 4.9. The real SuperK spectrum is plotted in figure 4.10.

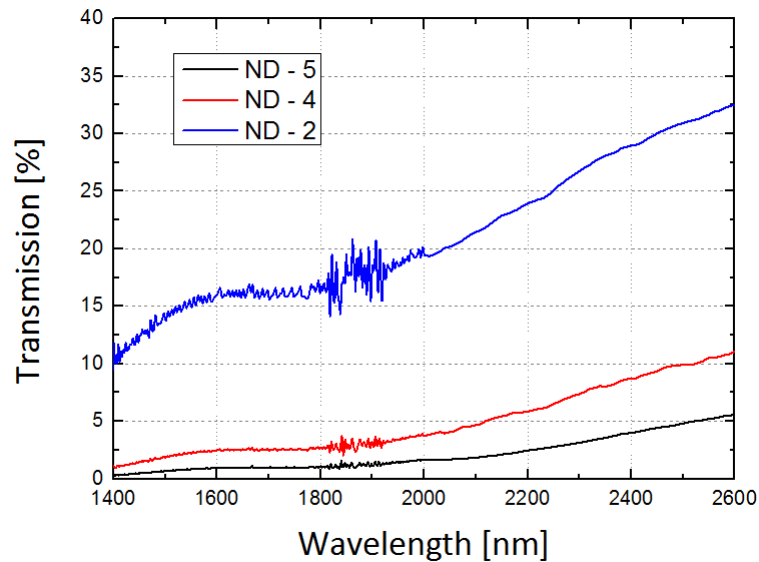


Figure 4.9: Transmission spectrum of the neutral density filters, data plotted from Thorlabs specification sheets [37]

The stability of the source at different wavelengths was an uncertainty so a simple test was

devised to measure it. Five different power levels were measured four times. The mean was plotted and the standard deviation is visually displayed in pink in figure 4.10. The results show that while there are fluctuations present in the lower wavelengths of the first octave band, they are relatively minimal.

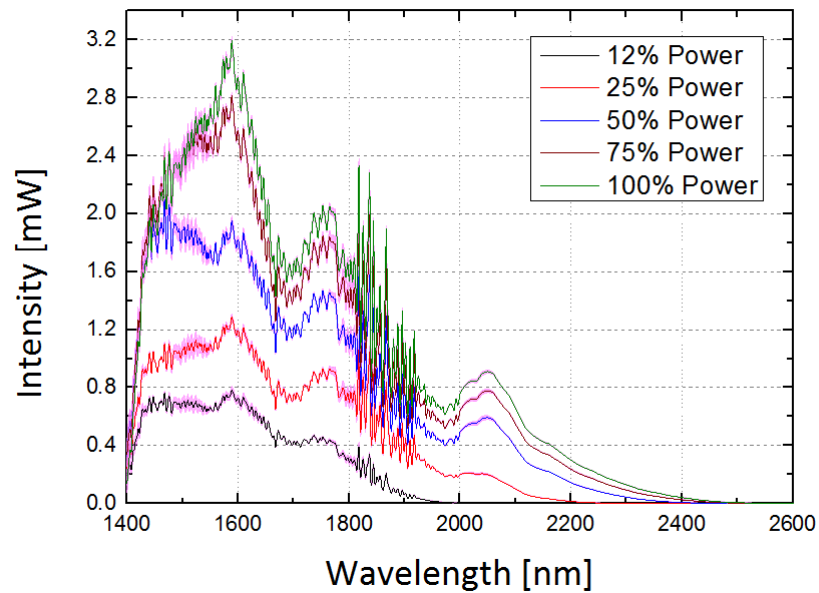


Figure 4.10: NKT SuperK EXR-20 spectrum bandwidth for power increments.

The collimator

Mode-field diameter:

Defined as the optical power per unit area across the end face of a single mode fiber [4.11]. where P is the power, d is the diameter of the fiber core, D is the diameter of the core and cladding and V is the normalized frequency. For a V -number ranging from 0-2.405 only the fundamental mode, LP_{01} , can propagate. A V -number of 3.8 represents the cut-off for three modes LP_{01} , LP_{11} and LP_{21} . The mode-field diameter is $13\mu m$ according to the datasheet. Therefore coupling into a fiber core of $50\mu m$ is theoretically agreeable [32].

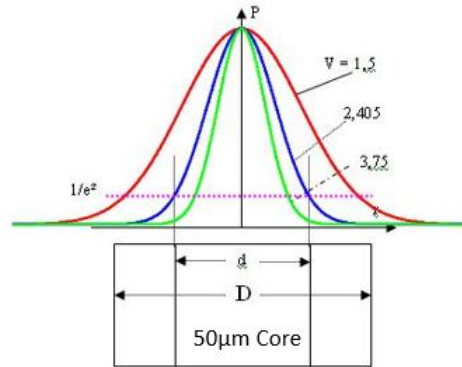


Figure 4.11: Schematic of the mode-field diameter measurement with a fiber core for different modes.

Maximum waist distance:

Defined as the maximum distance from a lens a Gaussian beams waist can be placed. It is calculated as follows:

$$z_{max} = f + \frac{2f^2\lambda}{\pi[MFD]^2} \quad (4.2)$$

Where the f is the focal length of the lens, λ the wavelength of light incident and MFD the mode-field diameter. The focal length of the aspheric lens in the collimator is $18.44mm$. Choosing a wavelength of interest such as $1.59\mu m$ obtains a z_{max} of $\approx 2m$. Figure 4.12 displays a schematic of the collimation.

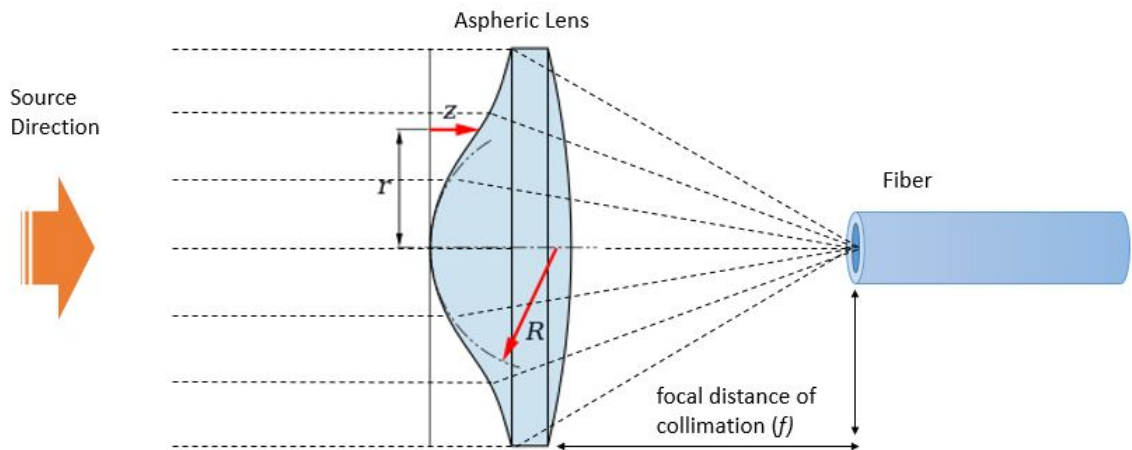


Figure 4.12: Schematic of the mode-field diameter measurement with a fiber core for different modes

Beam divergence angle:

$$\theta = \left(\frac{MFD}{f} \right) \left(\frac{180}{\pi} \right) = 0.707 \text{ mrad} \quad (4.3)$$

Input beam diameter approximation:

$$d = 4\lambda \left(\frac{f}{\pi MFD} \right) \quad (4.4)$$

Using equation 4.4 the input beam diameter of the collimator can be calculated for the same wavelengths displayed for the Superk beam diameter in table 4.1. The collimator lens also has a clear aperture of 5.5mm . Therefore it is clear all of the wavelengths of the SuperK can be collected.

Source diameter	Collimator diameter
1mm at 530nm	0.96mm at 530nm
2mm at 1100nm	1.99mm at 1100nm
3mm at 2000nm	3.6mm at 2000nm

Table 4.2: Collimator wavelength dependent diameter vs source wavelength dependent

Lens material

The collimator lens is made from ECO-550 glass. It has a transmission profile of 100% from $0.4 - 2.4\mu\text{m}$, covering the range of the SuperK. The numerical aperture of the lens is 0.15 which is less than the numerical aperture of the fiber at 0.22. This relationship ensures maximum coupling into the fiber. The lens has an AR-coating in the range from $1800 - 2400\text{nm}$ covering the combination band of glucose [25], [32].

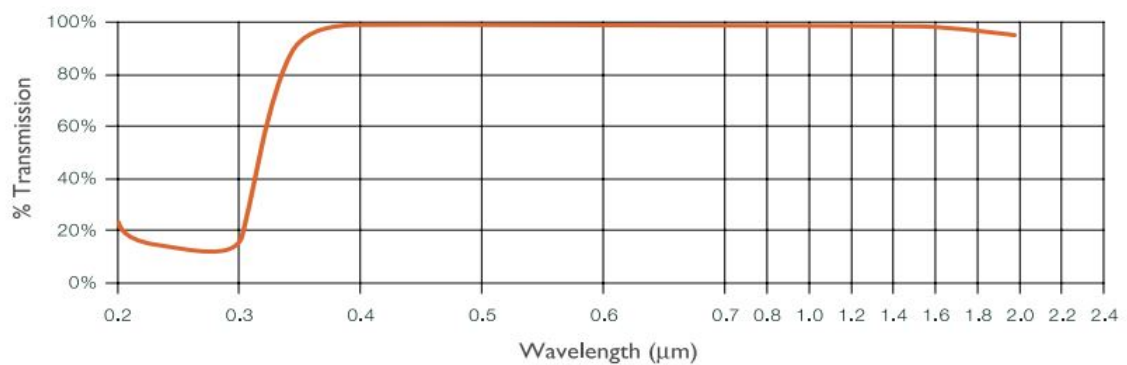


Figure 4.13: Transmission profile of ECO-550 glass [28].

The Fibers

Since sustainable power conversion efficiencies is the most important feature at every stage of the experimental set-up, emphasis was placed upon testing the source and collection fibers. Both fibers were stripped, cleaved and cleaned with *Isopropyl alcohol*. They were examined via a handheld fiber microscope the images of which can be observed in figures 4.14 and 4.15.

Figures 4.14 (a) and 4.15 (a) display the image of the regular uncleaved end of both the source and collection fiber. Figures 4.14 (b) and 4.15 (b) exhibit the cleaved ends of both the source and collection fiber. Obtaining focused images of the stripped and cleaved ends is extremely difficult. A handheld microscope has an attachment port for a screwing a regular fiber end in perfect focus. This is not compatible for a stripped and cleaved fiber end. A makeshift set-up was designed to manually locate this position with great care to not damage the exposed fiber end.

Slight damage can be seen on the collection fiber regular non-cleaved end near the core in addition to an uneven cleaved cut on the cleaved end (fig. 4.15 (b)). Quick power measurements were taken to compare the performance of the two. Both fibers were tested and fixed in the set-up. The visible laser was used for calibration and the output power was recorded beneath both fibers by a powermeter. The visible source was then switched from one fiber to the next. The illuminating power capabilities of both stripped and cleaved ends were constant. Second the collection characteristics of both were tested with a visible laser in a Lipofundin/water scattering phantom at $0.05mm$ separation distance. This measurement was a constant value, determining it was safe to move forward with experiments.

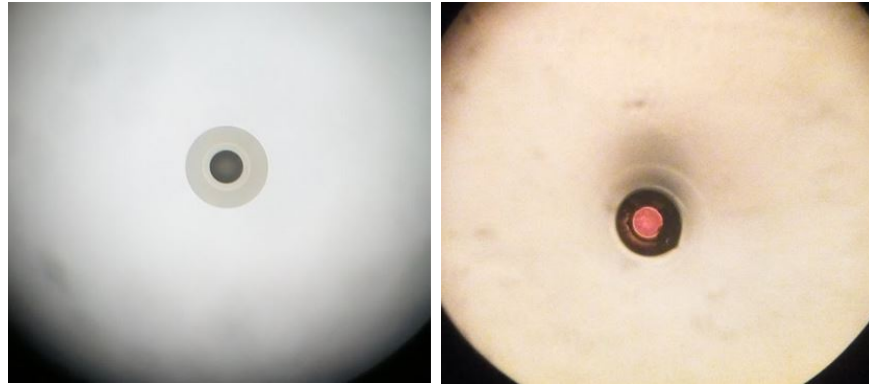


Figure 4.14: The source fiber (a) normal commercial end & (b) the stripped and cleaved end.

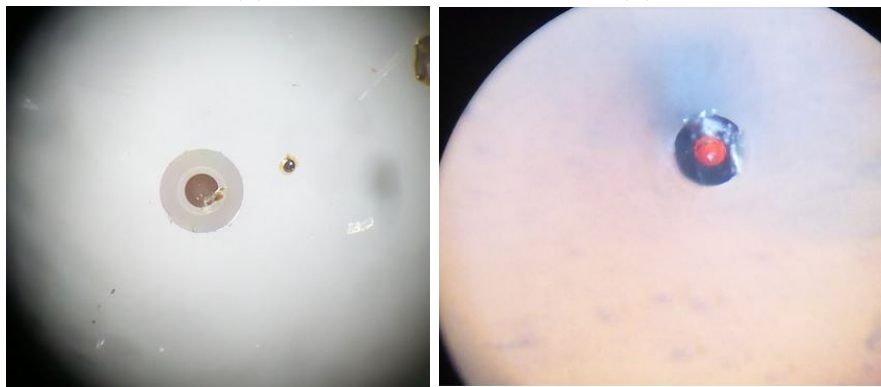


Figure 4.15: The collection fiber (a) normal commercial end & (b) the stripped and cleaved end.

Conversion efficiencies

Calculating the power conversion efficiencies at each variable in the set-up is key to understanding accuracy of the overall result at the detector. If something is not aligned or damaged knowing the original conversion efficiencies at peak performance is a fundamental tool for troubleshooting. Three main locations in the set-up were pin-pointed to record the power.

The first spectrum of radiation will be measured just after the filter. The second will be recorded just after the collimation element and therefore will represent the power that is entering the sample. The third will be collected just after the sample, while entering the TWINS free space element. The fourth is at the detector (fig. 4.16).

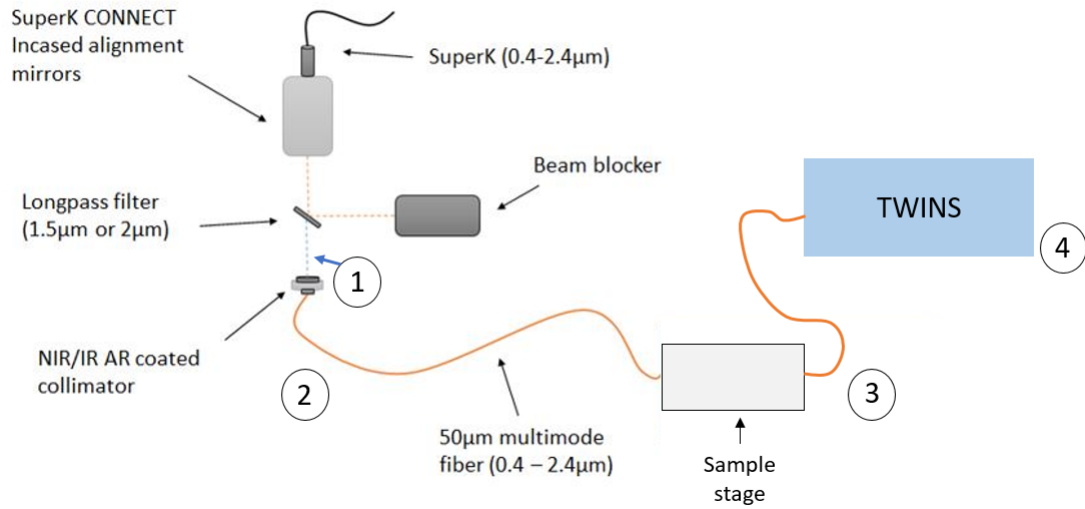


Figure 4.16: Schematic of power conversion efficiency locations measured in the set-up.

The power directly after the filter and collimator was high the same three neutral density filters stacked and used to obtain the SuperK spectrum were also used here. They were stacked in front of the extended InGaAs and connected to a voltmeter. The transmission spectrum in figure 4.9 was used to work backwards and retrieve the real power values. All powers were converted to Watts via a simple relationship factor. After the phantom, the signal in the collection fiber was measured with a voltmeter and no neutral density filters were required. Finally the signal at the detector was recorded with the lock-in amplifier since a chopper can be placed in the TWINS free-space element. The source and collection fiber in the phantom were brought to the optimal position for collection of maximum power. For this experiment a phantom with no ink was used.

First position

Power control	Measured power 1.5 μ m filter
50%	0.62W
75%	0.83W
100%	0.92W

Table 4.3: The SuperK power just after the 1.5 μ m longpass filter

Second position

Power control	Measured power 1.5 μm filter	Measured power 2.25 μm filter
50%	73mW	6mW
75%	94.8mW	10.1mW
100%	107mW	15mW

Table 4.4: The SuperK power just after the collimator for both the 1.5 μm and 2.25 μm filters

The signal recorded out of the sample measures approximately 13mV on top of a 12mV noise floor on the voltmeter. 1mV would equate to 20nW. Therefore it was decided to find the transmission loss in the TWINS by connecting the source fiber directly in the TWINS. Therefore, a comparison of the power measured on the lock-in after the free-space TWINS element and the power measured before the TWINS with a voltmeter can be measured. A signal exiting the phantom can always be determined knowing the signal at the lock-in amplifier and the loss of the TWINS.

Third position

Power control	Measured power 1.5 μm	Measured power 2.25 μm	Transmission loss 1.5 μm	Transmission loss 2.25 μm
50%	7mW	0.4mW	9.6%	6.6%
75%	8.32mW	0.68mW	8.8%	6.3%
100%	8.85mW	0.822mW	8.23%	5.5%

Table 4.5: The SuperK power measure in the lock-in amplifier after passing through the TWINS.

Fourth position

The last measurement is obtained at the final segment at the detector with every element connected as intended (fig. 4.16). The best signal with the 1.5 μm filter in place at 100% power is recorded at approximately 0.7nW. Therefore, the signal collected by the fiber exiting the phantom equates to $\approx 12nW$. It is worth noting at this point also that the max signal is found at 0.7nW but the noise floor of the set-up was also measure on the lock-in to be 2pW.

The power loss conversion efficiencies can now be calibrated for the system and is documented in figure 4.17. Knowing the noise floor of this system gives a good indication of what input power is required for sufficient detection sensitivity of the first octave band.

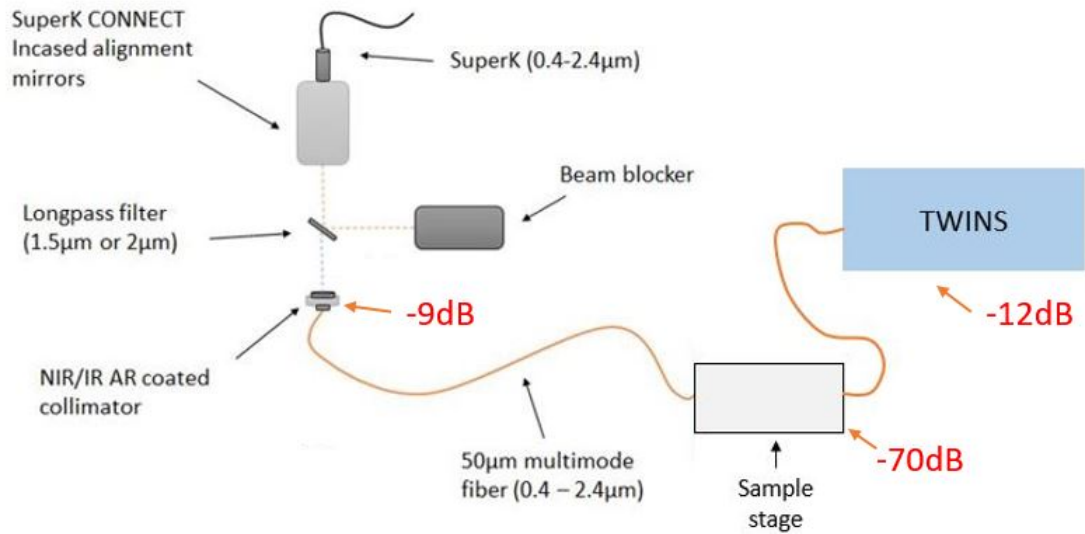


Figure 4.17: Power loss conversion efficiencies.

Conclusion

All elements of the experimental set-up were characterized and selected for the detection of the first octave band and the combination band of glucose. The optical source has a unique feature that allows manual power selection in percentage. However studying its output at different power selections revealed an interesting outcome (fig. 4.3). To ensure the wavelengths covering the combination band are entering the phantom, the higher powers of 75% – 100% must be selected.

Another issue with detecting the combination band of glucose has now also been revealed. This is the power of the source at these wavelengths. A $-91dB$ signal loss using the $2.25\mu m$ filter theoretically places the power very close to the noise level of the system. A long period of aligning and calibration has ensured that the transmission power loss values at the collimator and in the TWINS set-up are approximately constant for the combination band wavelengths. However $-70dB$ loss in the phantom will most likely degrade further for the $2.1\mu m$ as predicted by theory.

4.4 Measurement results

The first measurements were taken with a slightly different set-up as described. At the time it was not known that saturation of wavelengths with higher energy could affect the detectors ability to also record the *SWIR* region of interest. Therefore, no filter was used at the output of the source.

The results with two ink increments are shown in figure 4.18 (a), (b) and (c). There is a clear cut-off at $1.4\mu\text{m}$ at the first minimal transmission point due to maximum water absorption. However the regions of interest, i.e. the first overtone and the combination band are not distinguishable. Another reason for this is the free-space alignment of the source and the collimator. A voltmeter is used to find peak collimation. Since this does not differentiate between wavelengths and the $0.6 - 1.4\mu\text{m}$ range is more powerful then the *SWIR* region of interest, it is most likely cut-off.

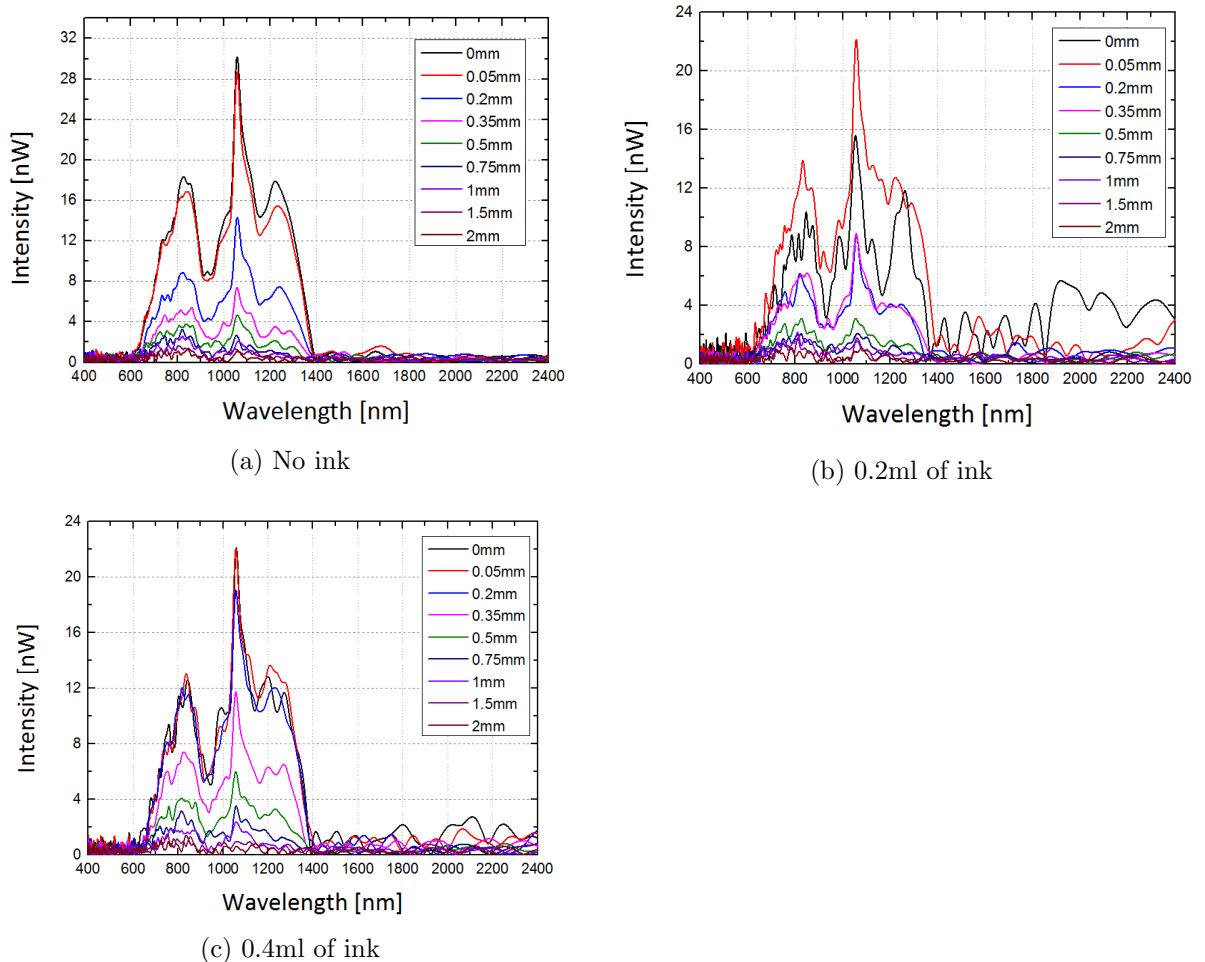


Figure 4.18: Spectrums recorded from the phantom under illumination of the full bandwidth of the SuperK source for (a) no ink, (b) 0.2ml of ink and (c) 0.4ml of ink

Filters

The results in figure 4.18 were the motivation for introducing filters in the set-up (fig. 4.4). Employing the $1.4\mu\text{m}$ filter in front of the source allowed us to detect the first overtone band. The new results of a distance decay measurement are displayed in figure 4.19 for 70% power. The first overtone band is clearly now attainable over a separation distance of 0.3mm before it enters the noise floor.

Repeating the experiment with the $2.25\mu\text{m}$ bandpass filter and re-aligning proved futile at 100% output power and nothing was detected at the detector. To explore the accuracy of the measurements further the glucose peak of $1.59\mu\text{m}$ was chosen to map the intensity decay with distance separation in logarithm scale (fig. 4.20). The results show a slight deviation from a best linear fit.

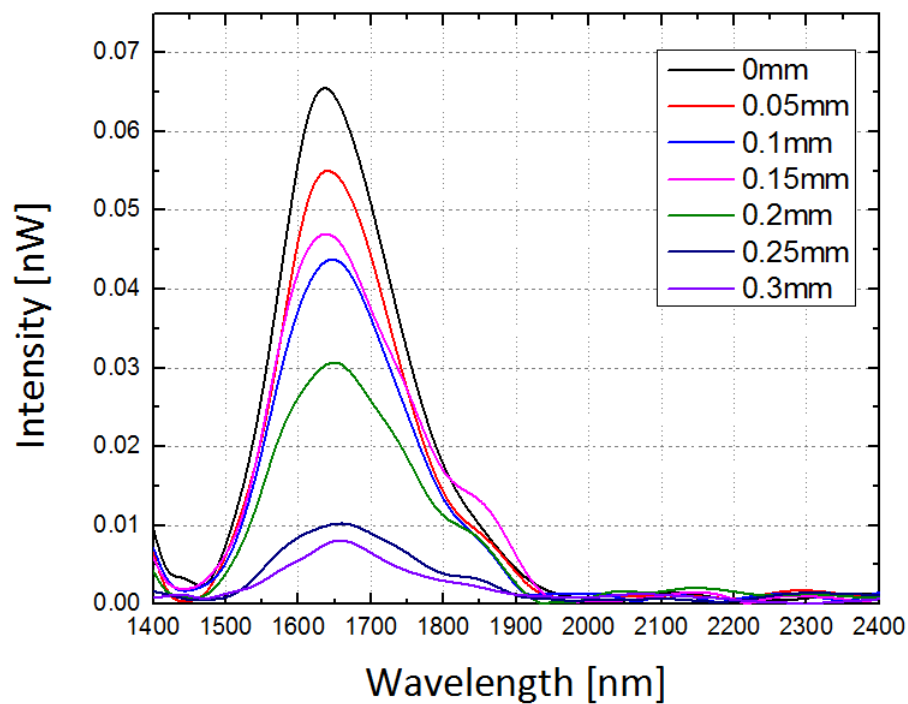


Figure 4.19: Distance decay of first overtone band with $1.4\mu\text{m}$ longpass filter

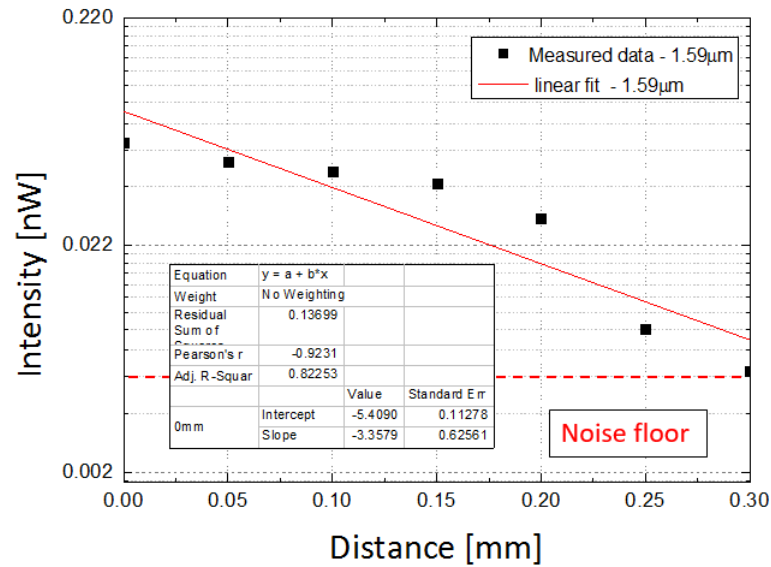


Figure 4.20: Intensity of the $1.59\mu m$ peak in log scale with separation distance increments.

4.5 Conclusion

The first overtone band was successfully detected. However the combination band was not. Two reasons for this have been described in length previously. The first is the compatibility of Lipofundin as a sufficient scattering medium and the higher wavelengths of the combination band. The second is the output power of the SuperK at these wavelengths. The power loss in the system and total noise floor were calculated in section 4.3.

Since the $2.1\mu m$ peak was not detected it is difficult to calculate a power loss conversion efficiency for that wavelength with Lipofundin in the set-up. The theory presented in chapter two does not predict what output power from the source is required to achieve a signal at the detector for the $2.1\mu m$ peak. It predicts whether Lipofundin is an efficient scattering medium so that the $2.1\mu m$ wavelength can be collected via diffuse reflection spectroscopy even without absorbing chromophores present. The conversion efficiency loss, for the $685nm$ wavelength in the Lipofundin phantom with no absorbing chromophores present, was $-21dB$. For the $1.59\mu m$ wavelength it was found to be $-70dB$. The Mie approximation predicts larger power loss via diffusion reflection spectroscopy for higher wavelengths. Therefore, natural intuition would predict that the conversion efficiency would be worse then $-70dB$ for the $2.1\mu m$ wavelength.

The SuperK has a much lower output power at higher wavelengths. From table 4.4, it was calculated that the power entering the sample for the $1.5\mu m$ filter and aligned for the first overtone band ($1.59\mu m$) of glucose is $107mW$. With the $2.25\mu m$ filter in place to explore the combination band ($2.1\mu m$), $15mW$ was measured entering the sample. A simple calculation can be realized to observe whether the Superk output power is sufficient to explore if the $2.1\mu m$ is detectable.

Ignoring the plausible larger losses for the $2.1\mu m$ wavelength, the $-70dB$ loss for the $1.59\mu m$ in the Lipofundin can be used for a comparative measurement. $15mW$ entering the sample would result in $\approx 20pW$ at the detector after the TWINS ($-12dB$ loss). This is relatively close to the noise floor of the system at $2-4pW$. With the theoretical knowledge that the $-70dB$ loss in the phantom is worse for the $2.1\mu m$ wavelength, it can be concluded that the output power of the SuperK is most likely too low to detect the $2.1\mu m$ wavelength in Lipofundin. If it is detectable. It can be concluded that a source with an output power in the combination band ($2-2.3\mu m$) of at least $100mW$ with the capabilities to scale higher, will be required to probe the $2.1\mu m$ peak in a Lipofundin phantom.

The recorded measurement fluctuations observed in figure 4.20 will be researched in more depth in the following chapter.

Chapter 5

Introducing Glucose as a Chromophore

5.1 Introduction

In this section the experimental set-up is identical to chapter 4. The only difference is the chromophore under investigation in the phantom. Glucose will be added to the optical phantom instead of ink. Ink is advantageous as it allows control of absorption, however testing the results on a chromophore of chemical relevance allows the ability to see how well the system performs.

5.2 Calculating glucose concentrations

Before the phantoms are produced it is important to theoretically calculate what concentrations of glucose should be added to the phantom to detect a change in absorption. Although the medical in-vivo concentrations of glucose were calculated in chapter two, section 2.2.3, sensitivity of detection is not the main goal at present. Therefore concentrations will be chosen to reflect large transmission losses for clear detection.

In figure 5.1 the Beer-Lambert law was simulated for an array of transmission values with a path length of $1mm$. The molar absorptivities as calculated in section 2.2.1 are plotted for each glucose peak. From this, a concentration can be extracted correlating to a specific transmission loss. Graphically this simulation shows why the $2.1\mu m$ peak, without water interfering, is theoretically much easier to detect than the $1.59\mu m$ peak. For example at concentration of $2500mM$ would reveal a 50% transmission loss at the $2.1\mu m$ peak but only a 20% loss at the $1.59\mu m$ peak.

It was chosen to increment the concentrations in order of percentage of glucose in the bulk water and Lipofundin solution. The units mM were converted to g/ml and the percentages of glucose in the $60ml$ phantom container were selected to be 0%, 5%, 15%, 25%, 45%, 55%.

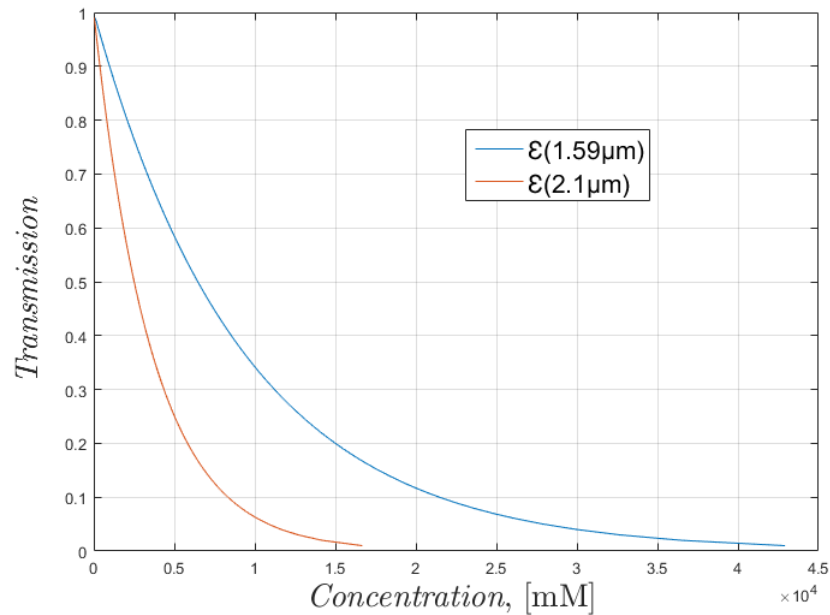


Figure 5.1: Beer-Lambert function simulated of the molar absorptivities of the two glucose peaks via MATLAB.

5.3 Measurement results

The distance decay results of the first measurements with glucose concentrations are displayed in figure 5.2. For 25% concentration the signal is very small already with the spectrum approaching the noise floor of $0.004nW$ after a distance of $0.1mm$. Concentrations of 45% and 55% offered no accurate measurements above the noise floor.

The separation distance of $0.05mm$ was chosen to investigate the relationship between intensity and concentration for the $1.59\mu m$ glucose absorption peak. Figure 5.3 details a transmission loss due to the increased concentration of glucose. The measurement points also display a slight exponential decay of intensity with increasing concentration. This decay can be described with a best fit with an equation:

$$y = (7.49 \times 10^{-6}) \exp(-x/16.56) - 1.07 \times 10^{-6} \quad (5.1)$$

The next step would, usually, be to repeat the experiment with small concentration percentages

to plot the concentration decay for the $1.59\mu\text{m}$ peak at different separation distances of the fiber. However the accuracy of the initial measurement results in figure 5.2 must be investigated further.

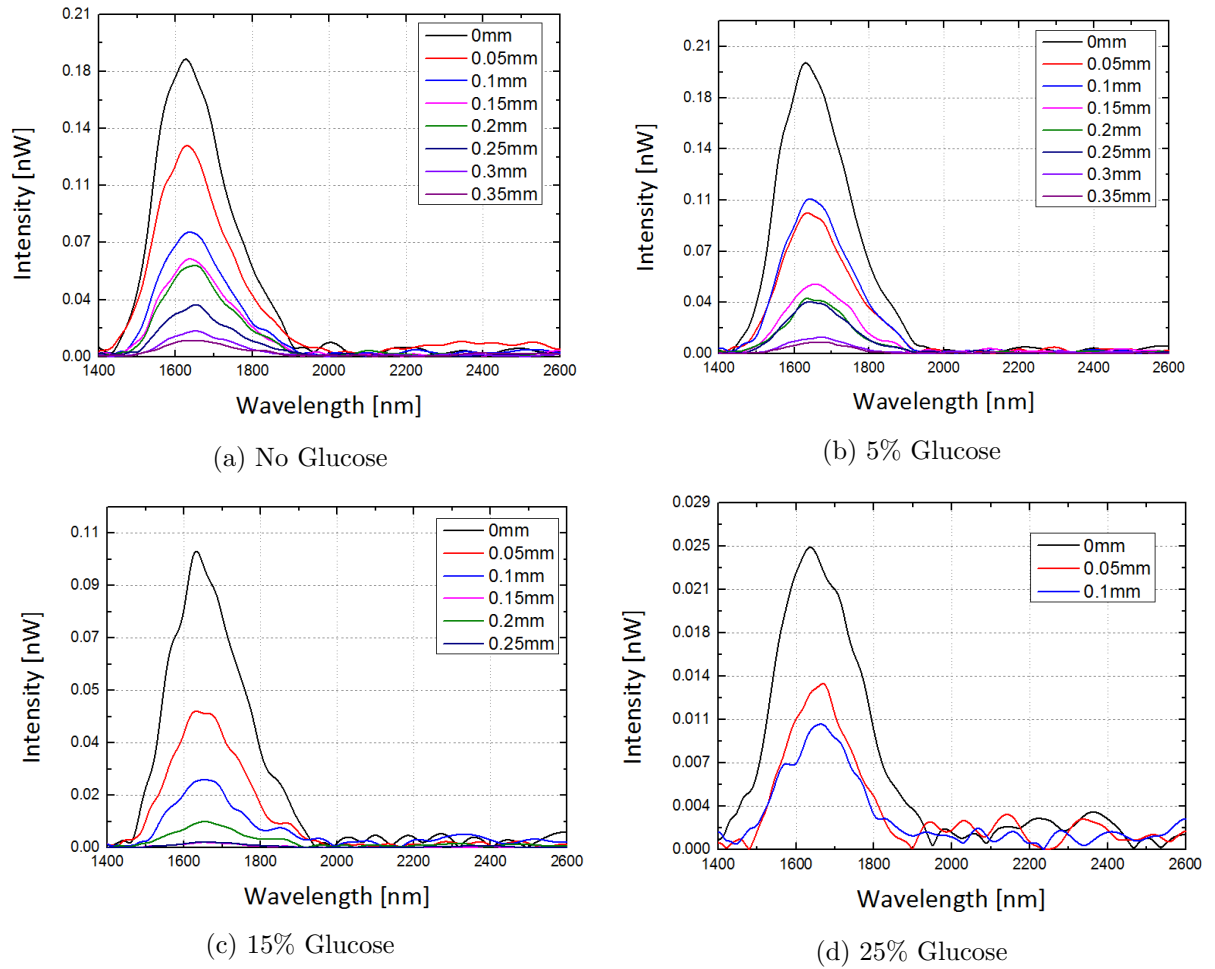


Figure 5.2: First overtone band recorded for concentrations of (a) no glucose (b) 5% glucose (c) 15% glucose & (d) 25% glucose in the phantom .

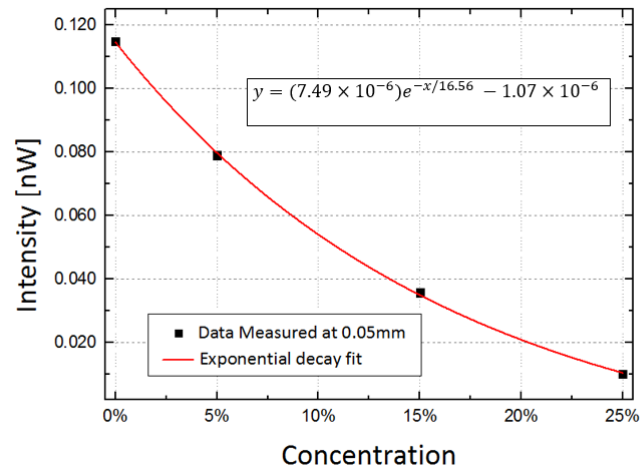
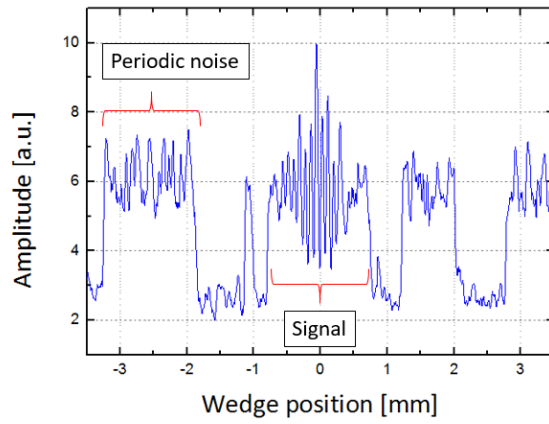


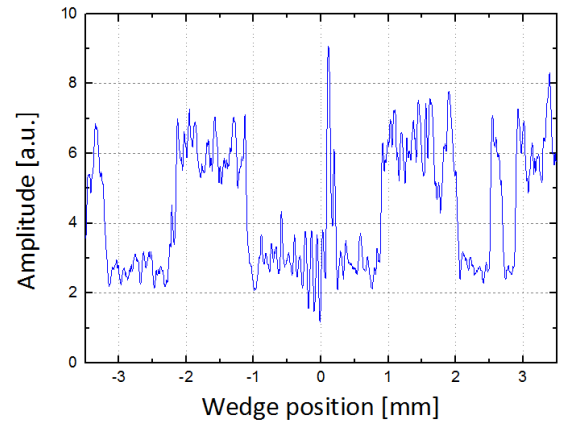
Figure 5.3: Glucose concentration decay for the $1.59\mu\text{m}$ peak at 0.05mm separation.

Fluctuations of the intensity coupled by the collimation fiber were observable in chapter 4 measurements with ink. They were also evident in the measurements with glucose chromophores. The TWINS was controlled via a LabVIEW interface that allows real-time observations of the signal as recorded by the detector and amplified by the lock-in amplifier. This was used as a tool through the project, along with an oscilloscope, for aligning and trouble shooting sections of the set-up in real-time. It was evident that apparent fluctuations of the intensity were affecting the interferograms recorded by the TWINS.

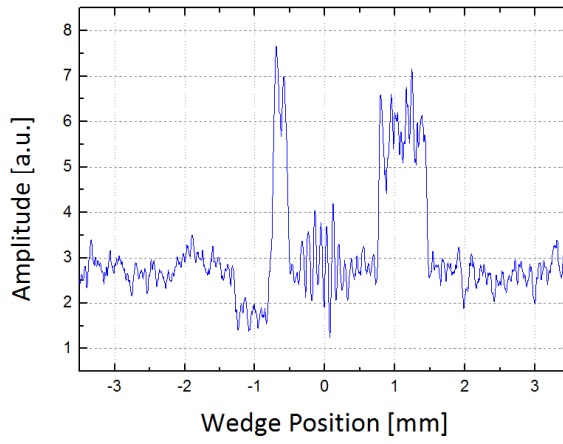
TWINS has an option on the LabVIEW control interface that allows one to average over several wedge sweeps. The advantage is that digitally the program takes the average interferogram from each repetitive sweep. The fourier transform of the average interferogram is the sole origin of the spectrum collected. The average interferogram represents the consistent signals during each sweep. Therefore unwanted noise or fluctuations can be averaged out to some degree of accuracy. However the degree of accuracy becomes diluted when the fluctuations increase in consistency and display periodic tendencies.



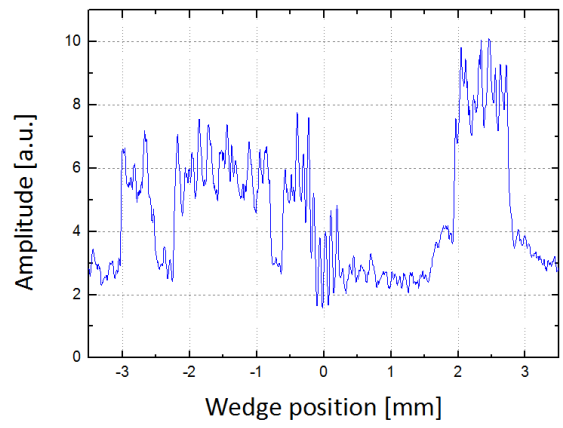
(a) First measurement



(b) second measurement



(c) Third measurement



(d) Fourth measurement

Figure 5.4: Four interferogram measurements repeated by TWINS for 25% glucose concentration at 0.05mm distance.

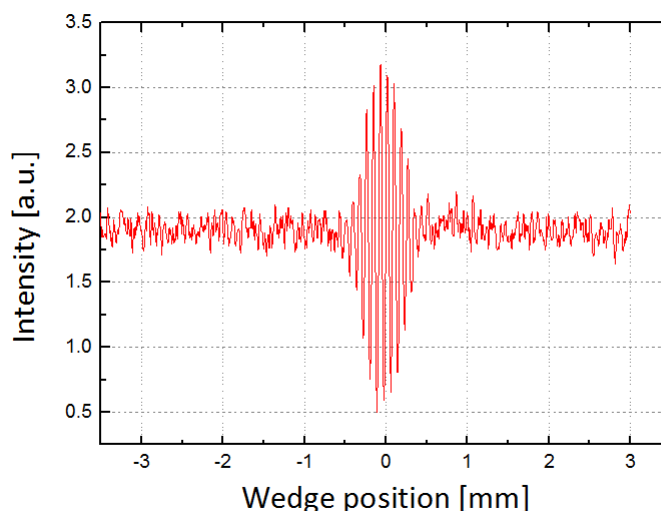


Figure 5.5: An example of an accurate interferogram measurement with acceptable noise.

Figure 5.4 displays the four interferogram measurements recorded for the 25% concentrated phantom at 0.05mm separation distance. The average of these four measurements resulted in the 0.05mm spectrum in figure 5.2 (d). Each one of these sweeps take approximately 25s . A coarse periodicity pattern in the noise fluctuations is observable in the measurements. For comparison, figure 5.5 displays a consistent interferogram measurement unaffected by intensity fluctuations.

5.3.1 Troubleshooting the fluctuations

A plan was devised to troubleshoot the cause of the intensity fluctuations. The detector was connected to a digital acquisition board which was connected to the PC and a function in Qtlab allowed for a simple recording of the intensity at the detector for a specified time input.

With this tool each variable was explored over a 15 minute time interval. First the source was tested at all power intervals including 100%. It was connected directly into the detector with neutral density filters covering the detector for protection. The result was a consistent signal. Next the TWINS setup was tested. The SuperK source was connected directly into the TWINS set-up with neutral density filters also covering the detector for protection. This test was repeated with the chopper on and off to investigate possible mechanical vibrations interfering with the phantom surface and the stripped fiber ends. The results were consistent and thus the TWINS was ruled out as the cause.

Finally the phantom was tested by measuring the output of the collection fiber directly (no TWINS present) under the constant illumination of the SuperK source. The phantom proved to be the source of the fluctuations. Next, a plan was devised to test certain hypotheses.

Stepper motor timing-belt

The results from the intensity vs time trace of the phantom resulted in consistent periodic signals occurring in two minute intervals. One hypothesis was that the Raspberry Pi could be sending the stepper motor a *reconnection* voltage every two minutes to retain connectivity. It could be possible that the this jolt could cause, on a micrometer scale, a displacement of the block holding the needle due to the connection of the timing-belt. Therefore the timing-belt was removed and the time trace tested over 15 minutes.

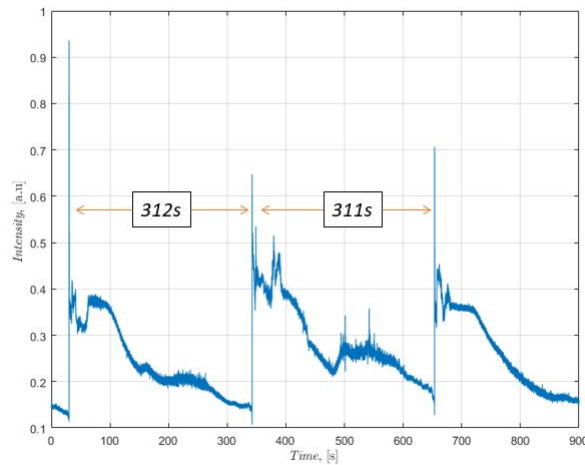


Figure 5.6: Time trace of intensity fluctuations with the step motor timing-belt detached.

The power of the SuperK source was set to 75% and the periodic fluctuations were still evident. Figure 5.6 displays a periodicity every 310s approximately.

Power

The most probably explanation to explain the fluctuations in the phantom, that were not present with the 25mW visible laser, is the high NIR power entering the phantom causing a reaction. It has been measured that at peak alignment $\approx 107mW$ with the $1.5\mu m$ filter is entering the sample as essentially heat. Since the fibers are within a $300\mu m$ distance of each other and absorption is high it could be possible there are thermal effects.

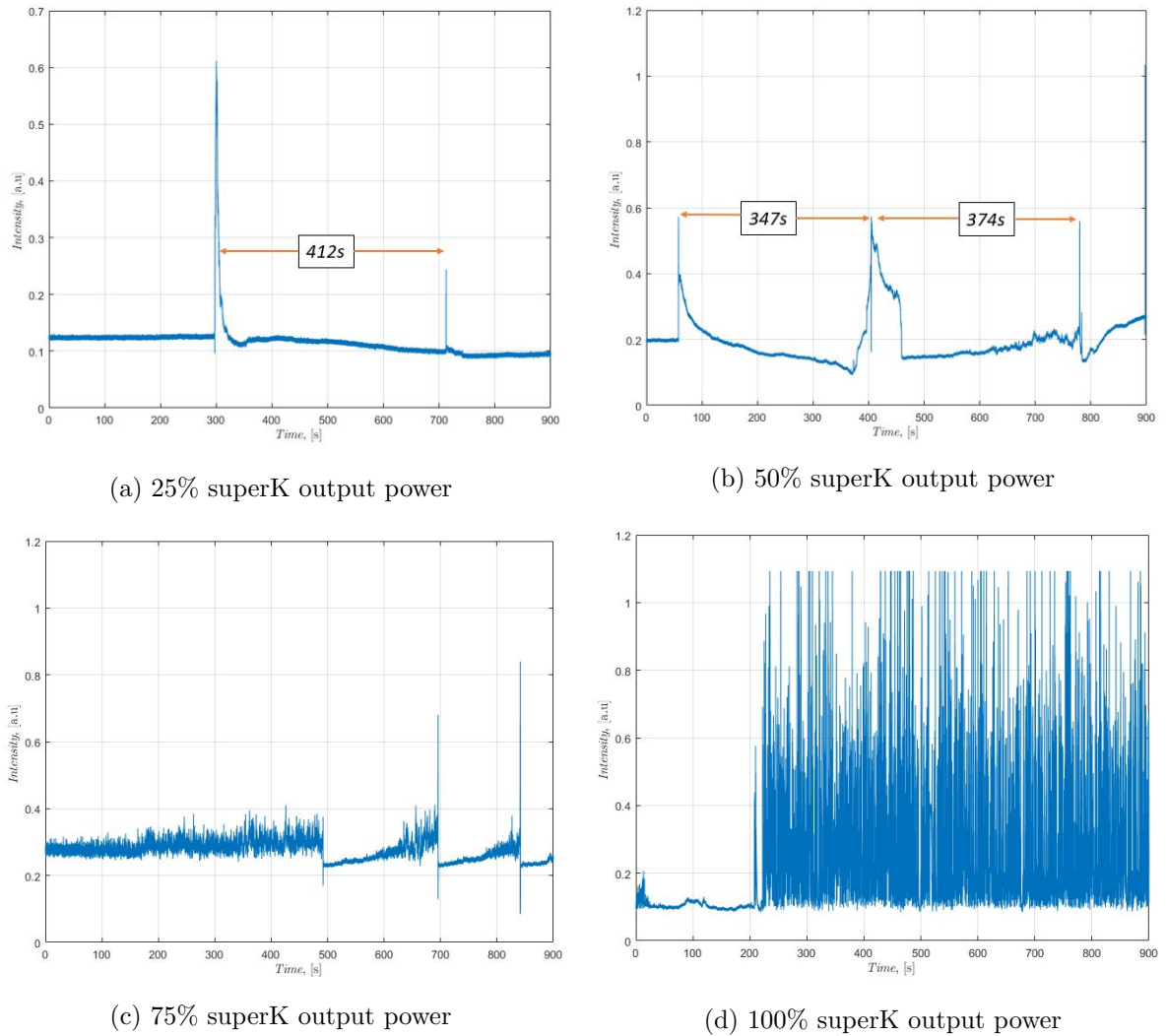


Figure 5.7: Time trace for 15 minute periods of the phantom with contrasting input powers of (a) 25%, (b) 50%, (c) 75% & (d) 100%.

The phantom under test was 6% Lipofundin diluted in water. This is the same concentration mix as the previous measurement. No ink or glucose chromophores were present. Figure 5.7 displays the results for each power increase over 15 minute time periods. A clear correlation exists between increasing the input power and an increase in the frequency of the events. The interferogram results in figure 5.4 were recorded with an input power of 100%.

Water

One final test was devised to understand whether the fluctuations can be attributed to the high absorption of water alone. A sample of water was tested illuminated by the SuperK as a source at a 100% power. The results displayed a much lower frequency of fluctuations (fig.2.6). This was repeated with a similar reproducible outcome.

Conclusion

There is now visual evidence presented of unexplained periodic behaviour which is a very strong candidate to explain previous fluctuations in the interferometer. The solution influences the reaction. The decrease in fluctuation frequency with water alone is interesting. It indicates the solution of water molecules and Lipofundin particles are the cause of the undesired effects.

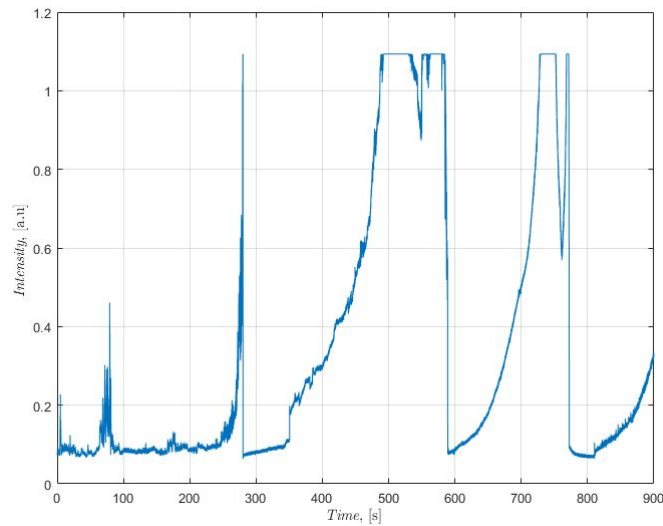


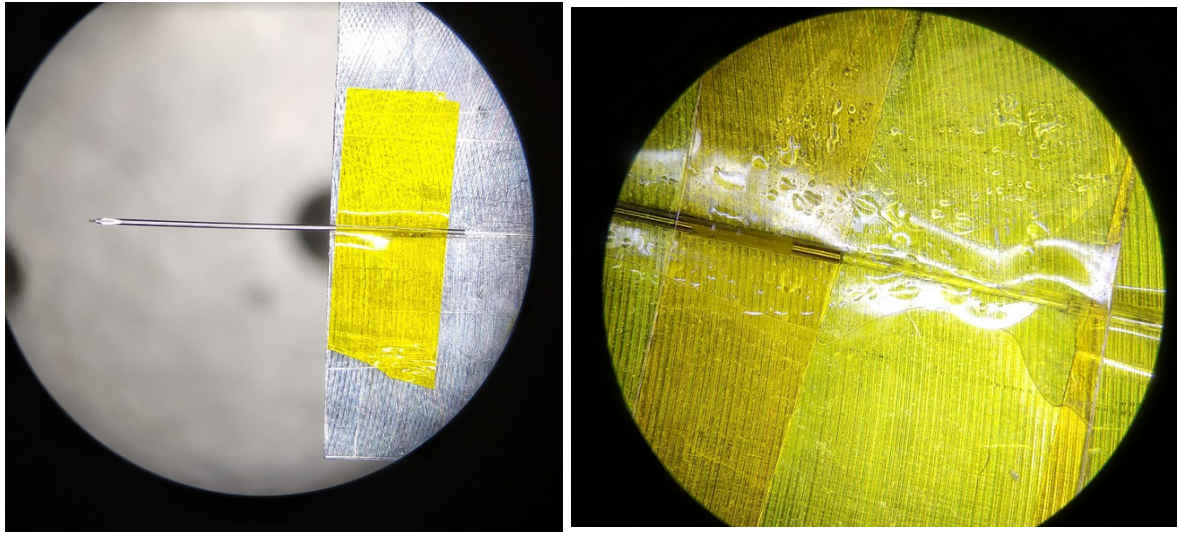
Figure 5.8: Time trace for a 15 minute period of water at 100% input power.

The solution

The most likely theory at this point in the thesis is that the high powers of the SuperK in the *SWIR* spectrum ($1.5 - 2.4\mu m$) are manipulating the scattering phantom and causing the needle, housing the stripped fiber, to move.

A simple test was devised to understand how the needle was moving and became loose. Figure 5.9 (a) displays how the needle housing the stripped fiber was attached with thermal tape to the metallic block previously. It was re-attached with a single large strip of thermal tape covering the surface area of the block. After a day of testing the block was removed from the set-up and observed under a microscope. The observations revealed a build up of droplets and swellings of the tape (fig.5.9 (b)). This counteracts the firmness of the stripped end of the fiber in the phantom and could allow movement.

The source and collection fiber were both removed from the set-up and firmly re-attached to the blocks as tight as possible with thermal tape. The initial results from a time trace with a 100% input power in a Lipofundin phantom displayed a 15 minute constant intensity response (fig. 5.10).



(a) Original attachment of the needle.

(b) Improved attachment of the needle.

Figure 5.9: Improved results with no fluctuations present.

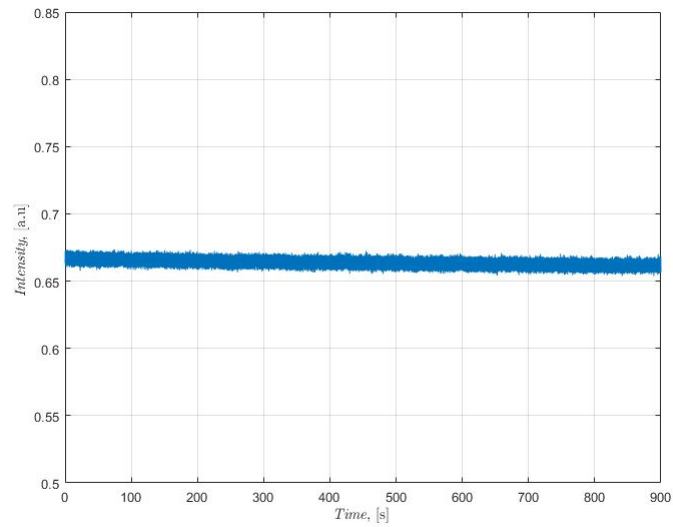


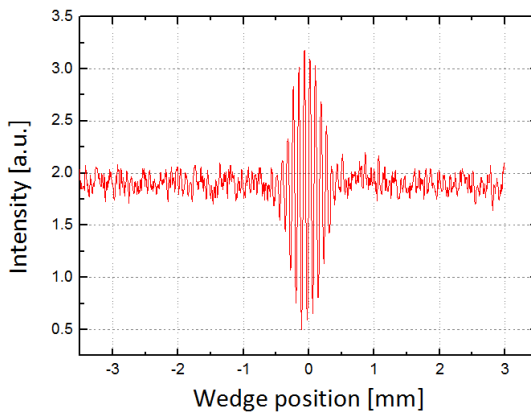
Figure 5.10: Time trace for a 15 minute period at 100% input power with improved attachment.

5.3.2 Improved results

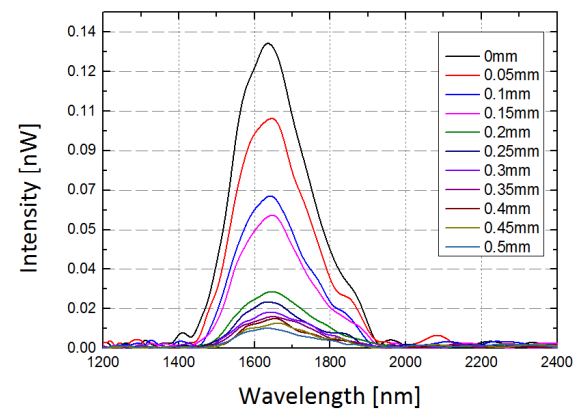
With the flat intensity response obtained the samples were remade with smaller glucose concentrations then before. The initial results for the first Lipofundin sample were very promising. The signal visible in the interferograms were constant (fig.5.11 (a)) and no fluctuations were present for the whole distance decay measurement. A measurement of four interferogram sweeps at

one distance can take three minutes. Therefore plotting the decay at 10 distances can take 30 – 40mins. An exponential decay function can be applied to decay of the $1.59\mu\text{m}$ peak at each distance (fig. 5.11 (b)).

The fluctuations became visible as soon as the phantom with the first glucose concentration was placed into the set-up. This would suggest that there is a limited timescale available when using thermal tape as an attachment before the effect becomes detectable.

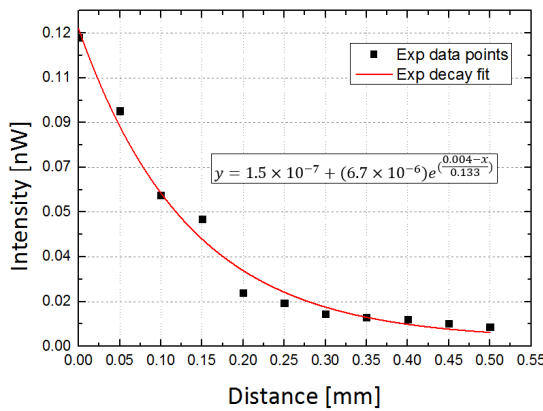


(a) Interferogram at 0.15mm distance.

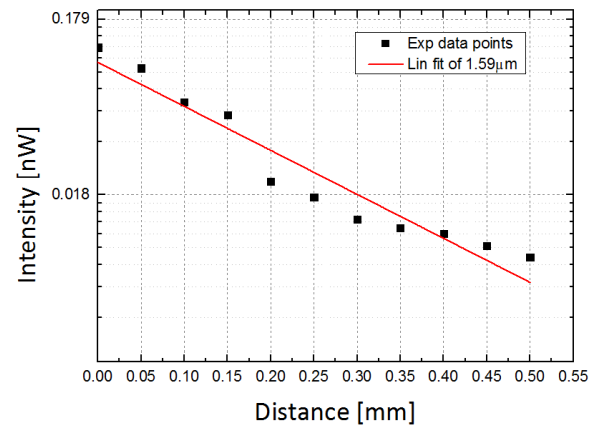


(b) Distance decay of phantom.

Figure 5.11: Improved results with no fluctuations present.



(a) Exponential decay with distance



(b) Distance decay with the logarithm of intensity

Figure 5.12: Exponential distance decay for the $1.59\mu\text{m}$ peak in the phantom.

5.4 Conclusion

This chapter troubleshooted the intensity fluctuation issue in depth. In chapter four when the broadband high powered SuperK was introduced. The results clearly show an increase in fluctuations with power introducing a dilemma. It has already been addressed in chapter four how essential maximum power is entering the set-up to allow the possibility of detecting the two glucose peaks of interest. On one hand, high power settings have proved to cause an increase of fluctuating intensity. On the other hand, high powers are required from the SuperK to cover the longer wavelengths and also because there is a minimum power required due to the losses in the set-up. This was measured to be $-70dB$ for the $1.59\mu m$ glucose absorption peak and possibly worse for the $2.1\mu m$ glucose absorption peak. Therefore although high power is detrimental to the overall performance of the system it is necessary to detect the first overtone band of glucose.

It should be noted that decreasing the power may decrease the fluctuation issue from seconds to minutes but it does not address the heart of the problem. As described, each distance decay measurement can take up to 40 minutes. Measuring six phantoms of contrasting glucose concentrations to test would create a measurement time period of over 4 hours. A time period in which the source is almost constantly on in the phantom. The fluctuations on the 2-4 minute scale would affect each phantom sweeps negatively.

The results in figure 5.3 show a clear decay in intensity at the $1.59\mu m$ wavelength with glucose concentrations of 0%, 5%, 15% and 25%, despite the frequent fluctuations. Therefore, with a stable set-up, the concentration of glucose can be extracted from the intensity of the $1.59\mu m$ wavelength measured at a distance of $0.05mm$.

Picking up a relatively good signal with a distance decay from $0 - 0.5mm$ for the $1.59\mu m$ wavelength is worth comparing to the theory in chapter two, section 2.5.4. The ideal fiber separation distance, as predicted by the Mie approximation of *Van Staveren et al.*, of $2.15mm$ for the $685nm$ wavelength was proved relatively accurate with a distance decay from $0 - 4mm$ in the Lipofundin phantom. However using the model to predict an ideal fiber separation for the $1.59\mu m$ in the Lipofundin phantom proved futile indicating the possible break down of using the diffuse reflection model under these conditions. It can now be confirmed, from the results in figure 5.12, that diffuse reflection spectroscopy can be used on a *in-vitro* phantom with Lipofundin MCT-20 as the scattering medium to probe the $1.59\mu m$ wavelength peak of glucose.

This chapter also shows that it is possible to mechanically prevent fluctuations by properly fastening the needle to the block. However thermal tape is not suitable. Accurate exponential distance decay results were found in a Lipofundin phantom with no glucose present which took a measuring time of 40 minutes. Moving onto samples with glucose proved futile as each distance decay became completely degraded with the noise fluctuations. In conclusion to this chapter, to accurately use diffuse reflection spectroscopy to qualitatively measure glucose concentrations, a new stable environment for the source and detector fiber is required.

Chapter 6

Conclusion & Future Work

The goal of this thesis research was to explore the viability of diffuse reflection spectroscopy (*DRS*) as an analytical chemistry method for extracting quantitative and qualitative measurements for absorbing chromophores in turbid environments. It is important to point out that this information is easily attainable via commercial spectrometers and integrating spheres. However these analytical chemistry methods rely on *in-vitro* samples.

Theoretically *DRS* can be applied to *in-vivo* measurements. Therefore the motivation was to prove the method could be used on *in-vitro* optical phantoms with controlled concentrations of absorbing chromophores with the hope of inspiring further research that could lead to practical uses in *in-vivo* environments.

Lipofundin was chosen as the scattering environment to induce the diffuse reflection propagation of a photon required. It was chosen as it is a research and industry standard scattering phantom used to mimic human tissue. Chapter three proved that *DRS* is a very accurate qualitative tool in analytical chemistry. A linear relationship was found between the radial distance intensity decay and concentration of ink chromophores. Most of the theory on diffuse reflection spectroscopy described turbid environments which demanded fiber separation distances on the *cm* scale and a model could not be found for the fiber separation on the $0 - 4mm$ that was required for this set-up. Therefore to find a linear relationship at this scale existed proved the method worked well on much smaller scales and could be applied to the next part of the project.

To test a chemical chromophore beyond black ink, glucose was chosen. It was chosen due to its chemical composition having the same basic three atomic building blocks as most organic compounds. Carbon, Hydrogen and Oxygen. It was also chosen in parallel as it has a medical application. The continuous detection of glucose is of extreme importance in medicine. Theory and research, for designing Lipofundin based optical phantoms to mimic human tissue, centered around the *VIS-NIR* window as this range offers the lowest absorption by water. However the

absorption chromophore glucose has two main absorption peaks in the *SWIR* at $1.59\mu\text{m}$ and $2.1\mu\text{m}$ which coincidentally occur in two bands where water absorption is also relatively low. Therefore, this refocused the goal of exploring the viability of diffuse reflection spectroscopy in the *SWIR* range with Lipofundin MCT-20.

There is little research on the suitability of Lipofundin for the longer wavelengths in the *SWIR* range. Whether *DRS* was possible for the $1.59\mu\text{m}$ and $2.1\mu\text{m}$ peak of glucose, hinged on the theoretical approximation of Mie theory of scattering. This could be predicted from measuring the mean diameter of a scattering particle in Lipofundin. Two research papers were found that used in-depth electron microscope tools to measure the mean distribution size. One found a mean distribution size of $25 - 75\text{nm}$, while the other reported a mean distribution size of $125 - 150\text{nm}$. These results have contradicting outcomes when attempting to predict whether *DRS* is viable with Lipofundin for the target $1.59\mu\text{m}$ and $2.1\mu\text{m}$ absorption peaks of glucose. The smaller radius would predict that the $1.59\mu\text{m}$ wavelength is at the very edge of detection and *DRS* and the $2.1\mu\text{m}$ wavelength is not compatible. In contrast the larger reported size of the scattering particles would predict that both glucose peaks are detectable via *DRS*. Therefore the result must be confirmed experimentally.

It was found that for the 685nm diode *VIS* laser, with 25mW entering the sample, there was a power loss conversion efficiency of $\approx -21\text{dB}$ exiting the sample. Moving to the *SWIR* wavelengths, it was found that the $1.59\mu\text{m}$ could indeed be detected. With peak alignment and a $1.5\mu\text{m}$ longpass filter in the set-up the power entering the sample was measured at 107mW . The power loss conversion efficiency with the signal exiting the sample was found to be $\approx -70\text{dB}$. The $2.1\mu\text{m}$ glucose absorption peak was not detectable. These results agree with Mie approximation for *DRS* with Lipofundin scattering particles of a mean distribution size of $25 - 75\text{nm}$. The $1.59\mu\text{m}$ glucose absorption peak of the first overtone band can be detected using the *DRS* method in a Lipofundin dilution.

It is difficult to conclude that the $2.1\mu\text{m}$ is completely unattainable. The maximum power achievable entering the phantom is 15mW with the $2.25\mu\text{m}$ bandpass filter in place. The power loss conversion efficiency is predicted to be worse than -70dB (exact value is unknown). Therefore, in principle, a source with at least powers above 100mW entering the phantom in the $2 - 2.4\mu\text{m}$ range with the ability to scale up to much higher powers would be required to test the detection of the $2.1\mu\text{m}$ glucose absorption peak via *DRS* in a the Lipofundin dilution. The SuperK only offers a maximum power of 117mW with the $2.25\mu\text{m}$ bandpass filter before $\approx -9\text{dB}$ of power is lost to collimation. If it was desired to attempt to probe the $2.1\mu\text{m}$ wavelength a different source would be required.

Rather than focusing on changing the source, an interesting step for future work would be to change the phantom. As mentioned the Lipofundin phantom was chosen to mimic the scattering environment of human tissue. However as the project progressed into the *SWIR* range it became apparent that Lipofundin not only begins to distance itself as an ideal candidate for *DRS* measurements but also as an imitator for human tissue. Human tissue, most likely due to its complex heterogeneous structure, does not follow the same pattern of reduced scattering characteristics with longer wavelengths of Lipofundin. It remains much more constant and from

theory offers ideal Mie scattering into the *SWIR* and past the glucose absorption peak of $2.1\mu\text{m}$ in the combination band. If a suitable scattering phantom could be found that truly mimics the scattering coefficients of tissue in the *SWIR* range it would be an interesting experiment to compare the *DRS* measurements for both glucose absorption peaks as the results could offer real medical application.

The results of chapter five revealed an unexpected consequence of coupling high *SWIR* powers into the sample. Intensity fluctuations that appeared to increase in frequency with power increase of the SuperK output. It was proved that, if the source and collection fibers were attached firmly, an accurate exponential distance decay measurement could be achieved. However, The current set-up relying on thermal tape proved to be futile. If the project is to carry-on, other mechanical designs that improve the fastening of the needle to the block are required. An example would be magnetic blocks.

In conclusion, to explore the glucose absorption peaks in the *SWIR* range with Lipofundin as the scattering environment, the $1.59\mu\text{m}$ peak in the first overtone band is the best target. If a phantom can be designed that mimics human tissue more accurately at the $1.59\mu\text{m}$ and $2.1\mu\text{m}$ wavelengths the power loss conversion efficiency will be expected to improve. Improving the power loss efficiency will also induce positive consequences such as potentially offering lower input powers in the phantom that are comparable to the accepted medical intensity dose on human tissue. Although targeting the fundamental bands of absorption in the *MIR* is attractive for analytical chemistry, detecting it using *DRS* would require scattering particle radii in the micrometer scale. Whether scattering environments of this nature exist and offer applicational motivation, would require further research.

QMantis hybrid detector measurement

The final quick measurement was to place the broadband hybrid photodetector fabricated at ICFO (described in chapter two, section 5.2) in the set-up and attempt to measure the first overtone band. This proved to be unsuccessful. The research device used has a lot of variability but in the advent of a champion device it would be, in principle, possible to detect the first overtone band of glucose. To test the broadband capabilities of the device and ensure the device was sensitive to the first overtone band ($1.5 - 1.8\mu\text{m}$). The device was used to measure the SuperK spectrum after the $1.5\mu\text{m}$ longpass filter and the visible diode laser with a wavelength of 685nm . The intensities were normalized with respect to each other as the purpose of the measurement is to show the broadband performance of the device used (6.1).

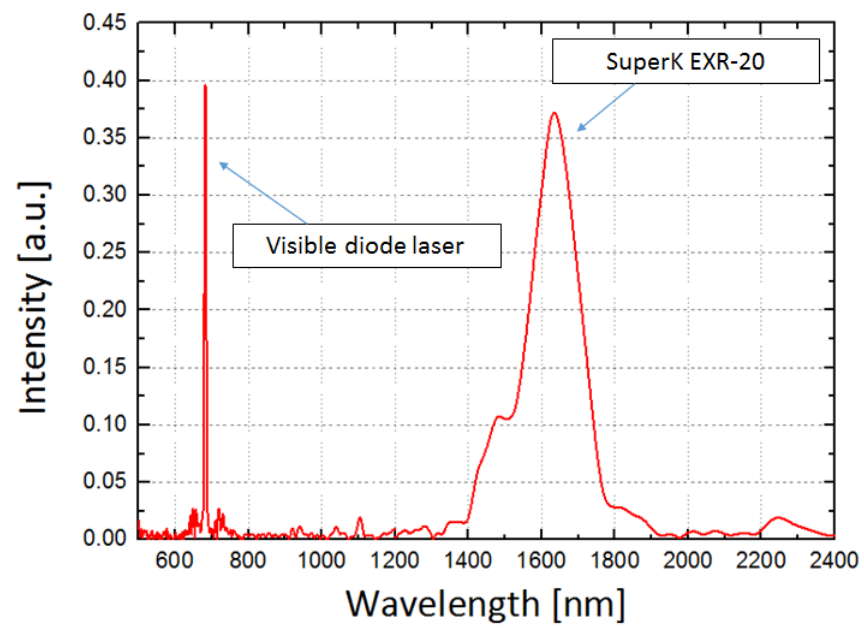


Figure 6.1: Broadband spectrum measurement for QMantis hybrid graphene-*CQD* detector.

Bibliography

- [1] NHS, 2016. “Diabetes ”
Available at: <https://www.nhs.uk/conditions/diabetes/> [Accessed 20 August 2018]
- [2] Vaddiraju, S., Burgess, D.J., Tomazos, I., Jain, F.C. and Papadimitrakopoulos, F., “Technologies for continuous glucose monitoring: current problems and future promises.”, in *Journal of diabetes science and technology*, **4**(6), pp.1540-1562, 2010.
- [3] Nikitskiy, I., Goossens, S., Kufer, D., Lasanta, T., Navickaite, G., Koppens, F.H. and Konstantatos, G. “Integrating an electrically active colloidal quantum dot photodiode with a graphene phototransistor.”, in *Nature communications* **7**, p.11954, 2016.
- [4] Goossens, S., Navickaite, G., Monasterio, C., Gupta, S., Piqueras, J.J., Perez, R., Burwell, G., Nikitskiy, I., Lasanta, T., Galan, T. and Puma, E. “Broadband image sensor array based on graphene CMOS integration.”, in *Nature Photonics* **11**(6), p.366, 2017.
- [5] Ryckeboer, E. “Spectroscopic detection of glucose with a silicon photonic integrated circuit.”, in *Doctoral dissertation, Ghent University*, 2014.
- [6] Rebel, A., Rice, M.A. and Fahy, B.G. “The accuracy of point-of-care glucose measurements”, in *Journal of diabetes science and technology* **6**(2), pp.396-411, 2012.
- [7] Bates, J.B. “Fourier transform infrared spectroscopy. ”, in *Science* **191**(4222), pp.31-37, 1976.
- [8] Jacques, S.L. “Optical properties of biological tissues: a review. Physics in Medicine & Biology”, in *Physics in Medicine & Biology*, **58**(11), p.R37., 2013.
- [9] Bashkatov, A.N., Genina, E.A., Kochubey, V.I. and Tuchin, V.V. “Optical properties of human skin, subcutaneous and mucous tissues in the wavelength range from 400 to 2000 nm”, in *Journal of Physics D: Applied Physics*, **38**(15), p.2543, 2005.
- [10] Rehault, J., Borrego-Varillas, R., Oriana, A., Manzoni, C., Hauri, C.P., Helbing, J. and Cerullo, G., “Fourier transform spectroscopy in the vibrational fingerprint region with a birefringent interferometer”, in *Optics express* **24**(1), pp.4403-4413., 2017.
- [11] Amerov, A.K., Chen, J. and Arnold, M.A., “Molar absorptivities of glucose and other biological molecules in aqueous solutions over the first overtone and combination regions of the near-infrared spectrum”, in *Applied spectroscopy*, **58**(10), pp.1195-1204, 2004.
- [12] Jobsis FF., “Noninvasive, infrared monitoring of cerebral and myocardial oxygen sufficiency and circulatory parameters”, in *Science* **198**(4323), pp.1264-1267, 1977 Dec 23.

- [13] Jobsis FF., “Discovery of the near-infrared window into the body and the early development of near-infrared spectroscopy”, in *Journal of biomedical optics* **4**(4), pp.392-397, 1999 Oct 4.
- [14] Braun, 2015. “Lipofundin MCT/LCT composition”
Available at: <https://www.bbraun.co.th/content/dam/catalog/bbraun/bbraunProductCatalog/S/AEM2th/b/lipofundin-mct-lct.pdf.bb-18262055/lipofundin-mct-lct.pdf> [Accessed 10 August 2018]
- [15] Yodh, A. and Chance, B., “ Spectroscopy and imaging with diffusing light.”, in *Physics Today* **48**(3), pp.34-41, 1995.
- [16] Durduran, T., Choe, R., Baker, W.B. and Yodh, A.G, “Diffuse optics for tissue monitoring and tomography”, in *Reports on Progress in Physics* **73**(7), p.076701, 2010.
- [17] Hernandez, S.E., Rodriguez-Armas, V.D., Perez, J.C., Martin, F.A., Castellano, M.A. and Gonzalez-Mora, J.L. “Diffuse reflectance spectroscopy characterization of hemoglobin and intralipid solutions: in vitro measurements with continuous variation of absorption and scattering”, in *Journal of biomedical optics* **14**(3), p.034026, 2009. Flock, S.T., Jacques, S.L., Wilson, B.C., Star, W.M. and van Gemert, M.J.
- [18] Flock, S.T., Jacques, S.L., Wilson, B.C., Star, W.M. and van Gemert, M.J. “Optical properties of Intralipid: a phantom medium for light propagation studies”, in *Lasers in surgery and medicine* **12**(5), pp.510-519, 1992.
- [19] Kuntsche, J., Klaus, K. and Steiniger, F. “Size determinations of colloidal fat emulsions: a comparative study.”, in *Journal of biomedical nanotechnology* **5**(4), pp.384-395, 2009.
- [20] Van Staveren, H.J., Moes, C.J., van Marie, J., Prahl, S.A. and Van Gemert, M.J. “Light scattering in Intralipid–10% in the wavelength range of 400 – 1100nm”, in *Applied optics* **30**(31), pp.4507-4514, 1991.
- [21] Jacques, S. “Optical properties of Intralipid, an aqueous suspension of lipid droplets”, in *Biomed. Opt. NewsEtc.* 1998.
- [22] Kohl, M., Lindauer, U., Royl, G., Kuhl, M., Gold, L., Villringer, A. and Dirnagl, U. “Physical model for the spectroscopic analysis of cortical intrinsic optical signals”, in *Physics in Medicine & Biology* **45**(12), p.3749, 2000.
- [23] Prahl, S.A. “A Monte Carlo model of light propagation in tissue”, in *Dosimetry of laser radiation in medicine and biology* **Vol. 10305**, p. 1030509, International Society for Optics and Photonics, 1989.
- [24] Dr. Simon A. Carn. “Scattering lecture slides”, in *Michigan Technological University* **GE4250**.
- [25] Thorlabs, 2017. “PAF series user guide”, in <https://www.thorlabs.com/drawings/6197f9eccd6221c9-D5DEB9A9-E24D-A823-E710C7AA69042186/PAF-X-18-PC-A-Manual.pdf> [Accessed 15 April 2018]
- [26] NKT Photonics, 2015. “SuperK EXTREME Supercontinuum White Light Laser Manual”, Available at <https://www.nktphotonics.com/wp-content/uploads/sites/3/2015/05/superk-extreme-1.pdf?1534074556> [Accessed 20 April 2018]

- [27] NKT Photonics, 2015. “Compact ultra-bright supercontinuum light source application note”,
Available at: <https://www.nktphotonics.com/wp-content/uploads/sites/3/2015/02/Applicationnote-Supercontinuum-SC-5.0-10401.pdf> [Accessed 25 July 2018]
- [28] Light Path Technologies, 2016. “ECO-550 glass datasheet”
Available at: <https://www.amstechnologies-webshop.com/media/pdf/ECO-550.pdf> [Accessed 10 March 2018]
- [29] Fantini S, Hueber D, Franceschini MA, Gratton E, Rosenfeld W, Stubblefield PG, Maulik D, Stankovic MR., “Non-invasive optical monitoring of the newborn piglet brain using continuous-wave and frequency-domain spectroscopy”, in *Physics in Medicine & Biology* **44**(6), p.1543, 1999.
- [30] Farrell, T.J., Patterson, M.S. and Wilson, B., “A diffusion theory model of spatially resolved, steady state diffuse reflectance for the noninvasive determination of tissue optical properties in vivo”, in *Medical physics* **19**(4), pp.879-888, 1992.
- [31] NKT Photonics, 2015. “SuperK CONNECT Broadband fiber delivery system”
Available at: <https://www.nktphotonics.com/wp-content/uploads/sites/3/2015/03/SuperKCONNECT.pdf> [Accessed 2 June 2018]
- [32] Thorlabs, 2017. “PAF Series Aspheric and Achromatic FiberPort Collimators with FC/PC, FC/APC, or SMA Adapters User Guide”
Available at: <https://www.thorlabs.com/drawings/ca68efb971b3962b-C4B9B9F7-FE16-99EA-C6E66DEEE187CF9E/PAF-X-18-PC-A-Manual.pdf> [Accessed 2 June 2018]
- [33] Thorlabs, 2003. “Edgepass Filters: Longpass and Shortpass”
Available at: <https://www.thorlabs.com/newgrouppage9.cfm?objectgroupid=918&pn=FEL1500> [Accessed 26 June 2018]
- [34] Thorlabs, 2012. “IR Bandpass Filters: 1.75 to 9.50 μm Central WavelengthIR”
Available at: <https://www.thorlabs.com/newgrouppage9.cfm?objectgroupid=5871&pn=FB2250-500> [Accessed 26 June 2018]
- [35] New England Photoconductor, 2018. “Extended InGaAs RT & TE Cooled Thermoelectrically Cooled Extended InGaAs Photodiodes”
Available at: <https://www.nepcorp.com/InGaAsExtended.html> [Accessed 1 June 2018]
- [36] Thorlabs, 2017. “PDA36A(-EC) Si Switchable Gain Detector User Guide ”
Available at: <https://www.thorlabs.com/drawings/c64ab0391b0e20d0-F9FDEB1B-9380-2D6D-F735BBC3329D14AF/PDA36A-EC-Manual.pdf> [Accessed 1 April 2018]
- [37] Thorlabs, 2000. “Mounted Absorptive Neutral Density Filters”
Available at: <https://www.thorlabs.com/newgrouppage9.cfm?objectgroupid=266&pn=NE20A> [Accessed 30 June 2018]

CONFIDENTIAL UP TO AND INCLUDING 27/08/2023 - DO NOT COPY, DISTRIBUTE OR MAKE PUBLIC IN ANY WAY

Diffuse reflectance spectroscopy characterization of molecular absorption via graphene based photodetectors

Michael Evans

Supervisors: Prof. Nicholas Le Thomas , Prof. Frank Koppens (ICFO)

Counsellors: Dr. Stijn Goossens (ICFO), Ir. Gabriel Mercier (ICFO), Ir. Carles Monasterio (ICFO)

Master's dissertation submitted in order to obtain the academic degree of
European Master of Science in Photonics

ICFO - Institut de Ciències Fotòniques, Castelldefels

and

Ghent University

Department of Information Technology

Chair: Prof. dr. ir. Bart Dhoedt

Faculty of Engineering and Architecture

Academic year 2017-2018

